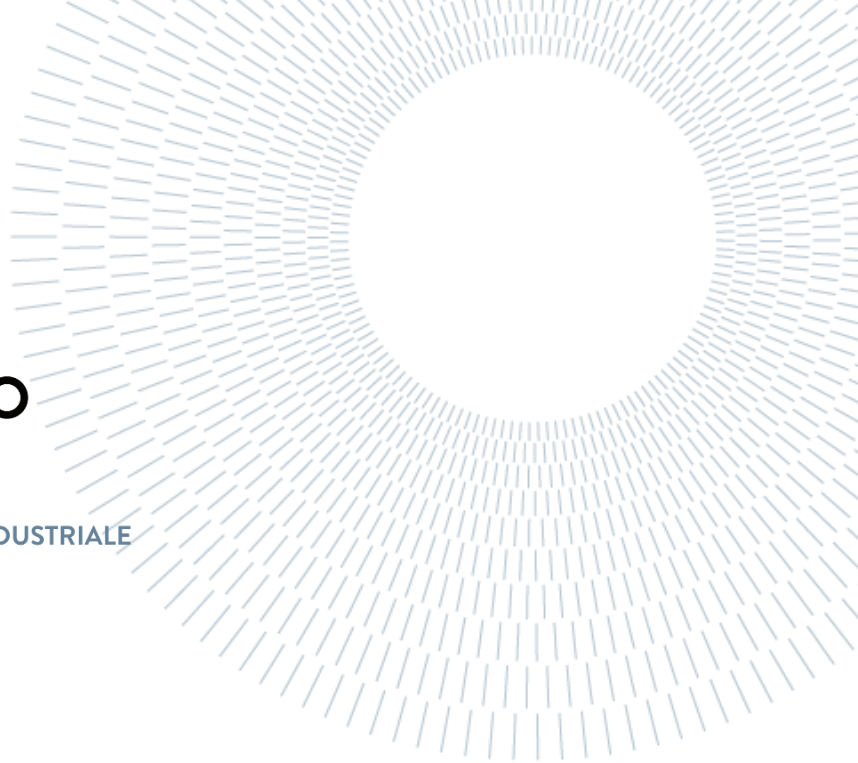




POLITECNICO
MILANO 1863

SCUOLA DI INGEGNERIA INDUSTRIALE
E DELL'INFORMAZIONE



Dynamic and static analysis of bicycle tyres tested with indoor test-rig

MASTER OF SCIENCE THESIS IN
MECHANICAL ENGINEERING

Authors: **Isabel Pollini**
Vincenzo Tartaglione

Students ID: 977953, 944207
Advisor: Prof. Gianpiero Mastinu
Co-advisor: Ing. Gabriele Dell'Orto
Academic Year: 2022-23

Abstract

The aim of this thesis work is to present the results of a dynamic and static experimental campaign performed with the VeTyT test-rig on bicycle tyres. The main target of the campaign was the measurement of the tyre characteristic curves and mechanical properties, as well as understanding the effect of different parameters, such as camber angle, vertical load and inflation pressure, on the measured quantities. The analyses were conducted on three different typologies of tyres: cargo bike, e-bike and road racing bike tyres. In Chapter 1 the current state of the art for the bicycle indoor test-rigs is described, to provide reference elements for the VeTyT test-rig to be compared with. In Chapter 2 a general description of the VeTyT system is provided. Chapter 3 focuses on the analysis of the results obtained through the dynamic tests. After a brief recall of fundamental literature concepts for road vehicle tyres, the lateral force and self-aligning torque characteristic curves of two of the tested tyres, together with their cornering stiffnesses, are provided. On top of that, a comparative analysis of the characteristic curves between tyres with the same functionality, while changing the tyre manufacturer, the tyre width or the tyre compound, is reported, as well as a qualitative analysis between tyres with different functionality. In Chapter 4 the results of the static tests are presented, focussing on important tyre properties, such as the lateral stiffness, vertical stiffnesses and relaxation length. Moreover, an analysis on the contact patch area of the tested road racing bike tyres was performed, verifying the behaviour under different vertical load and inflation pressure conditions. Implemented upgrades and potential improvements to the VeTyT test bench are discussed in Chapter 5. The development of a program automatizing the elaboration process of the acquired data is presented, as well as a preliminary analysis on a possible lateral translation system for the VeTyT structure. Some suggestions for future developments of both the software and the testing system structure are proposed. This thesis work has been elaborated in its entirety by the two authors in cooperation, with the exception of Chapter 5, which presents updates written only by the candidate Isabel Pollini.

Key-words: bicycle, tyre, test-rig, lateral force, self-aligning torque, contact patch, stiffness.

Abstract in Italiano

Lo scopo di questo lavoro di tesi consiste nel presentare i risultati di una campagna sperimentale dinamica e statica realizzata su pneumatici da bicicletta con il banco di prova VeTyT. Il principale obiettivo della campagna era la misurazione delle curve caratteristiche degli pneumatici e delle loro proprietà meccaniche, oltre alla comprensione dell'effetto che diversi parametri, come l'angolo di camber, il carico verticale e la pressione di gonfiaggio, hanno sulle grandezze misurate. Le analisi sono state condotte su tre tipologie di pneumatico differenti: da cargo bike, da e-bike e da bici da corsa. Nel Capitolo 1 è descritto l'attuale stato dell'arte per quanto riguarda i banchi prova indoor per biciclette, per fornire degli elementi di riferimento con cui poter comparare il VeTyT. Nel Capitolo 2 è fornita una descrizione generale del sistema del VeTyT. Il Capitolo 3 si focalizza sull'analisi dei risultati ottenuti tramite le prove dinamiche. Dopo un breve ripasso dei concetti fondamentali della letteratura per pneumatici di veicoli da strada, le curve caratteristiche della forza laterale e del momento auto allineante di due degli pneumatici testati, insieme alle loro cornering stiffness, sono fornite. Inoltre, è riportata un'analisi comparativa tra le curve caratteristiche di pneumatici con la stessa funzionalità, ma diversa casa produttrice, battistrada o mescola, oltre a un'analisi qualitativa tra curve con diversa funzionalità. Nel Capitolo 4 sono presentati i risultati delle prove statiche, focalizzati su importanti proprietà dello pneumatico, come la rigidezza laterale, la rigidezza verticale e la lunghezza di rilassamento. Inoltre, è stata condotta un'analisi sull'impronta di contatto degli pneumatici da corsa testati, verificando il loro comportamento per diverse condizioni di carico verticale e pressione di gonfiaggio. Gli aggiornamenti implementati sul banco di prova VeTyT e potenziali migliorie sono discussi nel Capitolo 5. Lo sviluppo di un programma che automatizza il processo di elaborazione dei dati acquisiti è presentato insieme a un'analisi preliminare su un possibile sistema di traslazione laterale per la struttura del VeTyT. Vengono inoltre proposti suggerimenti per gli sviluppi futuri sia del software che della struttura del sistema di prova. Questa tesi è stata sviluppata nella sua interezza dai due autori in collaborazione, con l'eccezione del Capitolo 5 che presenta aggiornamenti scritti esclusivamente dalla candidata Isabel Pollini.

Parole chiave: bicicletta, pneumatico, banco di prova, forza laterale, momento auto allineante, impronta di contatto, rigidezza.

Contents

Abstract	i
Abstract in Italiano	iii
Contents	vii
List of Figures	x
List of Tables	xvi
Introduction	1
List of tyres	5
1 State of the Art: ways of measurement of bicycle tyre characteristics	9
1.1. Test-rig at University of Padua	10
1.2. Test-rig at University of Wisconsin-Milwaukee.....	11
1.3. Test-rig at Delft University of Technology	12
1.4. Test-rig at Karlsruhe Institute of Technology	14
2 Introduction to VeTyT	15
2.1. Frame	15
2.2. Running contact surface	16
2.3. Cardan joint.....	18
2.4. Watt's linkage.....	18
2.5. Steering system.....	19
2.6. Fork.....	19
2.7. Measuring instruments	20
2.8. Vertical Load Setting System.....	22
3 Dynamic Analysis	23
3.1. Road Vehicles tyre literature	24
3.1.1. <i>Fy</i> : Lateral Force	24
3.1.2. <i>Mz</i> : Self-aligning torque.....	26
3.1.3. <i>Cα</i> : Cornering stiffness.....	28
3.2. Standard Dynamic Analysis	29
3.2.1. Cargo bike Tyre – SCH-T01	30
3.2.1.1. Constant pressure and camber, vertical load variation	30

3.2.1.2. Constant pressure and vertical load, camber variation.....	33
3.2.1.3. Cornering stiffness	36
3.2.2. E-Bike Tyre – SCH-T03	37
3.2.2.1. Constant pressure and camber, vertical load variation.....	38
3.2.2.2. Constant pressure and vertical load, camber variation.....	41
3.2.2.3. Cornering stiffness	44
3.3. Abnormal characteristic curves.....	45
3.3.1. SCH-T03 and SCH-T04	46
3.3.2. CST-T02	51
3.3.3. SCA-T05	53
3.4. Comparison between tyre characteristic curves	54
3.4.1. Comparison between tyres belonging to the same function group ..	54
3.4.1.1. Cargo bike tyres	55
3.4.1.2. E-bike tyres.....	58
3.4.1.3. Road racing bike tyres.....	62
3.4.2. Qualitative comparison between tyre functional groups	65
4 Static Analysis.....	69
4.1. Vertical Stiffness Analysis.....	69
4.1.1. Set-up for the measurement	70
4.1.2. Results	72
4.2. Contact Patch Analysis	77
4.3. Lateral Stiffness.....	86
4.3.1. Set-up for the measurement	88
4.3.2. Acquisition phase	91
4.3.3. Data Analysis	91
4.3.4. Results	92
4.4. Relaxation Length Analysis	96
5 VeTyT improvements.....	103
5.1. Future structural updates to VeTyT	103
5.1.1. New lateral translation system	103
5.1.2. Modified “height” calibration system	111
5.2. Software Development	112
5.2.1. Starting point.....	113
5.2.2. Post processing.....	113
5.2.2.1. Software inputs	113

5.2.2.2.	Software Outputs	115
5.2.2.3.	Data Processing	115
5.2.2.4.	Visualization.....	117
5.2.3.	Report Generator	118
5.2.4.	Future software developments.....	119
5.2.4.1.	Guided User Interface (GUI)	119
6	Conclusion and future developments.....	123
Bibliography		127
A Appendix A		132
A.1.	Contact patch	132
B Appendix B.....		139
B.1.	Post Processing code	139

List of Figures

Figure 1.1: Test-rig at University of Padua, the “MotoTireMeter”.	10
Figure 1.2: Test-rig at University of Wisconsin-Milwaukee.....	12
Figure 1.3: Test-rig at Delft University of Technology.....	13
Figure 1.4: Test-rig at Karlsruhe Institute of Instrumented.	14
Figure 2.1: VeTyT on flat track, configuration without linear actuator in the steering system.	15
Figure 2.2: The two parts composing VeTyT’s frame: upper part (a), lower part (b). The final assembled frame (c).	16
Figure 2.3: Rotating drum.	17
Figure 2.4: Detail of VeTyT’s flat track belt.	17
Figure 2.5: Pneumatic and cooling systems overview.	17
Figure 2.6: Cardan, or universal, joint belonging to the VeTyT system.	18
Figure 2.7: Detail of VeTyT’s Watt’s Linkage, instrumented with two load cells.	18
Figure 2.8: Steering system, equipped with the linear motor.	19
Figure 2.9: VeTyT’s two principal axes, the steering axis and the camber axis, highlighted on the structure.	19
Figure 2.10: Single sided fork equipped with the high stiffness rim, mounted on the VeTyT.	20
Figure 2.11: Double sided fork equipped with a commercial wheel, mounted on the VeTyT.	20
Figure 2.12: Linear magnetic encoder.....	21
Figure 2.13: Load cell for the measurement of the force on the steering rod F_s	22
Figure 2.14: Load cell for the measurement of the vertical load F_z , placed on top of the steering shaft.	22
Figure 2.15: Vertical load setting system, with masses applied on the lever arm.	22
Figure 3.1: Lateral force versus slip angle characteristic curve for a general tyre, for various brake slip levels.	24

Figure 3.2: Lateral force vs slip angle curve for different vertical load values, for a P215/60 R15 Goodyear Eagle GT-S tyre inflated at 31 psi (214 kPa).....	25
Figure 3.3: Camber effect on a lateral force vs slip angle characteristic curve	26
Figure 3.4: Top view of a tyre, showing the generation of the self-aligning torque M_z	26
Figure 3.5: Camber effect on a self-aligning torque vs slip angle characteristic curve.....	27
Figure 3.6: Self-aligning torque vs slip angle curve for different vertical load values, for a P215/60 R15 Goodyear Eagle GT-S tyre inflated at 31 psi (214kPa).	27
Figure 3.7: Graphic representation of the cornering stiffness definition	28
Figure 3.8: Cornering stiffness vs vertical load for a general road vehicle tyre.	29
Figure 3.9: Lateral force plot as a function of the side slip angle, for pressure equal to 400 kPa, camber 0° and varying vertical load (411 N, 526 N) for SCH-T01.	31
Figure 3.10: Self-aligning torque plot as a function of the side slip angle, for pressure equal to 400 kPa, camber 0° and varying vertical load (411 N, 526 N) for SCH-T01.....	32
Figure 3.11: Lateral force plot as a function of the side slip angle, for pressure equal to 400 kPa, vertical load $F_z = 411 N$ and varying camber (-5°, 0°, 5°) for SCH-T01.....	34
Figure 3.12: Self-aligning torque as a function of the side slip angle for pressure equal to 400 kPa, vertical load $F_z = 411 N$ and varying camber (-5°, 0°, 5°) for SCH-T01.....	35
Figure 3.13: Lateral force plot as a function of the side slip angle, for pressure equal to 300 kPa, camber 0° and varying vertical load (343 N, 404 N, 488 N) for SCH-T03.....	38
Figure 3.14: Self-aligning torque plot as a function of the side slip angle, for pressure equal to 300 kPa, camber 0° and varying vertical load (343 N, 404 N, 488 N) for SCH-T03.....	40
Figure 3.15: Lateral force plot as a function of the side slip angle, for pressure equal to 300 kPa, vertical load $F_z = 404 N$ and varying camber (-5°, 0°, 5°) for SCH-T03.....	42

Figure 3.16: Self-aligning torque as a function of the side slip angle for pressure equal to 300 kPa, vertical load $F_z = 404\text{ N}$ and varying camber ($-5^\circ, 0^\circ, 5^\circ$) for SCH-T01.....	43
Figure 3.17: Lateral force (left) and self-aligning torque (right) plot as a function of the side slip angle, for pressure equal to 500 kPa, vertical load $F_z = 488\text{ N}$ and varying camber ($-5^\circ, 0^\circ, 5^\circ$) for the first SCH-T03 test.....	48
Figure 3.18: Lateral force (left) and self-aligning torque (right) plot as a function of the side slip angle, for pressure equal to 500 kPa, vertical load $F_z = 488\text{ N}$ and varying camber ($-5^\circ, 0^\circ, 5^\circ$) for the first SCH-T04 test.....	49
Figure 3.19: Lateral force (left) and self-aligning torque (right) plot as a function of the side slip angle, for pressure equal to 500 kPa, vertical load $F_z = 488\text{ N}$ and varying camber ($-5^\circ, 0^\circ, 5^\circ$) for the repeated SCH-T03 test	50
Figure 3.20: Lateral force (left) and self-aligning torque (right) plot as a function of the side slip angle, for pressure equal to 500 kPa, vertical load $F_z = 488\text{ N}$ and varying camber ($-5^\circ, 0^\circ, 5^\circ$) for the repeated SCH-T04 test	50
Figure 3.21: Contact patch of the CST-T02 tyre, in the zone affected by the manufacturing defect.....	51
Figure 3.22: Lateral force (left) and self-aligning torque (right) plot as a function of the side slip angle, for pressure equal to 400 kPa, camber 0° and varying vertical load (411 N, 449 N, 526 N) for the first CST-T02 test	52
Figure 3.23: Lateral force (left) and self-aligning torque (right) plot as a function of the side slip angle, for pressure equal to 400 kPa, camber 0° and varying vertical load (411 N, 449 N, 526 N) for the repeated CST-T02 test.	52
Figure 3.24: Lateral force (left) and self-aligning torque (right) plot as a function of the side slip angle, for pressure equal to 300 kPa, vertical load $F_z = 404\text{ N}$ and varying camber ($-5^\circ, 0^\circ, 5^\circ$) for the SCA-T05 tyre	53
Figure 3.25: Lateral force plot as a function of the side slip angle, for pressure equal to 400 kPa, camber 0° and vertical load equal to 411 N for the analysed cargo bike tyres.....	56
Figure 3.26: Self-aligning torque plot as a function of the side slip angle, for pressure equal to 400 kPa, camber 0° and vertical load equal to 411 N for the analysed cargo bike tyres.....	57
Figure 3.27: Lateral force plot as a function of the side slip angle, for pressure equal to 300 kPa, camber 0° and vertical load equal to 343 N for the analysed e-bike tyres.	59

Figure 3.28: Self-aligning torque plot as a function of the side slip angle, for pressure equal to 300 kPa, camber 0° and vertical load equal to 343 N for the analysed e-bike tyres.	61
Figure 3.29: Lateral force plot as a function of the side slip angle, for pressure equal to 350 kPa, camber 0° and vertical load equal to 340 N for the analysed road racing bike tyres.	63
Figure 3.30: Self-aligning torque plot as a function of the side slip angle, for pressure equal to 350 kPa, camber 0° and vertical load equal to 340 N for the analysed road racing bike tyres.	64
Figure 3.31: Lateral force plot as a function of the side slip angle for the analysed tyre categories under the testing conditions specified in Table 3.25.	66
Figure 3.32: Self-aligning torque plot as a function of the side slip angle for the analysed tyre categories under the testing conditions specified in Table 3.25.	67
Figure 4.1: The tyre cross section under the action of a vertical load undergoes a vertical deflection (tyre drop).....	70
Figure 4.2: Complete set-up for the vertical stiffness measurement.	71
Figure 4.3: Tyre drop as function of vertical load and inflation pressure for SCH-T04.....	73
Figure 4.4: Tyre drop as function of vertical load and inflation pressure for SCH-T03.....	74
Figure 4.5: Tyre drop as function of vertical load and inflation pressure for, in the continuous line, SCH-T03 and for, in dashed line, SCH-T04.	74
Figure 4.6: The vertical load function of the linearized tyre drop: at left SCH-T04, at right SCH-T03.	75
Figure 4.7: Working principle of the Prescale sheets	79
Figure 4.8: Contact patch of VIT-T10 at 350 kPa and 490 N.....	79
Figure 4.9: Contact patch of VIT-T10 at 350 kPa and 490 N compared with the elliptical approximation.	81
Figure 4.10: Example of contact patch analysis through ImageJ® software. VIT-T10 at 350 kPa and 490 N.	81
Figure 4.11: Contact patch of VIT-T10 at 350 kPa and 490 N with the Matlab® script.....	83
Figure 4.12: For the VIT-T10: on the left, the contact patch area as function of vertical load, when varying the inflation pressure; on the right, the contact	

patch area as function of inflation pressure, when varying the vertical load.	84
Figure 4.13: On the left (a), the contact patch of VIT-T10 at 550 kPa and 490 N; on the right (b), the contact patch of VIT-T11 at 550 kPa and 490 N	86
Figure 4.14: Tyre cross section under the action of a lateral force..	87
Figure 4.15: On the left, it is represented a detailed scheme of the forces acting on the set-up; on the right it is expressed the equilibrium equation of forces at plate in the lateral direction.	87
Figure 4.16: System used to connect the aluminium plate and the threaded metal rod.....	89
Figure 4.17: The clamp rigidly connects the rim to the VeTyT frame thanks to the use of wooden blocks.	89
Figure 4.18: Complete set-up for the lateral stiffness measurement.....	90
Figure 4.19: Example of total lateral force F_w measured by the Watt's linkage load cells as function of acquisition time. (VIT-T11 at 350 kPa and 340 N)...	91
Figure 4.20: Example of a complete measurement results for a given condition of inflation pressure and vertical load. (VIT-T10 at 350 kPa and 490 N)	92
Figure 4.21: On the left, the lateral stiffness as function of inflation pressure, when varying the vertical load, of the VIT-T10; on the right, the lateral stiffness as function of inflation pressure, when varying the vertical load, of the VIT-T11.	95
Figure 4.22: time solution of the first order differential equation when varying the relaxation length.	97
Figure 4.23: The relaxation length of the VIT-T10 as function of vertical load, when varying the inflation pressure.	101
Figure 4.24: The relaxation length of the VIT-T11 as function of vertical load, when varying the inflation pressure.	101
Figure 5.1: Lateral translation system preliminary design.....	106
Figure 5.2: Stopper preliminary design.....	107
Figure 5.3: Interactions: distributed loads, bolts, external supports.....	108
Figure 5.4: Von Mises stress analysis. At top, the frontal part of the stopper; at bottom, the rear part of the stopper.....	109
Figure 5.5: Linear guidelines with the stopper positioned to avoid the movement of the block.	110
Figure 5.6: The assembly of the load cell that measures the vertical load. ...	111

Figure 5.7: On the left, the turnbuckle-style connecting rods working principle. On the right, the turnbuckle-style connecting rods CAD.	112
Figure 5.8: Workspace content.	114
Figure 5.9: F_w and slip angle versus time plots, for both repetition of the test at 400kPa, camber 0° and 488N for the SCH-T03 tyre.	115
Figure 5.10: Menu interfaces of the Post Processing software for the choice of the analysis type (a), of the single test to analyse (b), of the tests to be averaged (c).	116
Figure 5.11: Slip angle signal motion law: in red is the whole acquired signal, in green is the part taken into consideration for the tests.	117
Figure 5.12: Checkbox menu for the analysis type choice.....	118
Figure 5.13: Drafts of dashboards for the Post Processing application, for the data elaboration (a) and visualization (b).....	121

List of Tables

Table 3.1: Lateral force values at slip angle equal to 4° and -4° , at constant pressure 400 kPa , constant camber 0° and varying vertical load (411 N , 526 N) for SCH-T01.....	31
Table 3.2: Peak self-aligning torque values and corresponding slip angles, at constant pressure 400 kPa , constant camber 0° and varying vertical load (411 N , 526 N) for SCH-T01	33
Table 3.3: Lateral force values at slip angle equal to 2° and -2° , at constant pressure 400 kPa , constant vertical force 411 N and varying camber (-5° , 0° , 5°) for SCH-T01.	34
Table 3.4: Peak self-aligning torque values and corresponding slip angles; constant pressure 400 kPa , constant vertical load 411 N and varying camber (-5° , 0° , 5°) for SCH-T01.....	36
Table 3.5: Cornering stiffness values at constant pressure (400 kPa), constant camber equal to 0° and varying vertical load (411 N , 526 N) for SCH-T01..	36
Table 3.6: Cornering stiffness values at constant pressure (400 kPa), varying camber (-5° , 0° , 5°) and vertical load (411 N , 526 N) for SCH-T01	37
Table 3.7: Lateral force values at slip angle equal to 4° and -4° , at constant pressure 300 kPa , constant camber 0° and varying vertical load (343 N , 404 N , 488 N) for SCH-T03.....	39
Table 3.8: Peak self-aligning torque values and corresponding slip angles, constant pressure 300 kPa , constant camber 0° and varying vertical load (343 N , 404 N , 488 N) for SCH-T03.....	40
Table 3.9: Lateral force values at slip angle equal to 2° and -2° ; constant pressure 300 kPa , constant vertical force 404 N and varying camber (-5° , 0° , 5°) for SCH-T03.	42
Table 3.10: Peak self-aligning torque values and corresponding slip angles; constant pressure 300 kPa , constant vertical load 404 N and varying camber (-5° , 0° , 5°) for SCH-T03.	43
Table 3.11: Cornering stiffness values constant camber equal to 0° , varying pressure (300 kPa , 400 kPa , 500 kPa) and vertical load (343 N , 404 N , 488 N) for SCH-T03.....	44
Table 3.12: Cornering stiffness values at constant pressure equal to 300 kPa , varying camber (-5° , 0° , 5°) and vertical load (343 N , 404 N , 488 N) for SCH-T03.	45

Table 3.13: Analysed cargo bike tyres, with complete name, dimensions and internal tyre code.....	55
Table 3.14: Testing conditions chosen for the analysis of the considered tyres.	55
Table 3.15: Lateral force values at slip angle equal to $\pm 2^\circ$ and $\pm 4^\circ$ and cornering stiffness values for the analysed cargo bike tyres.	56
Table 3.16: Peak self-aligning torque values and relative slip angle values for the analysed cargo bike tyres.	57
Table 3.17: Analysed e- bike tyres, with complete name, dimensions and internal tyre code.....	58
Table 3.18: Testing conditions chosen for the analysis of the considered tyres.	59
Table 3.19: Lateral force values at slip angle equal to $\pm 2^\circ$ and $\pm 4^\circ$ and cornering stiffness values for the analysed e-bike tyres.....	60
Table 3.20: Peak self-aligning torque values and relative slip angle values for the analysed e-bike tyres.....	61
Table 3.21: Analysed cargo bike tyres, with complete name, dimensions and internal tyre code.....	62
Table 3.22: Testing conditions chosen for the analysis and cornering stiffness values of the considered tyres	62
Table 3.23: Lateral force values at slip angle equal to $\pm 2^\circ$ and $\pm 4^\circ$ and cornering stiffness values for the analysed e-bike tyres.....	63
Table 3.24: Peak self-aligning torque values and relative slip angle values for the analysed road racing bike tyres.....	64
Table 3.25: Testing conditions chosen for the analysis and cornering stiffness values of the considered tyres	66
Table 4.1: Tyre drop measurements for SCH-T04	72
Table 4.2: Tyre drop measurements for SCH-T03	73
Table 4.3: Vertical stiffness values of SCH-T04 in the left part and of SCH-T03 in the right part; down, the indicators from the manufacturer: a) SCH-T04; b) SCH-T03	76
Table 4.4: Area contact patch = Load/Pressure at different loads (340 N, 400 N, 490 N) and pressures (0.35 MPa, 0.55 MPa, 0.75 MPa).....	78
Table 4.5: Area contact patch as elliptical, at different loads (340 N, 400 N, 490 N) and pressures (350 kPa, 550 kPa, 750 kPa). VIT-T10.....	80

Table 4.6: Area contact patch with the software ImageJ®, under different loads (340 N, 400 N, 490 N) and pressures (350 kPa, 550 kPa, 750 kPa). VIT-T10.	82
Table 4.7: Area contact patch of VIT-T10 with the Matlab® script, at different loads (340 N, 400 N, 490 N) and pressures (350 kPa, 550 kPa, 750 kPa)	83
Table 4.8: Area contact patch of VIT-T11 with the Matlab® script, at different loads (340 N, 400 N, 490 N) and pressures (350 kPa, 550 kPa, 750 kPa)	85
Table 4.9: Percentage variation in area at different loads (340 N, 400 N, 490 N) and pressures (350 kPa, 550 kPa, 750 kPa)	85
Table 4.10: VIT-T10 lateral stiffness values for different conditions of inflation pressure (350 kPa, 550 kPa, 750 kPa) and vertical load (340 N, 400 N, 490 N).	
.....	93
Table 4.11: VIT-T11 lateral stiffness values for different conditions of inflation pressure (350 kPa, 550 kPa, 750 kPa) and vertical load (340 N, 400 N, 490 N).	
.....	94
Table 4.12: The cornering stiffness values for different conditions of inflation pressure (350 kPa, 550 kPa, 750 kPa) and vertical load (340 N, 400 N, 490 N), for: on the left, the VIT-T10 tyre; on the right, the VIT-T11 tyre.....	99
Table 4.13: The lateral stiffness values for different conditions of inflation pressure (350 kPa, 550 kPa, 750 kPa) and vertical load (340 N, 400 N, 490 N), for: on the left, the VIT-T10 tyre; on the right, the VIT-T11 tyre.....	99
Table 4.14: The relaxation length values for different conditions of inflation pressure (350 kPa, 550 kPa, 750 kPa) and vertical load (340 N, 400 N, 490 N), for: at the top, the VIT-T10 tyre; at the bottom, the VIT-T11 tyre	100
Table 5.1: Stopper material and material properties	107
Table 5.2: Bolts properties	108
Table A. 1: Full contact patch analysis for VIT-T10.....	1353
Table A. 2: Full contact patch analysis for VIT-T11.....	138

Introduction

Mobility is one of the cornerstones of European society both for the Council of Europe and the European Union. It is crucial for the global economic growth and for the definition of people's quality of life. However, the mobility is also responsible for a set of negative effects. Especially looking at car mobility, high environmental and health pressures are reached in terms of pollution, congestion, traffic crashes, noise, and other externalities [1].

During the 2015 United Nations Climate Change Conference, when the Paris Climate Agreement was signed, it became clear that the European Union and its member states must take drastic action to deal with the inevitable consequences of climate change. The aim is to limit the average temperature increase to 2°C above pre-industrial levels [2]. An increase of $3 - 4^{\circ}\text{C}$ in temperature, as a matter of fact, would cause a high sea-level rise, significant loss of biodiversity, more extreme weather conditions, and food insecurity, resulting in catastrophic effects and conflicts between countries.

Transport is one of the most significant sectors responsible for climate change, in fact, in the European Union, it contributes to almost 30% of the total greenhouse gas emissions that causes global warming, of which 72% is derived from road transport [3]. For this reason, the European Union aims to achieve a 90% reduction in greenhouse gas emissions from transport by 2050, compared with 1990 [4]. The harmful air pollution factors emitted by the transport sector include carbon monoxide (CO), nitrous oxides (NO_x), particulate matter (PM_{2.5}, PM₁₀), sulphurous oxides (SO_x), volatile organic compounds (VOC), and ozone (O₃), which lead to, among others, acidification, eutrophication and health issues. Furthermore, noise pollution is generated, especially in highly dense urban areas [5].

The car industry is also responsible for vast amounts of waste in the environment, mainly due to the production of cars and fuel extractions. The car mobility industry uses many non-renewable energy sources due to the manufacturing of cars, the construction and maintenance of the road network, and the fuels needed to drive the vehicle. In addition, car mobility takes up a lot of space for circulation and storage of vehicles, which, therefore, cannot be used for other activities [6]. In recent years, more cars that use more sustainable resources have been developed (e.g., electric cars, natural gas, or biofuels) [7]. Studies state that electric vehicles will use 58% less energy than petrol cars and emit 64% less carbon dioxide over their lifetime [8]. The use of electric and hybrid cars is increasing, but it will take for sure many more years before cars on fossil fuels are entirely replaced.

Another way to achieve sustainable mobility is the promotion of active travel (soft mobility) which includes any non-motorized transport that can be used for short distances. The most common form of active travel is cycling [9].

Starting from the first prototype of bicycle developed by Baron Karl von Drais in 1817, cycling quickly became popular, with more than a billion people using it for transportation and sport-related activities [10]. Several benefits can be identified concerning cycling. For the economic point of view, according to the European Commission, cycling produces, already at current levels, globally 150 billion euros each year, of whom more than 90 billion euros are linked to positive aspects such as public health, the environment and the mobility, over all [11].

Several environmental and health-related benefits originate from cycling. Compared to the car, cycling contributes to more CO₂ emission savings and, thus, to less air and noise pollution [12]. Secondly, no fossil fuels are needed to use the bicycle (excluding during manufacturing), reducing the geopolitical dependency of the European society on high-risk countries such as Russia, China, and Saudi Arabia. With respect to cars most materials will remain the same (e.g., steel, aluminium and polymers). Cycling, as physical activity as well as pollutant reduction element, contributes to longer and healthier lives [12], in fact it helps to prevent diseases such as type 2 diabetes, cardiovascular diseases, cancer, and osteoporosis that are harmful or even fatal [13]. Moreover, it has highly positive effects on mental health because engaging in moderate physical activity reduces the risk of Alzheimer's disease and lowers the odds of developing depression [14].

The European Commission developed the goal of promoting cycling, which resulted in the establishment of several European projects, namely ADONIS and WALCYING, to increase the knowledge about the positive aspects related to cycling [15]. The Dutch Masterplan Bicycle in the Netherlands in 1990 intended to achieve 30% more bicycle kilometres by people than in 1995 in 2010 [16]. Infrastructure, parking facilities/theft prevention and safety (bicycle fatalities account for 8% of the total road fatalities recorded in 2016 in EU countries [17]) have increased the diffusion of cycling in the past 50 years. Even though the car is generally used to drive larger distances, it is also used to a large extent for shorter distance trips. In order to exploit all the benefits of cycling it is vital to use it as an alternative for shorter distance trips.

In the recent years a strong study on bicycle differentiation has been developed thanks to the different purposes they can have, i.e., mountain bikes, road race bikes, city bike and the more modern e-bikes and cargo bikes. An electrification campaign of the bicycles has been developed, achieving 35.3 million of electric bicycle in 2016 from 290 000 in 2000 [18], in order to give a competitive alternative to common cars for covering short - medium distances and give assistance to the rider in terms of power. Differently from electric scooter and motorcycles, the driving license is not mandatory for the e-bikes. In urban areas, also solutions such as cargo bicycles (even with electric drives

for support [19]) and trailers are becoming increasingly popular, since they allow the transportation of large and heavy loads in a stable way.

The recent Covid-19 pandemic has increased the development of individual and sustainable mobility[[20], [21]], in order to meet the government policies. For this reason the scientific and engineering world focused their interest on bicycles, particularly on their dynamics.

Tyres represent a fundamental element since it is the only part in contact with the ground and, thus, its mechanical characteristics can affect the stability (safety) and performance (handling) of bicycles.

The tyre lateral properties can be measured through field testing or by indoor testing machines and are the basis for any dynamic analysis. While, instability, such as wobble and wave, is enhanced by high speed, that is typically reached only by professional or amateur road cycling riders, during descents [[22], [23], [24]]. There are currently a few examples of test benches for studying bicycle tyre properties in the world, but they are not standardised, and often adapted from motorcycle/car applications.

The test-rig, named "VeTyT" (acronym of Velo Tyre Testing), located at the "Laboratorio per la Sicurezza dei Trasporti" ("Laboratory for Safety of Transport", La.S.T.) [25] in the Department of Mechanical Engineering of Politecnico di Milano, has been standardised in November 2022. It was conceived to measure the characteristic curves of the bicycle tyres, in order to meet the needs of this fast-growing market.

The aim of this thesis work is to present the results of a dynamic and static test campaign performed on different bicycle tyres. These experimental tests were carried out also to understand the effect of different parameters, such as camber angle, vertical load and inflation pressure, on the measurement of the tyre characteristic curves and properties (lateral stiffness, cornering stiffness and relaxation length). In addition, a study of the contact patch was developed. In this way the lack of experimental tests on road cycling tyres in literature, can be covered.

List of tyres

ROAD RACING BIKE TYRES	
Tyre Name	Tyre acronym
<i>Vittoria Road Racing / Competition Corsa N.ext 28" x 26 ETRTO¹ 26 – 622</i>	VIT-T10
<i>Vittoria Road Racing / Competition Corsa N.ext 28" x 28 ETRTO¹ 28 – 622</i>	VIT-T11
<p>The two foldable tyres are developed by Vittoria S.p.a.. Described as combining “Vittoria's peerless knowledge of racing performance with the durability of a long-lasting nylon casing that uses a unique Silica and Graphene compound for improved rolling efficiency, grip and longer wear-life. To increase puncture protection, the central section of the casing features 3 layers of nylon as well as an additional puncture protection belt”. [26]</p>	
RIM: Rigid	

CARGO BIKE TYRES	
Tyre Name	Tyre acronym
<i>Schwalbe Balloon Big Ben Plus (20" x 2.15) ETRTO¹ 55-406</i>	SCH-T01
<p>It is a foldable tyre developed by Schwalbe. It is described to have a “large volume for optimum effective suspension. The robust 3 mm GreenGuard protection and reinforced sidewalls make this tire a reliable companion in the busy city and beyond. ECE-R75 approved, comfortable and resilient. The perfect choice for every kind of E-Bike. The new Schwalbe Big Ben Plus is the perfect tire for different types of trendy bikes: E-bikes, cargo bikes and electric cargo bikes. It possesses the “ECE-R75 certification, necessary for e-bikes with maximum speed up to 50 km/h.” [27]</p>	

Tyre Name	Tyre acronym
<i>CST Brooklyn (20" x 2.15)</i> <i>ETRTO¹ 55 – 406</i>	CST-T02
It is a foldable tyre, belonging to CST. According to the manufacturer: "your cargo bike is a real workhorse. You need to deliver the load quickly – but you want to do it in reasonable comfort too. Our urban tire, the Brooklyn, is the perfect tire for cargo bikes. The thick anti-puncture layer, the stiffened sidewalls and the ideal natural suspension characteristics mean that you're still fit at the end of a long workday". [28]	
RIM: <i>Mach1 Kargo Disc 20" (406 - 25c)</i>	

E-BIKE TYRES	
Tyre Name	Tyre acronym
<i>Schwalbe 50km Energizer, Active Plus P-Guard 5 (28" x 1.7)</i> <i>ETRTO¹ 47 – 622</i>	SCH-T04
It is a foldable tyre, belonging to the Schwalbe Energizer family (specific tyres for e-bikes), described as having "a high-quality compound, low rolling resistance and, above all, a good adherence. For this reason, this tyre has a high safety level, even in cornering. In addition, the 3 mm caucho insert, PunctureGuard (P-Guard), guarantees a good puncture protection. It possesses the ECE-R75 certification, necessary for e-bikes with maximum speed up to 50 km/h". [29]	
Tyre Name	Tyre acronym
<i>Schwalbe 50km Energizer Plus G-Guard 5/Addix-E (28"x1.75)</i> <i>ETRTO¹ 47 – 622</i>	SCH-T03
It is a foldable tyre, belonging to the Schwalbe Energizer family (specific tyres for e-bikes), described as having "an ultramodern, dynamic touring profile with a smooth centre section and strong diamond sides. It rolls easily on the road and has good grip, even on unpaved ground. The newly created Addix E-Compound, created appositely for e-bikes, is specially optimized for maximum durability, low rolling resistance and exceptional grip even at high speed. The 3 mm insert in natural caucho obtained in part with recycled material, GreenGuard (G-Guard), guarantees reliable puncture protection in everyday touring. It possesses the ECE-R75 certification, necessary for e-bikes with maximum speed up to 50 km/h". [30]	
Tyre Name	Tyre acronym

<i>Scalato Mondano (28" x 2.15)</i> <i>ETRTO¹ 55 – 622</i>	SCA-T05
<p>It is a foldable tyre developed by Scalato. According to the manufacturer: "this is the ultimate city bike tire. Especially developed for electric city bikes, and made from superior material (Twaron®, para-aramid product to deliver products that are stronger, lighter, and more resistant) . This tire also works perfectly on a heavy e-bike. Fast, smooth and stable: the Mondano is a joy on every bicycle path. SCALATO tires offer double layer "bead to bead" protection with reinforced sidewalls and a high-end casing of 60 threads per inch (60TPI) gives you the performance you are looking for. This strongly woven material gives the tire extra strength". [31]</p>	
<p>RIM: <i>Shimano Deore HB-M525A 28" (622)</i></p>	

1. ETRTO. Based on the European Tyre and Rim Technical Organisation (ETRTO) standard, the first number represents the tyre width at the widest point of the tire, expressed in millimetres, and the second number represents the inner tyre diameter at the tire bead that rests on the rim, expressed in millimetres.

1 State of the Art: ways of measurement of bicycle tyre characteristics

The recent interest in the study of bicycles has led to the development of experimental methods and test-rigs aimed at measuring their tyres' characteristic curves and properties. Tyres have a principal role in vehicle dynamics since they are the only element that connects the vehicle with the ground, exchanging forces in the tyre-road contact patch. In literature the studies on tyre characteristics are mainly related to cars and trucks since these vehicles were of primary interest in the 1900s for their potentialities, in terms of mobility and transportation, combined with the economic boom caused by the industrial development.

The lack of data regarding bicycle tyres is the main issue for the next years when the bicycles could represent a turning point for a more sustainable society. Therefore, some experimental test methods have been developed for measuring bicycle tyre properties and characteristic curves. It is possible to distinguish between outdoor and indoor testing. The first allows to perform tests under more realistic conditions, since the tyre is rolling on the ground, as it is intended to do in real applications, carried by a trailer. However, during outdoor testing the tyre is subjected to many random external phenomena, making the measured data non-repeatable. The indoor testing, on the other hand, does not replicate exactly the real conditions, but can ensure repeatability. Moreover, the variation of a tyre parameter can be mainly associated with their effect on the tyre properties, without the high uncertainty of it being caused by an external disturbance.

In this Chapter, the current bicycle indoor test-rigs present in literature are described in order to have a reference for the test-rig used during this thesis work.

1.1. Test-rig at University of Padua

At the Department of Industrial engineering of University of Padua one of the first test-rig for measuring the bicycle tyre properties was designed (Figure 1.1), starting from an initial prototype made for motorcycle and scooter tyres. The test-rig [32], called “MotoTireMeter”, consists in a planar rotating disk with diameter equal to 3 m, covered with high friction sandpaper. The tested wheel is supported by a chassis and rolls on the high frictional part of the rotating disk.

The acquisition of the forces and torques of interest is obtained by means of a set of load cells: a single-axis load cell measures the lateral force F_y , a similar load cell is used to evaluate the self-aligning torque M_z , and a third load cell measures the torque M_y .

The system allows high values of camber angles γ (up to $\pm 54^\circ$), by rolling the chassis, and side slip angle α (up to $\pm 10^\circ$), by adjusting the orientation of the fork.

Because of the curvature of the track followed by the wheel, an additional contribution to the lateral force, named “curvature force”, is introduced and it is directed towards the outside of the track. To take into consideration this additional force, the data must be corrected by less than 4% [33].

In 2012, several bicycle tyres were tested [34]. During the experimental campaign the speed was set to 4 km/h and the camber angles were limited to 24° in order to prevent detrimental wheel hop vibrations. It was noticed that the limited slip angles (from 0.5° to 4°) of the tests did not allow to reach saturation conditions. In addition, the values of lateral force for small slip angles ($\alpha < 1^\circ$) were very difficult to measure, because of the low lateral force values and the presence of the curvature force term, which does not decrease. This led to a strongly reduction in the signal-to-noise ratio.



Figure 1.1: Test-rig at University of Padua, the “MotoTireMeter”. [34]

1.2. Test-rig at University of Wisconsin-Milwaukee

The test-rig at University of Wisconsin-Milwaukee was specifically designed for bicycle tyres [35]. The latest version consists in a frame made of welded steel (the first version was made of wood) and an aluminium fork holding the wheel on top of a flat track system, similar to a chain. The chosen materials accomplish the high stiffness required to the system to undergo lower deformations. The frame is connected to the ground by means of a two-degrees-of-freedom universal joint, located at a distance of 1.3 m from the bicycle tyre (Figure 1.2), behind the wheel contact patch so that any friction in the bearings or seals generates a negligible contribution to the lateral force.

The configuration of the system can vary. The camber angle can be introduced and adjusted by rotating the universal joint about its longitudinal axis, while the generation of the slip angle is possible by pivoting the flat track about its vertical axis. The vertical load is set by the weight of the frame and by adding masses of known weight above the fork. The track can be covered with anti-skid tape, to perform tests under different friction coefficient between the road and the tyre.

For the acquisition of forces and torques a system of sensors is developed. The fork rotation about the steering axis is prevented by a force sensor, connected to the rigid frame, which measures the self-aligning torque M_z . The lateral force is measured by a force sensor that prevents the lateral motion of the tyre. However, this measured lateral force is not the one generated in the contact patch, so a torque equilibrium equation is needed to obtain the lateral force generated at the contact patch F_y .

The described system has two main advantages: the possibility to continuously change camber angle and side slip angles during the test and the possibility to mount different types of rims.

However, the main drawback consists in the maximum achievable speed, limited to 0.15 m/s, which is not representative of the real speed conditions of a bicycle. This is caused by the low power provided to the flat track by the electric motor, and by the limits in the range of variation slip angles and/or camber angles imposed by the low width of the flat track.

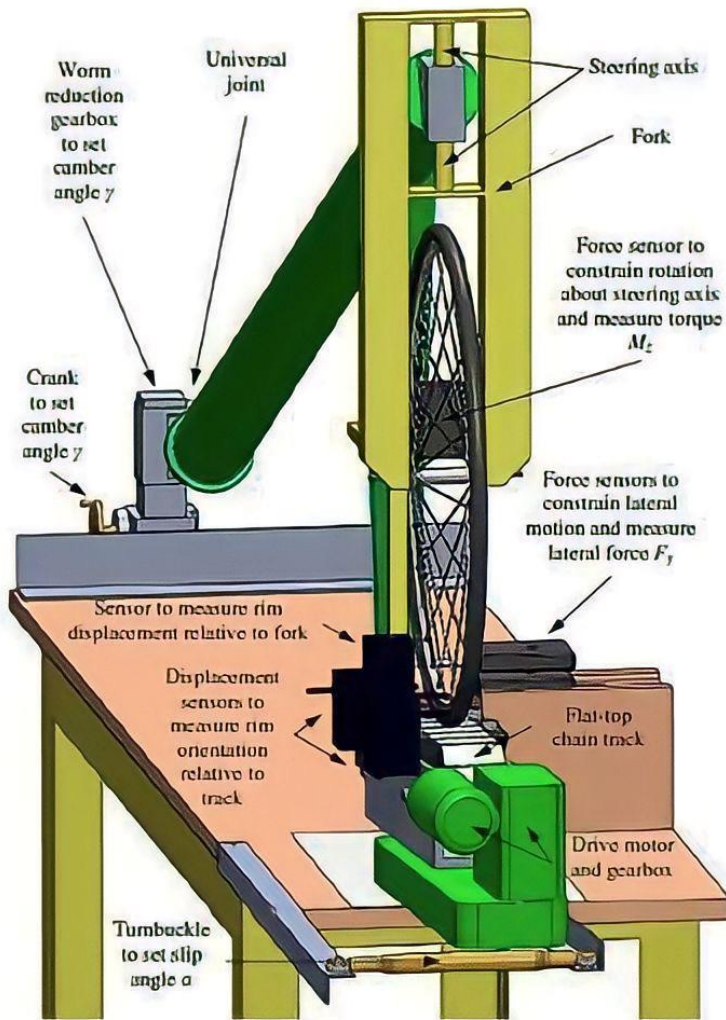


Figure 1.2: Test-rig at University of Wisconsin-Milwaukee. The aluminium fork holds the wheel on top of a flat track system similar to chain, which is driven by a low power electric motor. [35]

1.3. Test-rig at Delft University of Technology

The test-rig at Delft University of Technology [35] consists in a welded steel frame with a fork to hold the bicycle wheel which is placed on top (Figure 1.3) of a rotating drum of 2.5 m diameter. The frame is fixed to the ground by means of the universal joint in order to prevent the roll rotation of the system. An actuator allows to change the camber angle by rotating the frame with respect to the universal joint. The slip angle is adjusted by moving the universal joint along a curved path, in order to maintain the tyre contact patch on top of the drum. Also, the vertical load can be modified with the use of additional masses of known weight applied to the frame.

A force sensor is placed on the chassis to prevent the rotation of the wheel around the steering axis and it measures the self-aligning torque M_z . The lateral force F_y is measured by a force sensor that constrains the lateral displacement of the tyre.

This test-rig allows tests to be performed up to a speed of 22 m/s (79.2 km/h), which is likely to be experienced by an automobile tyre.

The main disadvantage of the test-rig consists in the use of a rotating drum. The curvature of the drum influences the size and the shape of the contact patch: the use of a small diameter drum with respect to the wheel diameter introduces a different contact patch with respect to when a flat surface is used. This difference may result in measured tyre properties different from the real ones. The slip angle was limited to less than $\pm 3^\circ$ to avoid bias in the lateral force measurement.

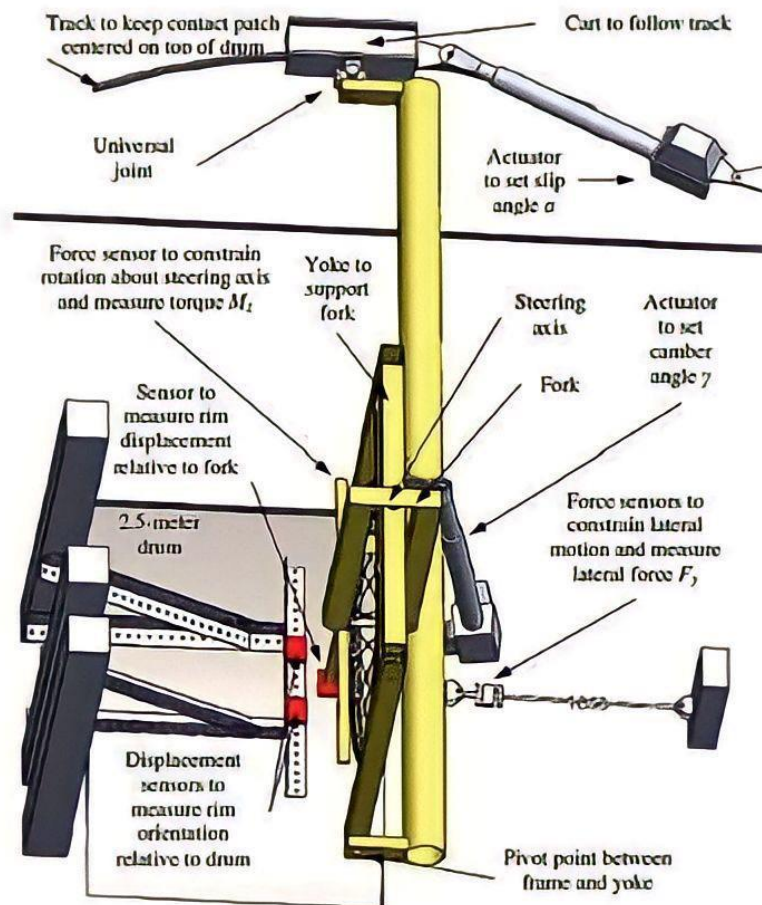


Figure 1.3: Test-rig at Delft University of Technology. A steel frame constrains the wheel rolling on a drum. Side slip and camber angles can be set by acting on the universal joint.

[35]

1.4. Test-rig at Karlsruhe Institute of Technology

The test-rig at Karlsruhe Institute of Technology was conceived to test car tyres, with the possibility of being adapted for bicycle tyres [36]. It performs the measurements by using a single-sided fork, holding the wheel, terminating with a measuring hub. It measures all the three forces and three torques, with a maximum range of 15 kN for the forces and 1.5 kNm for the aligning torque. The wheel rolls inside of a 3.8 m diameter rotating drum (Figure 1.4) which is driven by 310 kW electric motor.

This system allows high flexibility on various parameters. The slip angle and the camber angle can be simultaneously adjusted. The use of a hydraulic motor connected to the wheel allows the application of braking/acceleration torque to the rolling wheel. The roughness of the track surface can be modified applying adhesive surfaces, to perform measurements on surfaces of different roughness levels. Additionally, there is the possibility to reduce the temperature up to -20°C in the inner drum chamber, so as to simulate ice or snow conditions, as well as to create a controlled water film on the track surface, to simulate rainy conditions.

The main drawback of this system lies in the fact that performing tests on a drum deforms the contact patch with respect to flat track simulations.



Figure 1.4: Test-rig at Karlsruhe Institute of Instrumented. The measuring hub is used to hold the bicycle wheel letting it rolls on the internal part of a drum. [36]

2 Introduction to VeTyT

The VeTyT (acronym for Velo Tyre Tester) is a test-rig for bicycle tyres developed at the LaST (“Laboratorio Sicurezza Trasporti”, Transport Safety Laboratory), belonging to the Department of Mechanical Engineering of Politecnico di Milano (Figure 2.1). The main purpose of this test-rig is to measure the characteristic curves and properties of bicycle tyres of different kinds, mainly their lateral force and self-aligning torque. This Chapter will provide an overview of the VeTyT system, in the configuration in which was used for the testing campaign that is object of this thesis project.

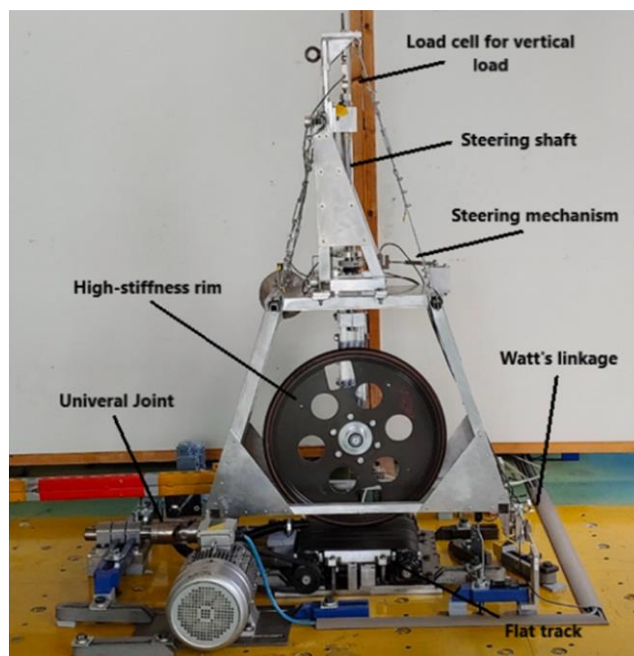


Figure 2.1: VeTyT on flat track, configuration without linear actuator in the steering system.

2.1. Frame

The VeTyT frame consists in a two-part aluminium 6060T6 frame, made by extruded beams with hollow square sections ($40 \times 40 \text{ mm}$ and $30 \times 30 \text{ mm}$) welded between each other. The two parts that compose the frame (lower and upper) are connected by means of four bolts as illustrated in Figure 2.2. The chassis has been reinforced with additional aluminium plates and steel rods, following a structural study of the system that highlighted the necessity of a stiffer body, in order not to alter the results of the

tests [37]. It is constrained to the ground by a cardan joint and a Watt's linkage, that allows it to regulate the camber angle by inclining the whole structure around its longitudinal axis (roll rotation). The frame is made in such a way that it can house rims of different sizes, from 16" to 29" [38].

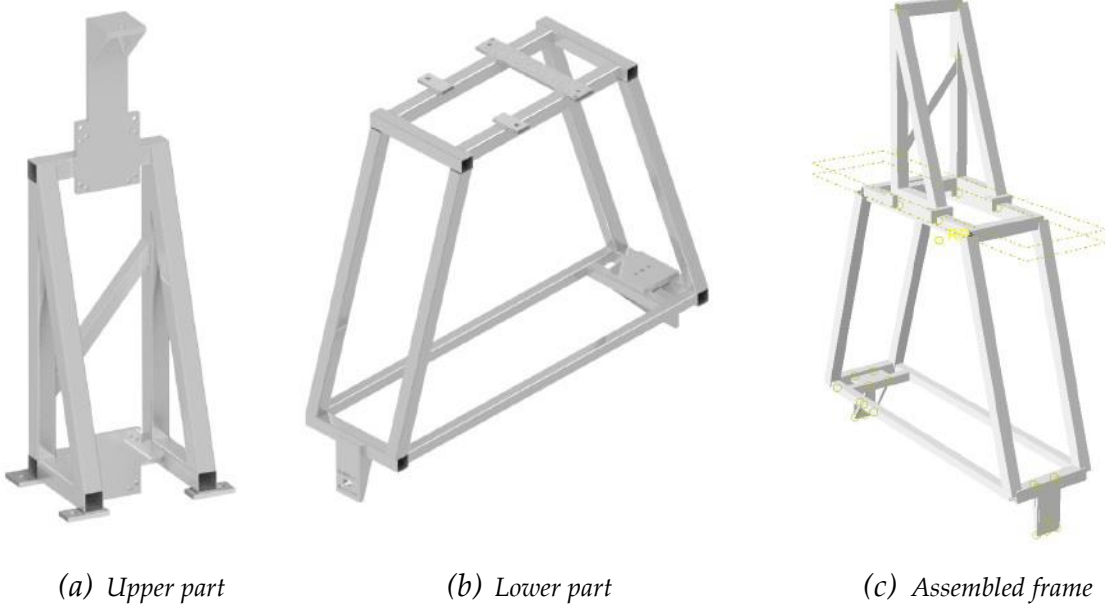


Figure 2.2: The two parts composing VeTyT's frame: upper part (a), lower part (b). The final assembled frame (c).

2.2. Running contact surface

The VeTyT is designed so that it can perform tests on two different types of surfaces: the rotating drum [39] and the flat track [40]. The first is a drum designed for testing car and motorbike tyres that can reach a peripheral speed of 122 m/s , then extended to the bike tyre tests. It has an external diameter of 2.6 m and is 550 mm -wide (Figure 2.3). The 2022-2023 experimental campaign was conducted only on the flat track, which is a poly-V [41] belt driven by a 5.5 kW three-phase asynchronous electric motor (Figure 2.4). It offers the possibility of appreciating the whole tyre contact patch without deformations due to the surface curvature, thus eliminating the main drawback of the rotating drum.

A pneumatic system providing the belt with a flow of pressurized air and silicon oil was developed in order to minimize the wear of the belt and lower the friction action, which can generate heat during a test. In this configuration the system can reach up to 20.8 m/s speed. However, it was noted that the pneumatic system wasn't sufficient to dissipate the heat produced by friction, influencing the repeatability of the tests. Therefore, a cooling system was added, consisting in a radial fan flowing air through

a 3D-printed convergent nozzle directed towards the longitudinal axis of the belt as shown in Figure 2.5.

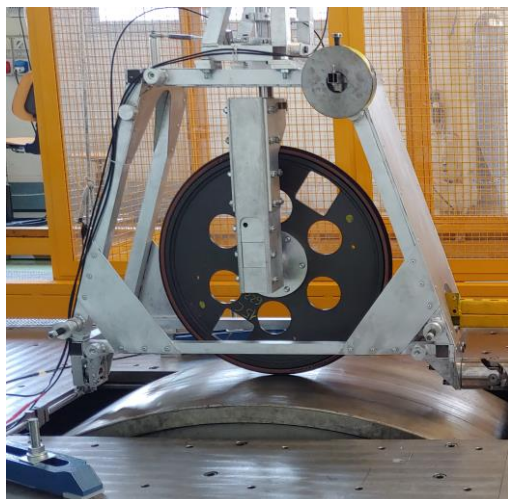


Figure 2.3: Rotating drum.



Figure 2.4: Detail of VeTyT's flat track belt.

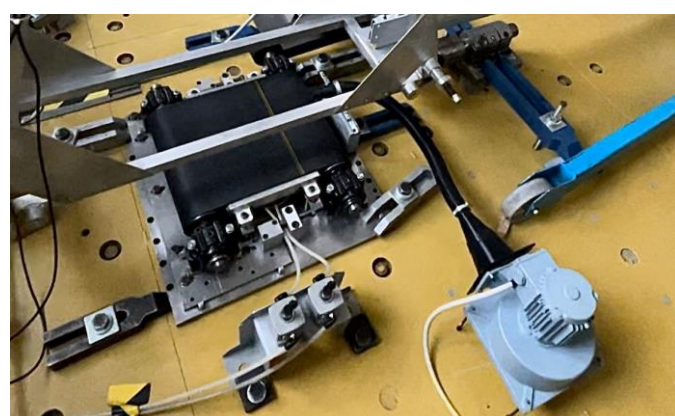


Figure 2.5: Pneumatic and cooling systems overview.

2.3. Cardan joint

The cardan joint constraints the chassis to the ground, while allowing the pitch and yaw rotations. The setting of the camber angle is permitted by the rolling motion of the base shaft of the system, which is rigidly connected to this joint (Figure 2.6).

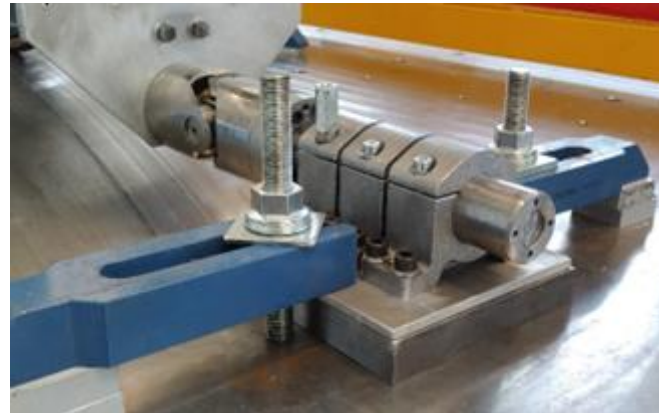


Figure 2.6: Cardan, or universal, joint belonging to the VeTyT system.

2.4. Watt's linkage

The Watt's linkage constraints the frame to the ground and limits its lateral movement. It is composed of three rods as shown in Figure 2.7: the two horizontal rods are constrained to the ground and instrumented with load cells that measure the tensile and compressive forces applied on them, in order to then calculate the overall lateral force acting on the tyre.

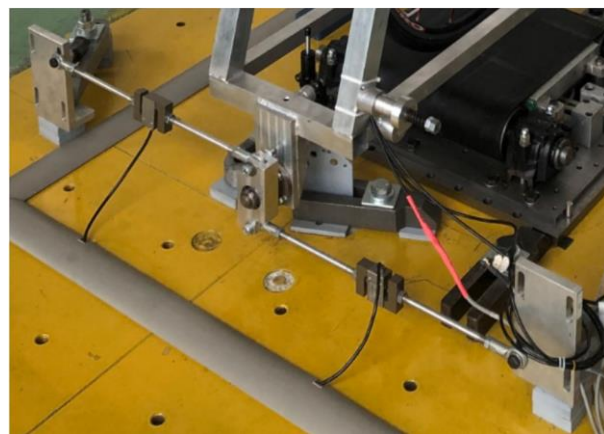


Figure 2.7: Detail of VeTyT's Watt's Linkage, instrumented with two load cells.

2.5. Steering system

VeTyT is able to steer the wheel in order to measure the characteristic forces at different slip angle values. In fact, the geometry of the system makes it so that the slip angle and steering angle correspond to each other. The steering shaft is held by a collar connected to a motorized extendible rod, fixed to the chassis. The rod consists in a linear electric motor, provided by Wittenstein®, that completely automatizes the steering action, by following a motion law imposed by the operator (Figure 2.8). The steering axis is coincident with the axis of the steering shaft, and is perpendicular to the camber axis, intersecting in the centre of the contact patch (Figure 2.9). To eliminate the risk of having unwanted longitudinal slip, the contact patch must belong to the steering axis.



Figure 2.8: Steering system, equipped with the linear motor.

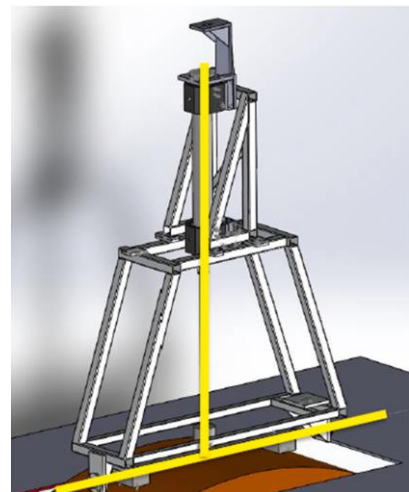


Figure 2.9: VeTyT's two principal axes, the steering axis and the camber axis, highlighted on the structure.

2.6. Fork

The fork is the element of the system that fixes the wheel to the frame, ensuring its correct positioning. To accommodate different types of tyres and tyre frames, two main fork configurations were designed:

- *Single sided fork*: specifically designed to house the high stiffness rim (Figure 2.10),

- *Double sided fork:* standard fork, that can house the majority of the tested tyre. A version with longer arms was produced to be able to test cargo-bike tyres, which are characterised by lower radius than the conventional commercial tyres (Figure 2.11).



Figure 2.10: Single sided fork equipped with the high stiffness rim, mounted on the VeTyT.



Figure 2.11: Double sided fork equipped with a commercial wheel, mounted on the VeTyT.

2.7. Measuring instruments

To measure the desired quantities, the VeTyT test-rig is equipped with sensors. A linear magnetic encoder is used to measure the slip angle: the magnetic band, placed on the steering shaft, and the reader is properly positioned in order to accurately read the linear displacement of the band, as shown in Figure 2.12. The angular displacement, i.e., the slip angle, is then obtained through geometric conversions.

Instead, to measure forces and moments, four load cells (CS20, provided by Pavone Sistemi S.R.L) properly placed are used:

- *Lateral Force:* two load cells (full-scale of 100 kg) are placed on the Watt's linkage rods, to measure the resultant force F_w , as algebraic sum of the two measured signals, because when one is in traction, the other is in compression.

$$F_w = |F_{w,sx}| + |F_{w,dx}| \quad (2.1)$$

The lateral force, when a side slip angle is imposed, is obtained by solving an equilibrium equation [38], knowing the value of the resultant force applied on

the Watt's linkage F_w and the force measured by the load cell mounted on the steering rod F_s .

$$F_y = \frac{F_w \cdot L - F_s \cdot b}{L_2 \cdot \cos \alpha} \quad (2.2)$$

Where L is the distance between Watt's linkage and cardan joint, L_2 is the distance between fork and cardan joint, b is the lever arm of the force F_s with respect to the steering shaft axis and α is the side slip angle.

- *Self-aligning torque*: a load cell (full-scale of 50 kg) is placed on the extendable rod of the steering system (Figure 2.13). The self-aligning torque is obtained as the moment generated by the measured force on the steering rod F_s acting on the distance between the steering shaft axis and the load cell longitudinal axis b .

$$M_z = F_s \cdot b \quad (2.3)$$

- *Vertical load*: a load cell (full-scale 250 kg) is placed on top of the steering shaft to measure the vertical load of the VeTyT system, excluding the shaft, the fork, the rim and the tyre that are placed under the sensor (Figure 2.14). To obtain the value of the actual vertical load acting on the contact patch of the tyre, the weight of the components placed under the load cell must be added to the measured force.



Figure 2.12: Linear magnetic encoder. The magnetic band is placed on the shaft while the receiver is properly centred with respect to the band to correctly measure the linear displacement of the band itself.



Figure 2.13: Load cell for the measurement of the force on the steering rod F_s .



Figure 2.14: Load cell for the measurement of the vertical load F_z , placed on top of the steering shaft.

2.8. Vertical Load Setting System

To set the desired vertical load on the wheel, masses of known weight are added to the VeTyT, until the desired configuration is reached, as seen in Figure 2.15. The masses are positioned on the lever arm that is rigidly connected to the frame, reducing the total vertical load acting on the wheel.

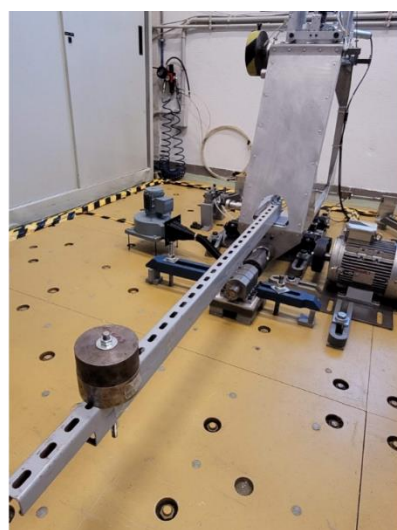


Figure 2.15: Vertical load setting system, with masses applied on the lever arm.

3 Dynamic Analysis

The purpose of VeTyT is to obtain the characteristic curves and properties of different bicycle tyres. To do so, different types of analysis can be performed, one of these being the dynamic analysis.

The VeTyT dynamic analysis consists in a series of tests performed with the wheel running on a flat track or on a rotating drum. The tests that will be studied in this Chapter, are all dynamic tests performed on the flat track belt, that is a poly-V belt [41] moved by a 5.5 kW three-phase asynchronous electric motor. This allows the belt, and therefore the wheel, to move at a constant longitudinal speed that can reach up to 20.8 m/s , with the help of a pneumatic system to reduce friction.

During the dynamic test, the wheel is able to steer to span the range of slip angles that is of interest. The steering action is automatized, through the actuation of a linear electric motor provided by Wittenstein®, which follows a motion law imposed by the operator through the official software of the actuator (MotionGUI2®).

Each dynamic test is defined by a set of tuneable parameters:

- Camber angle (γ)
- Static vertical load (F_z)
- Inflation pressure (P)
- Speed of the flat track (v)

However, during the testing campaign that is object of this thesis, the flat track speed has always been maintained the same for all the tyres, at 9.3 km/h (2.6 m/s). Camber angle, vertical load and inflation pressure are chosen accordingly with the characteristics of the tyre and the aim of the analysis. The camber angle is measured with an inclinometer, and it is considered positive when the inclination of the VeTyT system is counterclockwise, when observing it from the front.

This Chapter will cover different types of analyses that were performed starting from the data collected through the performed dynamic tests. The curves that will be presented were all obtained though the Post Processing software (described in Section 5.2) which filtered the data with a low pass filter at a cut-off frequency of 1 Hz.

Section 3.1 will offer a brief recall of the fundamental literature concepts on lateral force and self-aligning torques for road vehicle tyres.

Section 3.2 will explain how the “Standard Dynamic Analysis” is performed, by taking as example two of the tested tyres and showing their characteristic curves, properties and other interesting results.

Section 3.3 will present some characteristic curves that presented an unexpected behaviour and will try to understand the causes of this unusual trends, showing also the same curves obtained when repeated.

Section 3.4 will report an analysis between the characteristic curves of the tested tyres, taking into consideration the type of bicycle the analysed tyres were designed for.

3.1. Road Vehicles tyre literature

Most of studies on road vehicles have been focused on car tyres, therefore much data and information about it are available in literature. The characteristic curves for road vehicle tyres are well known and their trends, following operating parameters changes, have been thoroughly studied. In particular, motorcycle tyres can be considered similar to the bicycle's, due to their profile section and the high camber values they are subject to. For the sake of simplicity, they may be used as a comparison for the analysis of bicycle tyres performed through VeTyT.

This section will serve as a quick reminder of the key notions present in literature on the behaviour of the characteristic curves for road vehicle tyres, aimed at offering a term of comparison for the analyses that will follow later in this Chapter.

3.1.1. F_y : Lateral Force

The lateral force F_y characteristic curve, plotted against the slip angle α , follows the trend shown in Figure 3.1.

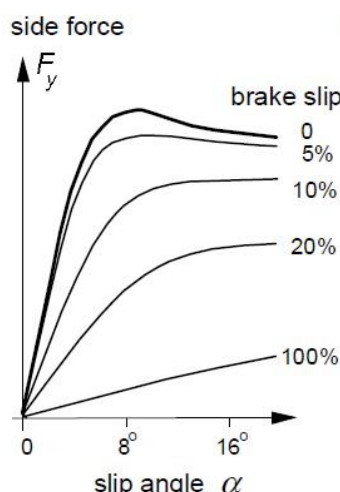


Figure 3.1: Lateral force versus slip angle characteristic curve for a general tyre, for various brake slip levels.

In case no additional contributions are present, the curve crosses the origin, to then start increasing in value for increasing slip angle. The lateral force increases linearly for low slip angle values, to then assume a nonlinear behaviour for higher slip angles, reaching its peak value and then slowly decreasing. In a perfectly symmetric tyre, this curve is symmetric with respect to the origin.

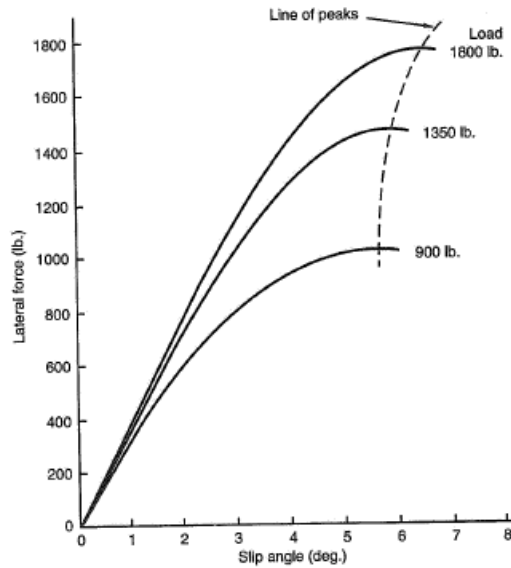


Figure 3.2: Lateral force vs slip angle curve for different vertical load values, for a P215/60 R15 Goodyear Eagle GT-S tyre inflated at 31 psi (214 kPa). [42]

The effect of the vertical load on the lateral force curve is shown in Figure 3.2 and consists in an overall increase of F_y values for all slip angles different from 0° . This is due to the fact that the contact patch area increases, causing an increase of the lateral force that can be applied to the ground. However, the increase in value is nonlinear with the vertical load till saturation (for high vertical loads). The ratio between the maximum reachable lateral force value and the vertical load corresponds to the friction coefficient between tyre and road surface.

$$\frac{F_{yMAX}}{F_Z} = \mu \quad (3.1)$$

Instead, the effect of the camber angle γ on the lateral force curve is shown in Figure 3.3 and consists in a vertical shift of the curve, upwards when the wheel leans into the turn and downwards when the wheel leans out of the turn.

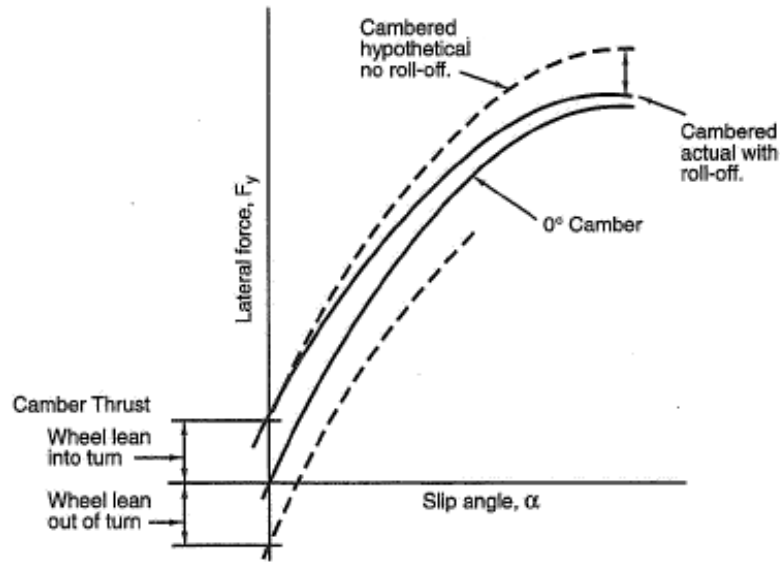


Figure 3.3: Camber effect on a lateral force vs slip angle characteristic curve. [42]

3.1.2. M_z : Self-aligning torque

From literature, it is known that the self-aligning torque behaviour is closely related to the lateral force's. M_z arises when the lateral force is not applied to the centre of the tyre's contact patch, due to an uneven deformation of the contact patch of the rolling tyre, caused by the hysteresis of the rubber.

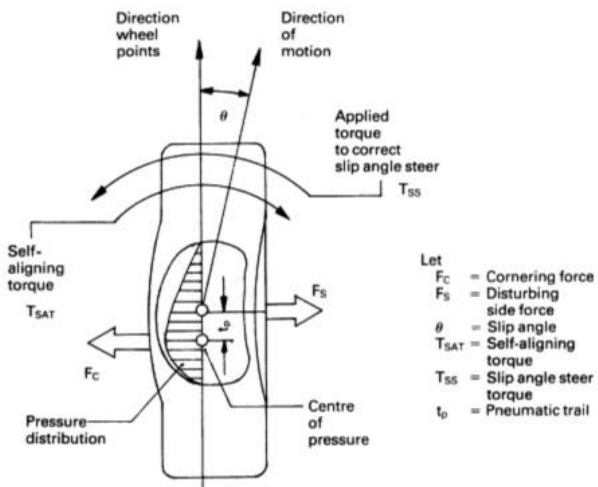


Figure 3.4: Top view of a tyre, showing the generation of the self-aligning torque M_z . The lateral force (or cornering force) F_y is applied at distance t_p from the geometric centre of the contact patch, thus having the pneumatic trail has the arm of the arising M_z .

Therefore, the relation between the self-aligning torque and the lateral force can be expressed by the following equation:

$$M_z = F_y t \quad (3.2)$$

Where t is the pneumatic trail, i.e., the distance between the geometric centre of the contact patch and the actual point of application of the lateral force (Figure 3.4). It is important to point out that the pneumatic trail t is not constant: in fact, it is highly dependent on the tyre behavior and characteristic properties, hence it changes value under different slip, pressure, vertical load and camber conditions.

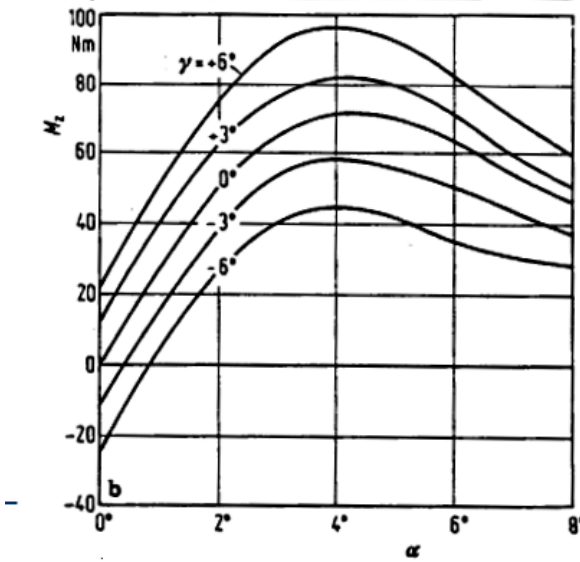


Figure 3.5: Camber effect on a self-aligning torque vs slip angle characteristic curve. [42]

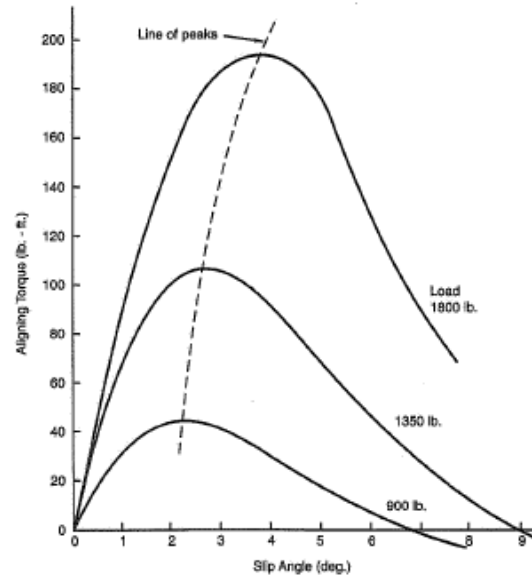


Figure 3.6: Self-aligning torque vs slip angle curve for different vertical load values, for a P215/60 R15 Goodyear Eagle GT-S tyre inflated at 31 psi (214kPa). [42]

Due to this strong relation between M_z and F_y , the effects of camber and vertical load on the self-aligning torque curves are very similar to the ones on F_y . In fact, the camber causes a vertical shift of the curve, upwards for positive camber angles and downwards for negative camber angles (Figure 3.5), while increasing the vertical load leads to an overall increase in self-aligning torque for side slip angles different from 0° , with non-linear relation between M_z and F_z , due to the maximum reachable lateral force value due to the friction limit. (Figure 3.6).

3.1.3. C_α : Cornering stiffness

The cornering stiffness is defined as the slope of the curve F_y vs α at $\alpha = 0^\circ$ (Figure 3.7).

$$C_\alpha = \frac{dF_y}{d\alpha} \Big|_{\alpha=0} \quad (3.3)$$

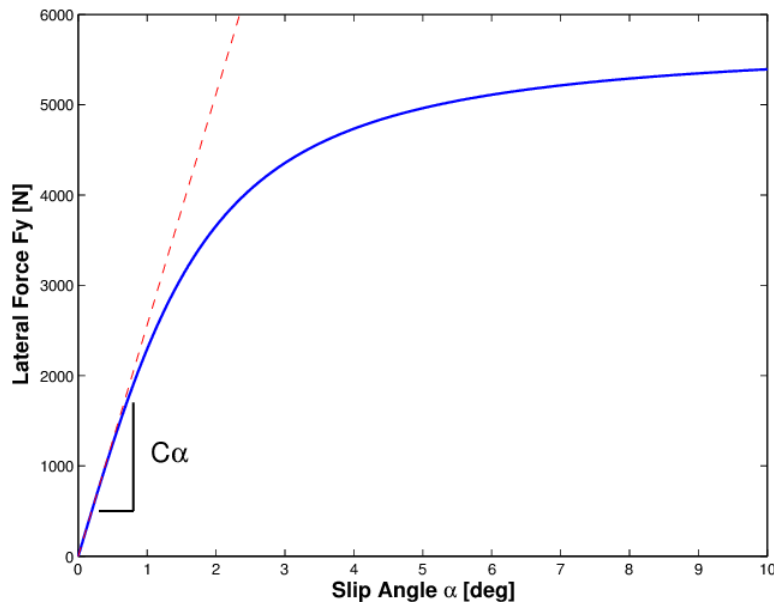


Figure 3.7: Graphic representation of the cornering stiffness definition. [43]

In road vehicle dynamics, the cornering stiffness is a very important tyre parameter because it directly influences the value of the lateral force, and therefore has an enormous impact on the handling behaviour of the vehicle. A road tyre with high cornering stiffness reaches higher value of lateral force for smaller value of side slip angle.

As for the lateral force, also the cornering stiffness has a non-linear relation with the vertical load, as it is shown in Figure 3.8. It increases with an almost linear trend at low vertical force values, with growing non-linearity until a peak C_α is reached. After the peak, cornering stiffness values start to slowly decrease, if vertical force is further increased.

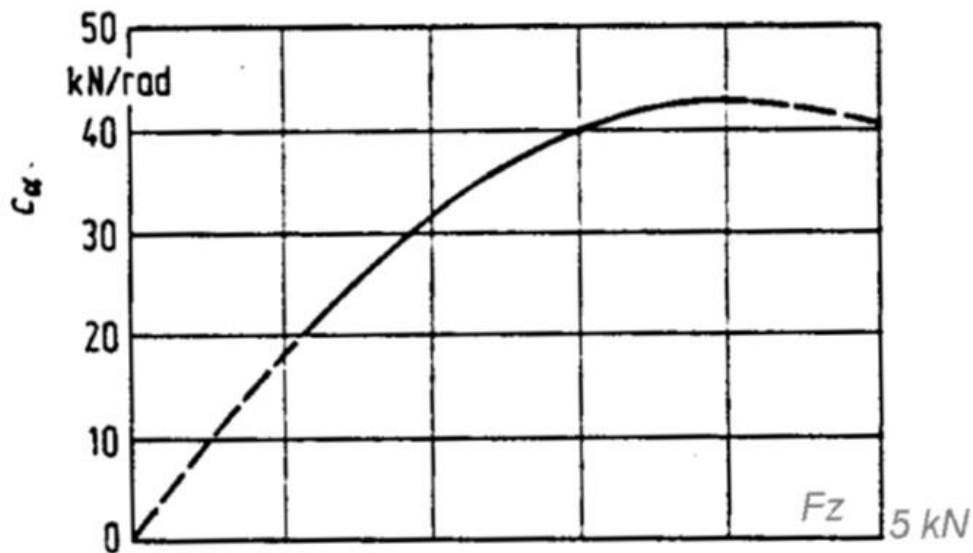


Figure 3.8: Cornering stiffness vs vertical load for a general road vehicle tyre.

3.2. Standard Dynamic Analysis

The term “Standard Dynamic Analysis” indicates the standard procedure followed to elaborate, present and finally analyse the data collected through the dynamic tests. The outputs of this analysis, for each tested tyre, are the following:

- Lateral force F_y vs slip angle α plots at constant pressure, constant camber angle and varying vertical load F_z
- Self-aligning torque M_z vs slip angle α plots at constant pressure, constant camber angle and varying vertical load F_z
- Lateral force F_y vs slip angle plots α at constant pressure, constant vertical load F_z and varying camber angle γ
- Self-aligning torque M_z vs slip angle α plots at constant pressure, constant vertical load F_z and varying camber angle γ
- Cornering stiffness table at camber angle equal to 0° for varying pressure and varying vertical load F_z
- Cornering stiffness tables at constant pressure, varying camber angle γ and varying vertical load F_z .

This set of curves and properties, together with observations and considerations, are reported in the official test report, one for each tested tyre. The test report is the document that collects the results of all the tests performed on a specific tyre and is the official document that is ultimately delivered to the final costumer.

The next sections will provide two examples of standard dynamic analysis: the cargo bike tyre SCH-T01 in Section 3.2.1 and the e-bike tyre SCH-T03 in Section 3.2.2.

3.2.1. Cargo bike Tyre – SCH-T01

The SCH-T01 is a cargo bike tyre, which means that it must endure higher loads than the average bicycle tyre. Therefore, it is characterized by a smaller diameter (406 mm) and a wider profile section (55 mm) [27].

This tyre was mounted on a *Mach1 Kargo Disc 20"* ($406 - 25c$) rim and tested under every combination of the following parameters:

- Camber angle: -5° , 0° , 5°
- Vertical load: 411 N , 526 N
- Inflation pressure: 400 kPa

For the sake of simplicity, in Sections 3.2.1.1 and 3.2.1.2 are only reported specific combinations of parameters.

The CST-T02 tyre, a cargo bike tyre from a different manufacturer with similar characteristics, was also tested under the same conditions: a comparison between the characteristic curves of the two can be found in Section 3.4.

3.2.1.1. Constant pressure and camber, vertical load variation

The characteristic curves at constant camber, constant pressure and different vertical load values can be compared through the performed tests. In Figure 3.9 the lateral force plot is shown as a function of the side slip angle, for pressure equal to 400 kPa , camber 0° and varying vertical load (411 N , 526 N), while Figure 3.10 represents the self-aligning torque as function of the side slip angle curve, for pressure equal to 400 kPa , camber 0° and varying vertical load (411 N , 526 N)

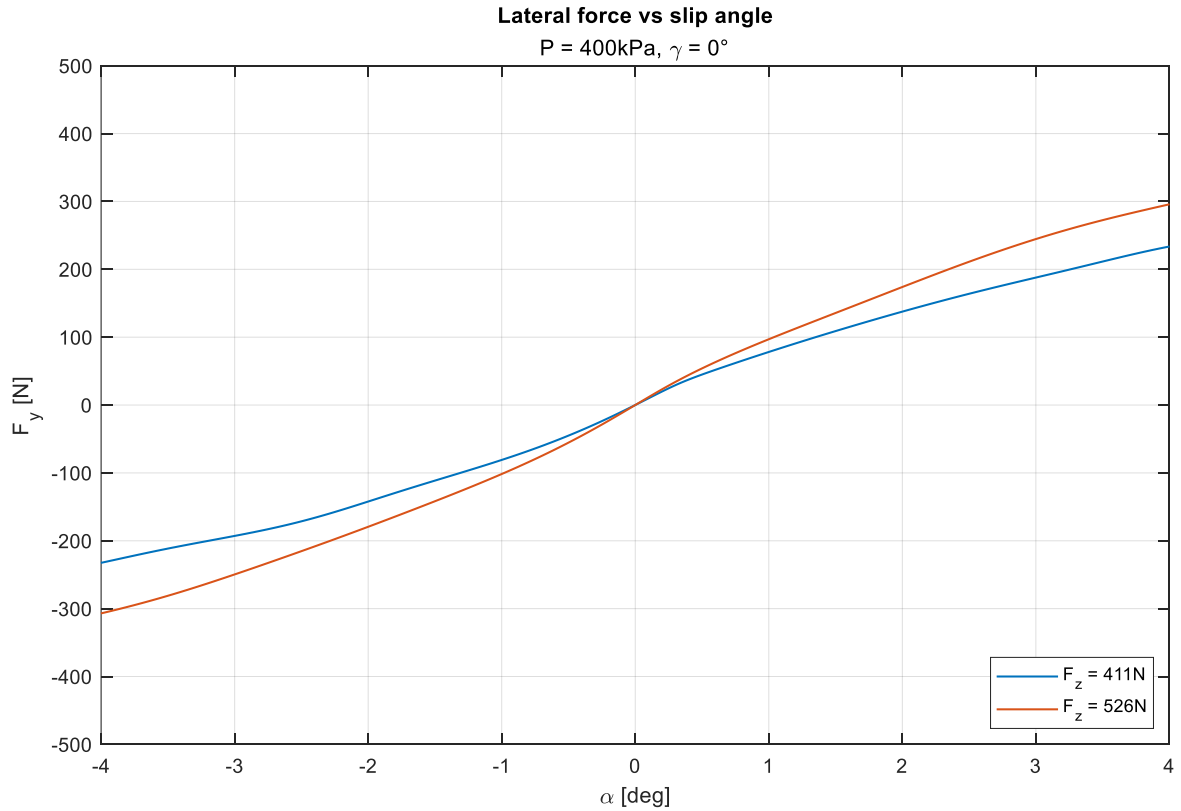


Figure 3.9: Lateral force plot as a function of the side slip angle, for pressure equal to 400 kPa , camber 0° and varying vertical load (411 N , 526 N) for SCH-T01.

In order to have a better understanding of Figure 3.9, the values of the lateral force for side slip angles equal to 4° and -4° are collected in Table 3.1.

Inflation Pressure [kPa]	Vertical load [N]	Camber [$^\circ$]	Side slip angle [$^\circ$]	F_y [N]
400	411	0	4	231.0
400	526	0	4	292.6
400	411	0	-4	-230.5
400	526	0	-4	-294.7

Table 3.1: Lateral force values at slip angle equal to 4° and -4° , at constant pressure 400 kPa , constant camber 0° and varying vertical load (411 N , 526 N) for SCH-T01.

From the characteristic curves shown in Figure 3.9 it can be observed that the lateral force F_y increases with the slip angle alpha in a seemingly linear fashion. This

behaviour is coherent with the one of the road vehicle tyres according to the literature, however without the 'peak' that is typical of those tyre characteristics curves. This is probably due to the fact that under these testing parameters, the vertical force saturation limit and the full slip condition are not reached inside the slip angle interval that is examined.

Moreover, the increase of the vertical load from 410 N to 526 N , at constant inflation pressure and camber angle, increases the value of the lateral force in modulus for side slip angles different from 0° .

From the data collected in Table 3.1 it can be noted that the curves at the same vertical load present very similar absolute values for positive and negative slip angle values and that the difference between the F_y values of the two characteristic curves, evaluated at slip angles $\pm 4^\circ$, is almost the same. Hence it can be said that the characteristic curve for the lateral stiffness is symmetric with respect to the origin.

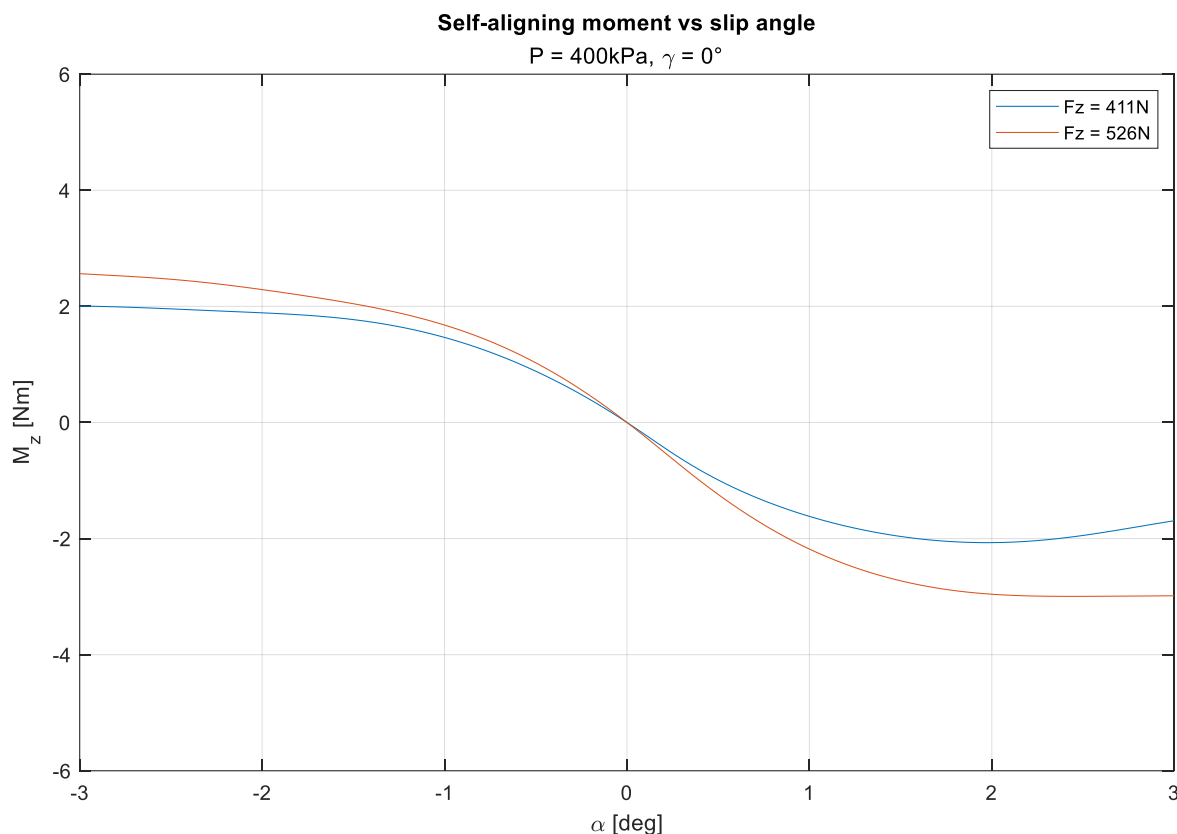


Figure 3.10: Self-aligning torque plot as a function of the side slip angle, for pressure equal to 400 kPa , camber 0° and varying vertical load (411 N , 526 N) for SCH-T01.

The peak values of the self-aligning torque and the relative values of side slip angle are collected in Table 3.2.

Inflation Pressure [kPa]	Vertical load [N]	Camber [°]	$\alpha_{M_{z_max}}$ [°]	M_{z_max} [Nm]
400	411	0	2.0	-2.1
400	526	0	2.5	-3.0
400	411	0	-3.0	2.0
400	526	0	-3.0	2.6

Table 3.2: Peak self-aligning torque values and corresponding slip angles, at constant pressure 400 kPa, constant camber 0° and varying vertical load (411 N, 526 N) for SCH-T01.

From Figure 3.10 it can be noted that the trend of the self-aligning torque curve is linear for low slip angle values, with growing non-linearity for increasing slip angles ($> |1.5^\circ|$). In this specific case, the curve seems to reach a peak for positive slip angles.

Looking at Table 3.2 it is possible to see that, for positive side slip angles, the increase of the vertical load causes the increase of the self-aligning torque peak value in modulus, which is the same effect that it also had on the lateral force F_y . This is justified by the close relation between M_z and F_y known from literature and explained in Section 3.1.1.2.

3.2.1.2. Constant pressure and vertical load, camber variation

Through the performed tests, the characteristic curves at constant pressure, constant vertical load and different camber angle values can be compared. Figure 3.11 shows the lateral force plot as a function of the side slip angle, for pressure equal to 400 kPa, vertical load $F_z = 411$ N and varying camber (-5° , 0° , 5°).

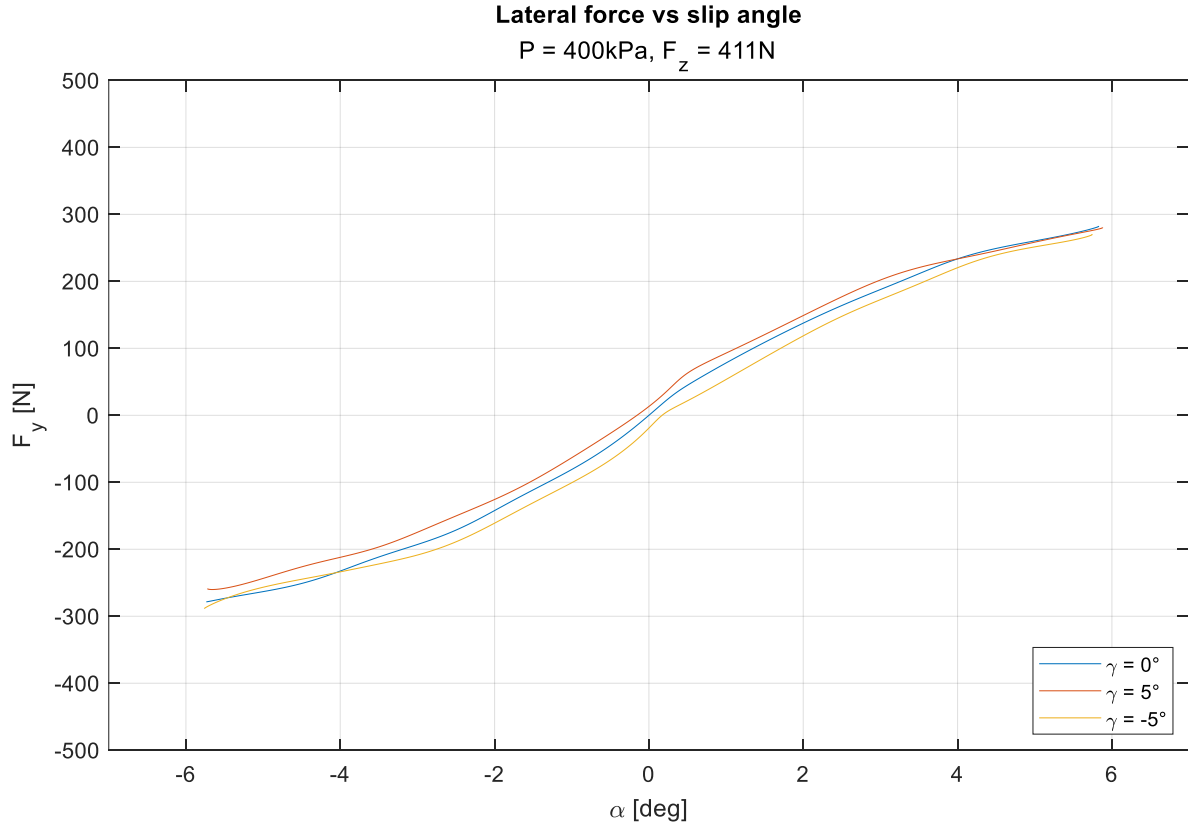


Figure 3.11: Lateral force plot as a function of the side slip angle, for pressure equal to 400 kPa , vertical load $F_z = 411 \text{ N}$ and varying camber ($-5^\circ, 0^\circ, 5^\circ$) for SCH-T01.

Inflation Pressure [kPa]	Vertical load [N]	Camber [$^\circ$]	Side slip angle [$^\circ$]	F_y [N]
400	411	-5	2	118.6
400	411	0	2	137.7
400	411	5	2	148.9
400	411	-5	-2	-161.0
400	411	0	-2	-142.2
400	411	5	-2	-125.6

Table 3.3: Lateral force values at slip angle equal to 2° and -2° , at constant pressure 400 kPa , constant vertical force 411 N and varying camber ($-5^\circ, 0^\circ, 5^\circ$) for SCH-T01.

The camber variation at constant inflation pressure and vertical load causes a vertical shift of the lateral force curve, mainly in the linear part, with respect to the camber 0° one, with the shift being directed downwards for negative camber angles and upwards

for positive camber angles. This effect can also be noted by observing the F_y values in Table 3.3: it can be seen that the difference between the curves at camber -5° and 0° is almost the same whether it is evaluated at slip angles $+2^\circ$ or at -2° . This also applies to the curves at camber 5° and 0° .

Figure 3.12 reports the self-aligning torque as a function of the side slip angle in the same conditions, for pressure equal to 400 kPa , vertical load $F_z = 411 \text{ N}$ and varying camber $\gamma = (-5^\circ, 0^\circ, 5^\circ)$.

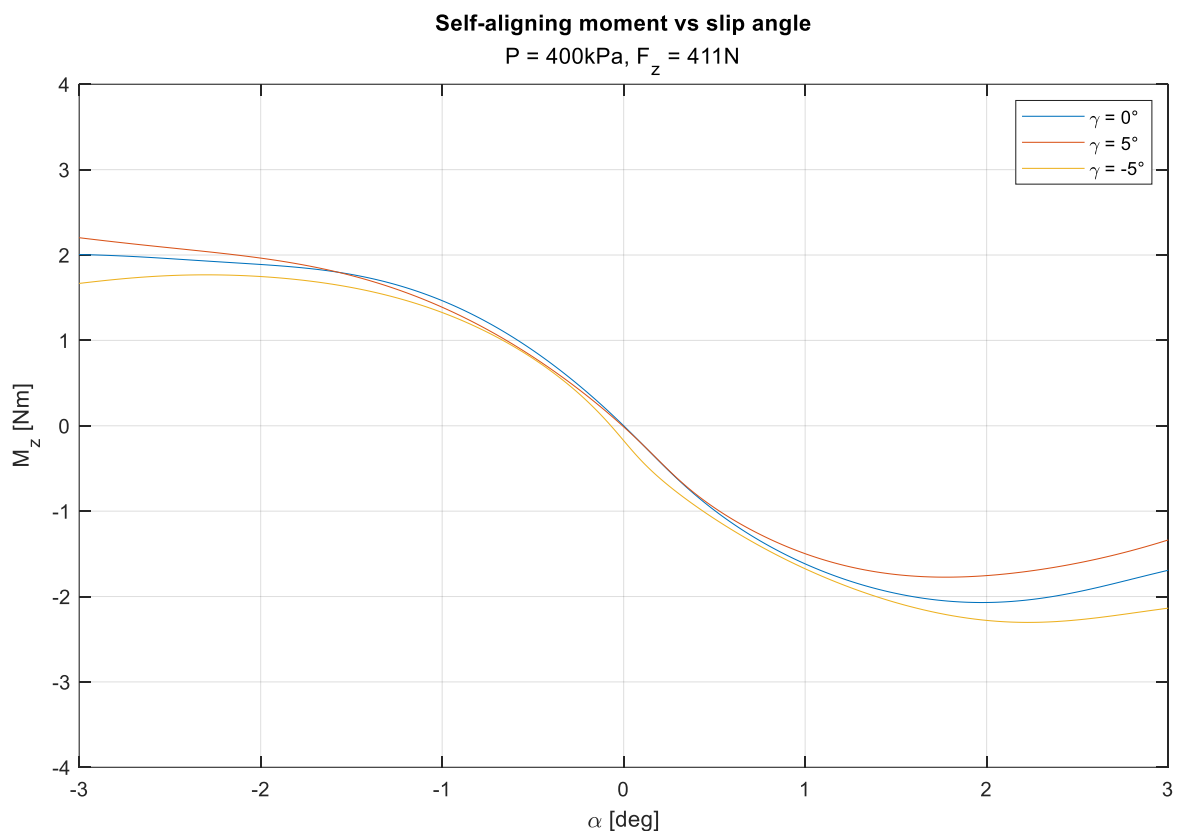


Figure 3.12: Self-aligning torque as a function of the side slip angle for pressure equal to 400 kPa , vertical load $F_z = 411 \text{ N}$ and varying camber $(-5^\circ, 0^\circ, 5^\circ)$ for SCH-T01.

In Table 3.4 are reported the M_z peak values ($M_{z,\max}$) for both the slip angles semi planes (positive slip angles and negative slip angles) with the corresponding slip angles ($\alpha_{M_{z,\max}}$). In case, in one of the semi planes, a clear M_z peak cannot be identified, the reported $M_{z,\max}$ value corresponds to the evaluation of M_z at the $\alpha_{M_{z,\max}}$ corresponding to the peak of another curve in the same semiplane.

Inflation Pressure [kPa]	Vertical load [N]	Camber [°]	$\alpha_{M_{z_max}}$ [°]	M_{z_max} [Nm]
400	411	-5	2.2	-2.3
400	411	0	2.0	-2.1
400	411	5	1.8	-1.8
400	411	-5	-2.3	1.8
400	411	0	-2.3	1.9
400	411	5	-2.3	2.0

Table 3.4: Peak self-aligning torque values and corresponding slip angles; constant pressure 400 kPa, constant vertical load 411 N and varying camber (-5°, 0°, 5°) for SCH-T01.

3.2.1.3. Cornering stiffness

The cornering stiffness was evaluated for each combination of pressure, camber angle and vertical load considered for the SCH-T01 tyre.

In Table 3.5 are reported the cornering stiffness values found varying the vertical load with camber 0° and pressure equal to 400 kPa, while Table 3.6 reports the values found varying the camber angle for different values of vertical load at 400 kPa. All the values of cornering stiffness presented in the next tables must take into account an uncertainty U of $\pm 1.5\%$ that includes measuring errors, approximations, track wear, tyre wear, and any other possible cause of uncertainty.

Cornering stiffness [N/°]					
		Vertical Load [N]			
		411		526	
		Value	%	Value	%
Inflation Pressure [kPa]	400	85.1	-	105.5	21

Table 3.5: Cornering stiffness values at constant pressure (400 kPa), constant camber equal to 0° and varying vertical load (411 N, 526 N) for SCH-T01. The '%' column indicates the percentage variation of the considered cornering stiffness value with respect to the one at lower vertical load.

Cornering stiffness [N/°]						
P = 400 kPa		Vertical Load [N]				
		411			526	
		Value	%	y0	Value	%
Camber [°]	-5	83.5	-1.9	-19.1	107.3	1.7
	0	85.1	-	-	105.5	-
	5	84.2	-1.0	13.2	103.8	-1.6
						36.4

Table 3.6: Cornering stiffness values at constant pressure (400 kPa), varying camber (-5° , 0° , 5°) and vertical load (411 N, 526 N) for SCH-T01. The '%' column indicates the percentage variation of the considered cornering stiffness value with respect to the one at same vertical load and camber 0° . The 'y0' column indicates the value that corresponds to the intersection of the curves with the F_y axis.

It can be noted that the cornering stiffness increases with the vertical load, at constant inflation pressure and camber angle. Instead, for constant vertical load and inflation pressure, the cornering stiffness value for different camber does not change much ($\pm 2\%$), which is coherent with the fact that the camber influence on the lateral force only consists in a vertical translation of the characteristic curve.

The non-linearity of the relation between cornering stiffness and vertical load known from literature can be observed also these experimental data, by noting that a 28% increase in vertical load corresponds to a 21% increase in cornering stiffness.

3.2.2. E-Bike Tyre – SCH-T03

The SCH-T03 is designed appositely for e-bikes and it is featured by 622 mm-diameter and a 47 mm-section, whose profile presents 'a smooth central section and strong diamond sides' [30]. This tyre was mounted on a *Shimano Deore HB-M525A 28"* (622) rim tested under every combination of the following parameters:

- Camber angle: -5° , 0° , 5°
- Vertical load: 343 N, 404 N, 526 N
- Inflation pressure: 300 kPa, 400 kPa, 500 kPa

For the sake of simplicity, in Sections 3.2.2.1 and 3.2.2.2 are reported specific combinations of parameters.

The same analysis was conducted on other two e-bike tyres: the SCH-T04 tyre, an older version of the SCH-T03, and the SCA-T05 tyre, a e-bike tyre from a different manufacturer with similar characteristics. A comparison between the characteristic curves of the three can be found in Section 3.4.1.2.

3.2.2.1. Constant pressure and camber, vertical load variation

The characteristic curves at constant pressure, constant camber and different vertical load values can be compared through the performed tests. In Figure 3.13 the lateral force plot is shown as a function of the side slip angle, for pressure equal to 300 kPa , camber 0° and varying vertical load (343 N , 404 N , 488 N), while Figure 3.14 represents the self-aligning torque as function of the side slip angle curve, for pressure equal to 300 kPa , camber 0° and varying vertical load (343 N , 404 N , 488 N).

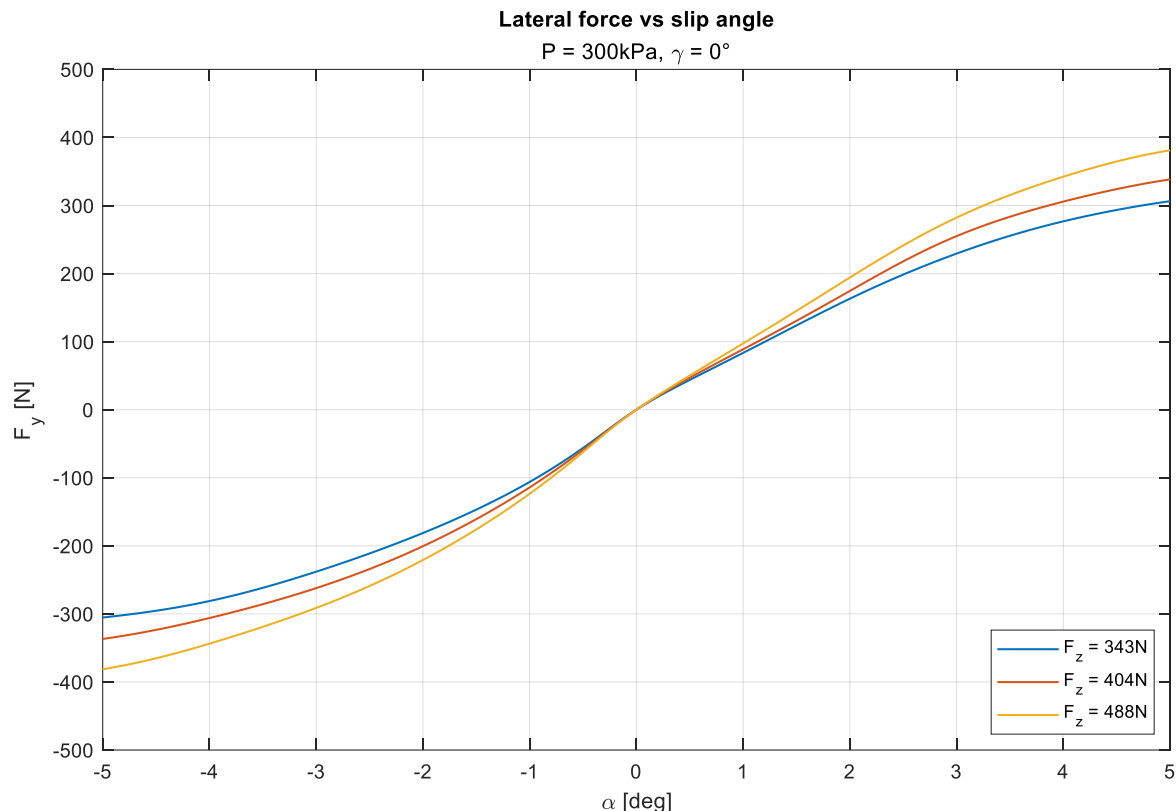


Figure 3.13: Lateral force plot as a function of the side slip angle, for pressure equal to 300 kPa , camber 0° and varying vertical load (343 N , 404 N , 488 N) for SCH-T03.

In order to have a better understanding of the Figure 3.13, the values of the lateral force for side slip angles of 4° and -4° are collected in Table 3.7.

Inflation Pressure [kPa]	Vertical load [N]	Camber [$^\circ$]	Side slip angle [$^\circ$]	F_y [N]
300	343	0	4	276.8
300	404	0	4	305.8
300	488	0	4	342.4
300	343	0	-4	-281.1
300	404	0	-4	-306.0
300	488	0	-4	-343.7

Table 3.7: Lateral force values at slip angle equal to 4° and -4° , at constant pressure 300 kPa , constant camber 0° and varying vertical load (343 N , 404 N , 488 N) for SCH-T03.

From the characteristic curves shown in Figure 3.13 it can be observed that the lateral force F_y increases with the slip angle in a similarly linear way. The non-linear part of the characteristic curve is more visible, in fact, for slip angles $> 3^\circ$ and $< -3^\circ$ a decrease in the slope of the curve can be noted. Therefore, it can be assumed that for those values of slip angle the tyre is getting closer to the maximum lateral force limit and to the full slip condition.

Moreover, the increase of the vertical load from 343 N to 488 N , at constant inflation pressure and camber angle, increases the value of the lateral force in modulus for side slip angles different from 0° . This effect can also be seen as a rotation of the curve about the origin in the anticlockwise direction and is coherent with the road vehicle tyres behaviour known.

From the data collected in Table 3.7 it can be noted that the curves at the same vertical load present very similar absolute values for positive and negative slip angle value, hence it can be said that the characteristic curve for the lateral stiffness is symmetric with respect to the origin.

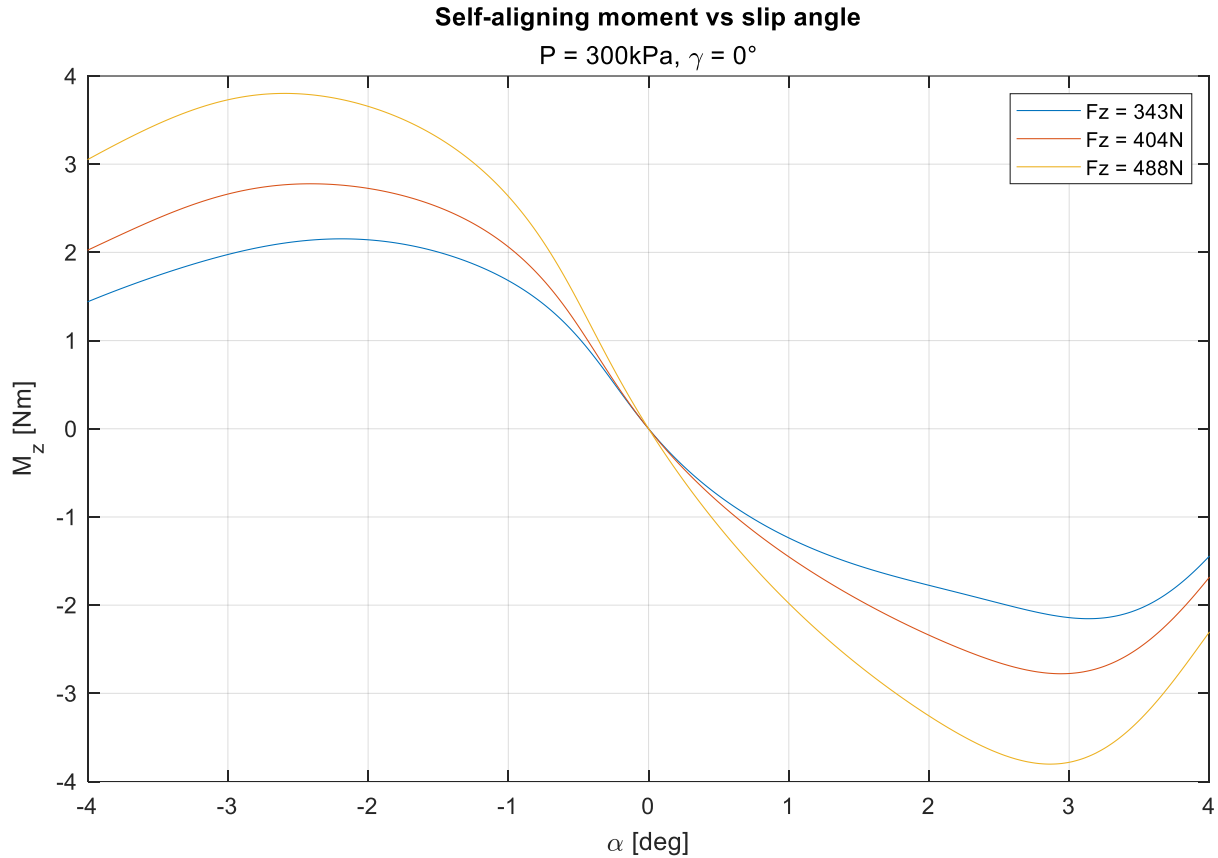


Figure 3.14: Self-aligning torque plot as a function of the side slip angle, for pressure equal to 300 kPa , camber 0° and varying vertical load ($343 \text{ N}, 404 \text{ N}, 488 \text{ N}$) for SCH-T03.

The peak values of the self-aligning torque and the relative values of side slip angle are collected in Table 3.8.

Inflation Pressure [kPa]	Vertical load [N]	Camber [$^\circ$]	$\alpha_{M_z,\text{max}} [^\circ]$	$M_z,\text{max} [\text{Nm}]$
300	343	0	3.1	-2.2
300	404	0	2.9	-2.8
300	488	0	2.8	-3.8
300	343	0	-2.2	2.2
300	404	0	-2.4	2.8
300	488	0	-2.6	3.8

Table 3.8: Peak self-aligning torque values and corresponding slip angles, constant pressure 300 kPa , constant camber 0° and varying vertical load ($343 \text{ N}, 404 \text{ N}, 488 \text{ N}$) for SCH-T03.

From Figure 3.14 it can be noted that the trend of the self-aligning curve is linear for low slip angle values, with growing non-linearity for increasing slip angles ($> |1.5^\circ|$). In fact, the curve seems to reach a peak, after which it decreases in values or stays almost constant. It can be observed that the effect of the increasing load on F_y is a rotation of the curve about the origin in the anticlockwise direction.

Looking at Table 3.8 it is possible to see that, for positive side slip angles, the increase of the vertical load causes the translation of the maximum value of the self-aligning torque to higher side slip angles and the increase of the self-aligning torque peak value in modulus.

As reported in literature, the self-aligning torque behaviour is closely related to the lateral force one and this justifies the reason why M_z increases its value in modulus with the vertical load, similarly to F_y . The difference in the shape of the characteristic curves is due to the non-linear pneumatic trail term.

3.2.2.2. Constant pressure and vertical load, camber variation

Through the performed tests, the characteristic curves at constant pressure, constant vertical load and different camber angle values could be compared.

In Figure 3.15 the lateral force F_y is represented as function of the lateral slip angle α for three values of camber angle. Vertical load and inflation pressure are constant ($F_z = 404 \text{ N}$, $P = 300 \text{ kPa}$).

The camber variation at constant inflation pressure and vertical load causes a vertical shift in the lateral force curve with respect to the camber 0° one, with the shift being directed downwards for negative camber angles and upwards for positive camber angles. This effect can also be noted by observing the F_y values in Table 3.9: it can be seen that the difference between the curves at camber -5° and 0° is almost the same whether it is evaluated at slip angles $+2^\circ$ or at -2° . This also applies to the curves at camber 5° and 0° .

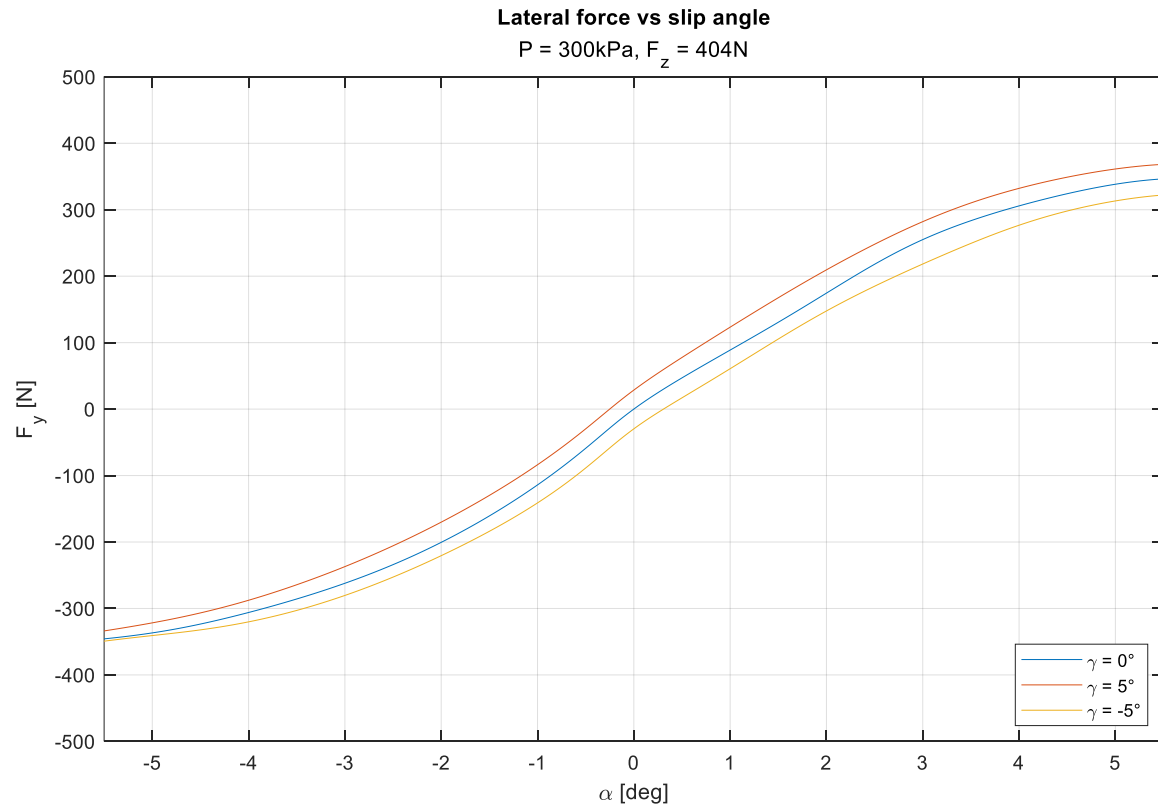


Figure 3.15: Lateral force plot as a function of the side slip angle, for pressure equal to 300 kPa , vertical load $F_z = 404\text{ N}$ and varying camber ($-5^\circ, 0^\circ, 5^\circ$) for SCH-T03.

Inflation Pressure [kPa]	Vertical load [N]	Camber [$^\circ$]	Side slip angle [$^\circ$]	F_y [N]
300	404	-5	2	147.7
300	404	0	2	174.5
300	404	5	2	209.5
300	404	-5	-2	-220.6
300	404	0	-2	-200.5
300	404	5	-2	-170.1

Table 3.9: Lateral force values at slip angle equal to 2° and -2° ; constant pressure 300 kPa , constant vertical force 404 N and varying camber ($-5^\circ, 0^\circ, 5^\circ$) for SCH-T03.

In Figure 3.16 the self-aligning torque M_z is represented as function of the lateral slip angle α for three values of camber angle. Vertical load and inflation pressure are constant ($F_z = 404\text{N}$, $P = 300\text{kPa}$).

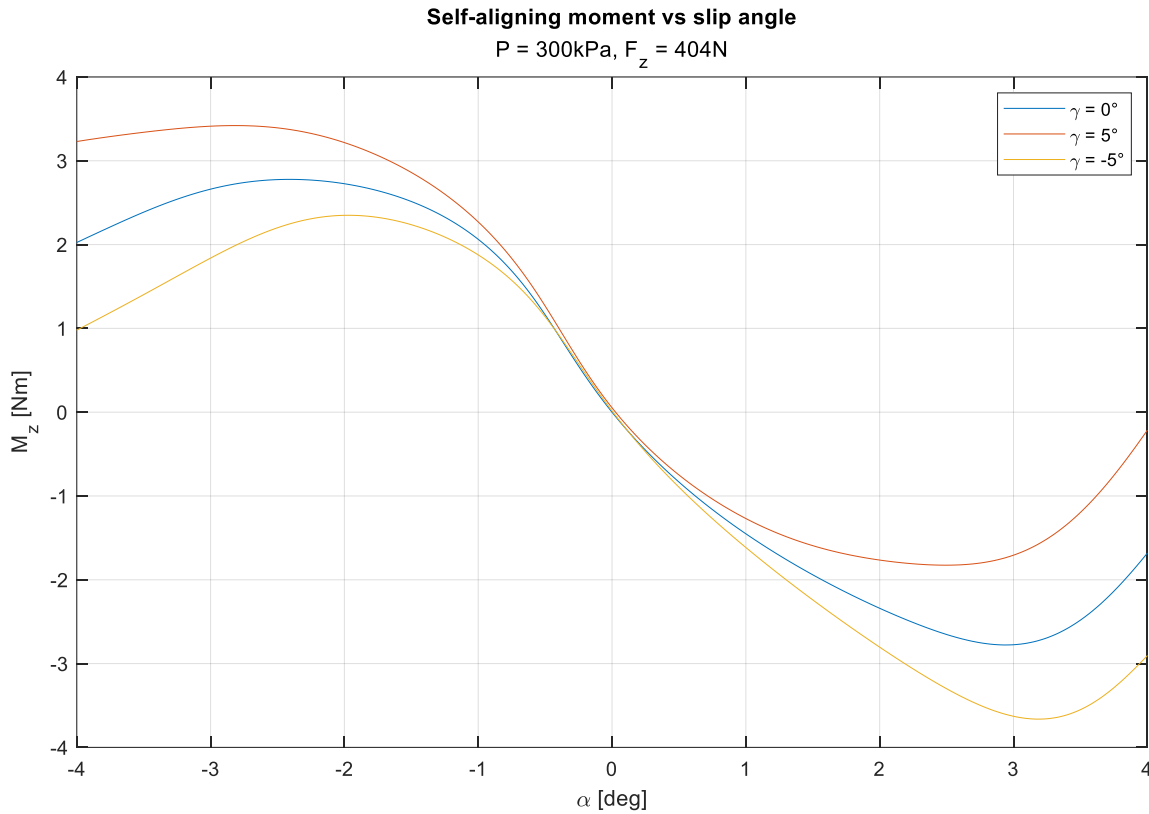


Figure 3.16: Self-aligning torque as a function of the side slip angle for pressure equal to 300kPa , vertical load $F_z = 404\text{N}$ and varying camber (-5° , 0° , 5°) for SCH-T01.

Inflation Pressure [kPa]	Vertical load [N]	Camber [$^\circ$]	$\alpha_{M_z \text{ max}} [^\circ]$	$M_{z \text{ max}} [\text{Nm}]$
300	404	-5	3.2	-3.7
300	404	0	3.0	-2.8
300	404	5	2.6	-1.8
300	404	-5	-2.0	2.4
300	404	0	-2.4	2.8
300	404	5	-2.8	3.4

Table 3.10: Peak self-aligning torque values and corresponding slip angles; constant pressure 300kPa , constant vertical load 404N and varying camber (-5° , 0° , 5°) for SCH-T03.

The vertical shift is directed downwards for negative camber angles and upwards for positive camber angles, which is a very similar behaviour to the one observed on the lateral force, however with much reduced impact at lower slip angles. This similarity is explained by the close relation between M_z and F_y known from literature, while the difference in the shape of the curves is due to the non-linear pneumatic trail term.

3.2.2.3. Cornering stiffness

The cornering stiffness was evaluated for each combination of pressure, camber angle and vertical load considered for the tyre SCH-T03.

In Table 3.11 are reported the cornering stiffness values found varying the vertical load and the pressure, with camber 0° , while Table 3.12 reports the values found varying the camber angle for different values of vertical load at 300 kPa . All the values of cornering stiffness presented in the next tables must take into account an uncertainty U of $\pm 1.5\%$ that includes measuring errors, approximations, track wear, tyre wear, and any other possible cause of uncertainty.

Cornering stiffness [$N/\text{°}$]							
		Vertical Load [N]					
		343		404		488	
		Value	%	Value	%	Value	%
Inflation Pressure [kPa]	300	105.2	-	113.6	8	123.5	17
	400	98.2	-	108.1	10	124.4	27
	500	86.6	-	90.1	4	111.6	7

Table 3.11: Cornering stiffness values constant camber equal to 0° , varying pressure (300 kPa , 400 kPa , 500 kPa) and vertical load (343 N , 404 N , 488 N) for SCH-T03. The '%' column indicates the percentage variation of the considered cornering stiffness value with respect to the one at lower vertical load.

Cornering stiffness [N/°]										
P = 300 kPa		Vertical Load [N]								
		343			404			488		
		Value	%	y0	Value	%	y0	Value	%	
Camber [°]	-5	107.9	2.5	-24.1	111.7	-1.6	-29.7	113.2	-8.3	-45.7
	0	105.2	-	-	113.6	-	-	123.5	-	-
	5	102.0	-3.1	21.8	112.5	-1.0	28.6	124.5	0.8	30.4

Table 3.12: Cornering stiffness values at constant pressure equal to 300 kPa, varying camber ($-5^\circ, 0^\circ, 5^\circ$) and vertical load (343 N, 404 N, 488 N) for SCH-T03. The '%' column indicates the percentage variation of the considered cornering stiffness value with respect to the one at same vertical load and camber 0° . The 'y0' column indicates the value that corresponds to the intersection of the curves with the F_y axis.

It can be noted that the cornering stiffness increases with the vertical load, at constant inflation pressure and camber angle. Instead, for constant vertical load and inflation pressure, the cornering stiffness value for different camber does not change much ($\pm 3\%$), with the case at vertical load 488 N and camber angle -5° considered as an outlier. This appears to be coherent with the fact that the camber influence on the lateral force versus slip angle characteristic only consists in a vertical translation of the characteristic curve.

3.3. Abnormal characteristic curves

The "Standard Dynamic Analysis" includes the fact that the dynamic test has to be repeated at least twice in the same conditions of inflation pressure, camber angle and vertical load, in order to validate the repeatability. However, some tests reported strange characteristic curve behaviours that were noticed only after the experimental campaign, when performing the analysis. This led to the necessity of repeating even entire tested combinations, to deep dive into the anomalies.

The tyres interested by this type of repeated analysis were:

- SCH-T03
- SCH-T04
- CST-T02
- SCA-T05

This section covers some examples of curves that reported unexpected trends, followed by the results of the repeated tests to observe how they compare with the previous ones. Then, the cause for the atypical behaviour was investigated.

3.3.1. SCH-T03 and SCH-T04

The SCH-T03 and the SCH-T04 tyres presented an atypical behaviour at the highest tested inflation pressure (500 kPa) and vertical load (488 N), for all three of the tested camber values ($-5^\circ, 0^\circ, 5^\circ$).

Figure 3.17 reports the characteristic curves resulting from the SCH-T03 first tests for lateral force and self-aligning torque respectively, for the stated testing conditions. Figure 3.18, instead, reports the lateral force and self-aligning torque curves for the SCH-T04 first tests.

Looking at both the Figures it can be immediately pointed out that the curves assume a wavy trend for lower slip angles. This effect is mostly noticeable in the lateral force curves at camber different from 0° , which makes the vertical shift with respect to the camber 0° curve, caused by the camber variation, not constant along the whole span of tested slip angles.

Moreover, the self-aligning torque characteristic curves do not resemble the typical result for a camber variation analysis obtained through the "Standard Dynamic Analysis": the shift between the 5° and 0° curves is much larger than the one between the 0° and the -5° . The three of them also present a sort of perturbation in correspondence of slip angle equal to -1° , which is more pronounced in the cambered curves.

It was decided to repeat the tests to understand whether the anomaly could be caused by circumstantial factors or it was a systematic limit behaviour of the tyre, since it only appeared in the most critical condition (max inflation pressure, max vertical load).

The tests were then repeated only for the parameter combinations that presented the atypical behaviours, therefore only for pressure 500 kPa , vertical load 488 N and all camber values ($-5^\circ, 0^\circ, 5^\circ$). The lateral force and self-aligning torque curves are reported in Figure 3.19 for SCH-T03 and Figure 3.20 for SCH-T04. From these plots it can be noted that the curves from the repeated tests were aligned with the known trends from literature and with the behaviour of the observed curves of the "Standard Dynamic Analysis" of those tyres.

The hypothesis of the limit condition of the tyre could then be excluded, however, it was necessary to understand what could have been the cause of such a different behaviour.

The main difference between the first tests and the repeated tests is in the flat track belt. It was changed since it had endured a complete year of testing.

Another important factor is the presence of sand: in fact, during the first test, a layer of sand (of known granulometry) was glued to the track in order to simulate in a more accurate way the road surface roughness and irregularities. This layer of sand would be consumed by the repeated tests, sometimes leaving empty spots or uncovering the layer of glue. This makes the surface extremely irregular from the friction coefficient point of view, in fact, the tyre will be in contact with three different materials, which are the sand, the glue and the flat track belt.

This could be a sensible explanation for the atypical behaviour observed in the first curves, and the fact that it only interests the maximum load and maximum pressure curves may be due to the fact that, being it the most critical condition, it can be also sensitive to these kinds of fluctuations and irregularities.

Once the flat track was replaced, it was decided not to apply the layer of sand anymore, so that the uniformity of the simulated road surface would be guaranteed, thus allowing a more regular trend for the lateral force and the self-aligning torque.

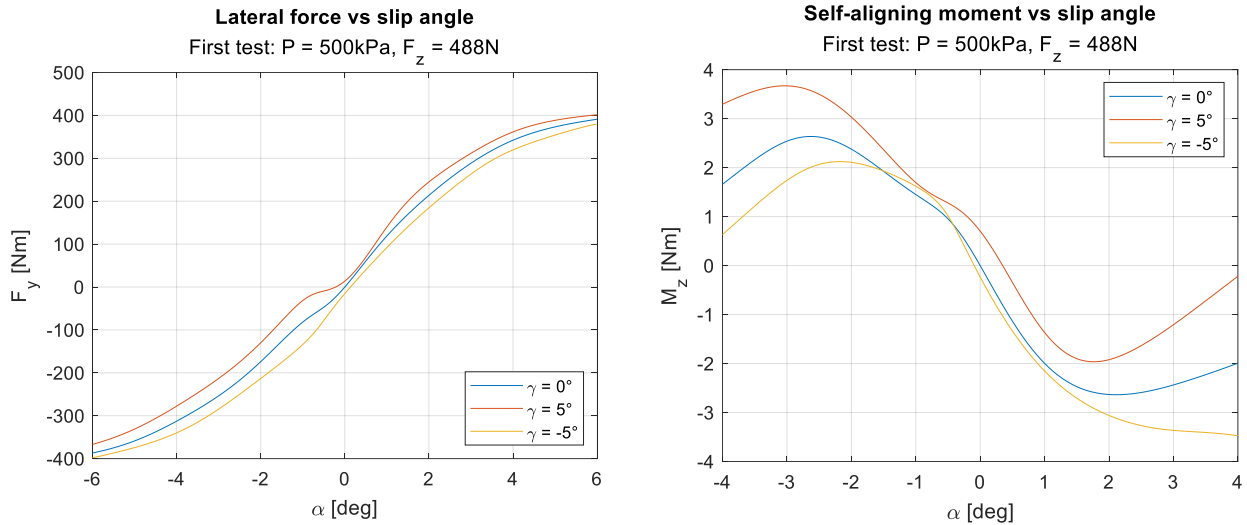


Figure 3.17: Lateral force (left) and self-aligning torque (right) plot as a function of the side slip angle, for pressure equal to 500 kPa, vertical load $F_z = 488\text{ N}$ and varying camber (-5° , 0° , 5°) for the first SCH-T03 test.

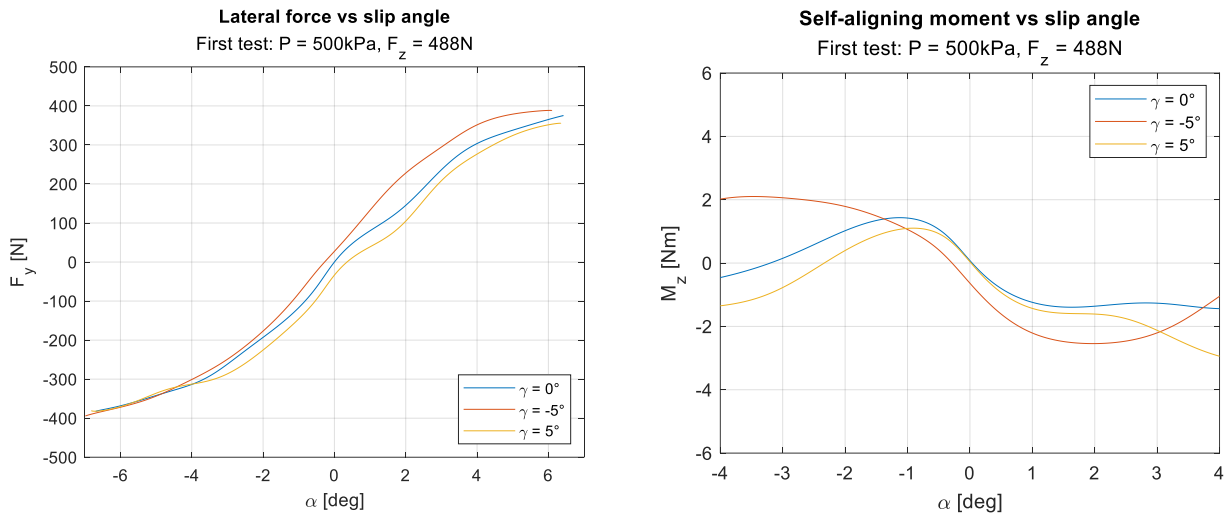


Figure 3.18: Lateral force (left) and self-aligning torque (right) plot as a function of the side slip angle, for pressure equal to 500 kPa, vertical load $F_z = 488\text{ N}$ and varying camber (-5° , 0° , 5°) for the first SCH-T04 test.

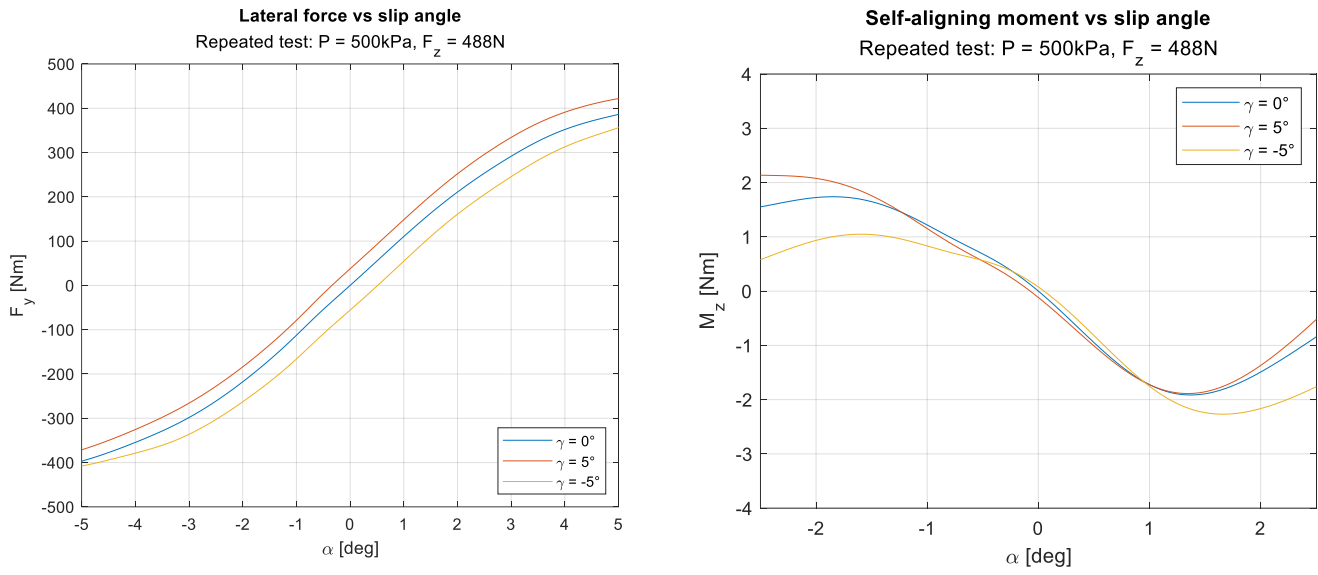


Figure 3.19: Lateral force (left) and self-aligning torque (right) plot as a function of the side slip angle, for pressure equal to 500 kPa , vertical load $F_z = 488 \text{ N}$ and varying camber (-5° , 0° , 5°) for the repeated SCH-T03 test.

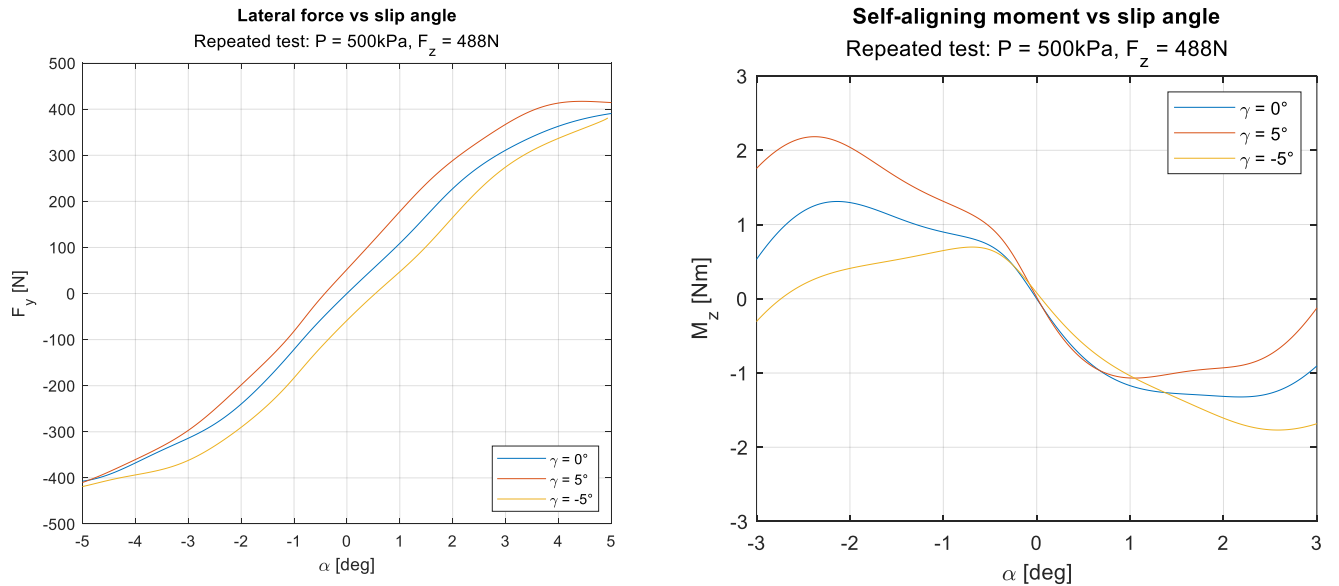


Figure 3.20: Lateral force (left) and self-aligning torque (right) plot as a function of the side slip angle, for pressure equal to 500 kPa , vertical load $F_z = 488 \text{ N}$ and varying camber (-5° , 0° , 5°) for the repeated SCH-T04 test.

3.3.2. CST-T02

The CST-T02 tyre as well presented atypical characteristic curves once the dynamic test data were analysed. Differently from the SCH-T03 and SCH-T04, the curves that were interested by these trends were not relative to a specific parameter combination, but they were scattered amongst all of the testing conditions without any evident common theme.

For the sake of simplicity, Figure 3.22 reports an example of lateral force and self-aligning torque versus slip angle curves at inflation pressure 400 kPa , camber 0° and vertical loads 411 N , 449 N , 526 N , obtained during the first test session of CST-T02 tyre.

It can be seen that, for the lateral force curve, the load variation effect does not present the typical behaviour known from literature. The three curves do not intersect in the origin and each one presents a strong asymmetry with respect to the origin. Similar observations can be drawn by looking at the self-aligning torque curves reported in Figure 3.22 (right), which are not only asymmetrical with respect to the origin, but also seem to have undergone a horizontal translation, when increasing the vertical load.

Since the atypical behaviour wasn't localized on a specific set of curves, the entire test session for the CST-T02 tyre was repeated. Figure 3.23 shows the lateral force and self-aligning torque curves obtained for the repeated test session at the same conditions of the curves in Figure 3.22 (pressure 400 kPa , camber 0° , loads 411 N , 449 N , 526 N). The repeated tests provided results that are much more aligned with what was expected from literature for both types of characteristic curve.

Therefore, it is important to understand what could have caused such different results between the two test campaigns. As for the SCH-T03 and SCH-T04, the first test session was performed on the worn flat track belt, while the second session used the new flat track belt.

Another possible cause of the discrepancy between the results could be that the CST-T02 tyre, presented a manufacturing defect on its tread. In some zones of the tyre, the centre of the tread presented a step along the circumferential direction, as it can be seen in Figure 3.21. It is possible that, for the repeated test, the step could have been, at least partially, worn out, hence removing another possible source of asymmetry and irregularity in the rolling motion.



Figure 3.21: Contact patch of the CST-T02 tyre, in the zone affected by the manufacturing defect.

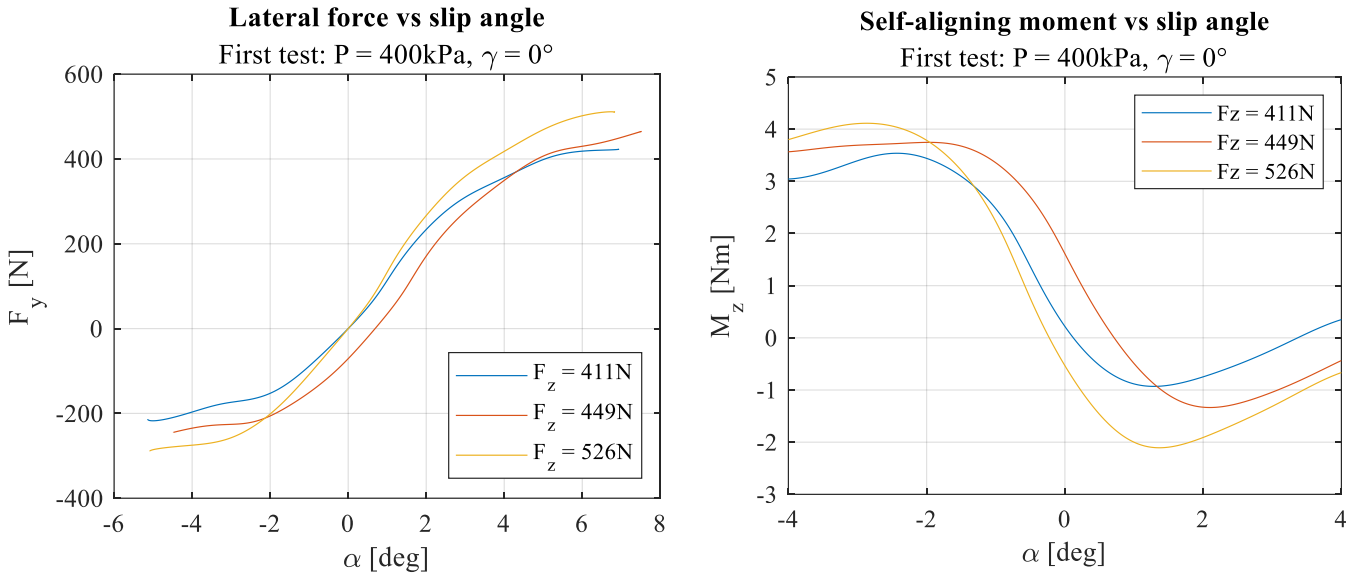


Figure 3.22: Lateral force (left) and self-aligning torque (right) plot as a function of the side slip angle, for pressure equal to 400 kPa , camber 0° and varying vertical load (411 N , 449 N , 526 N) for the first CST-T02 test.

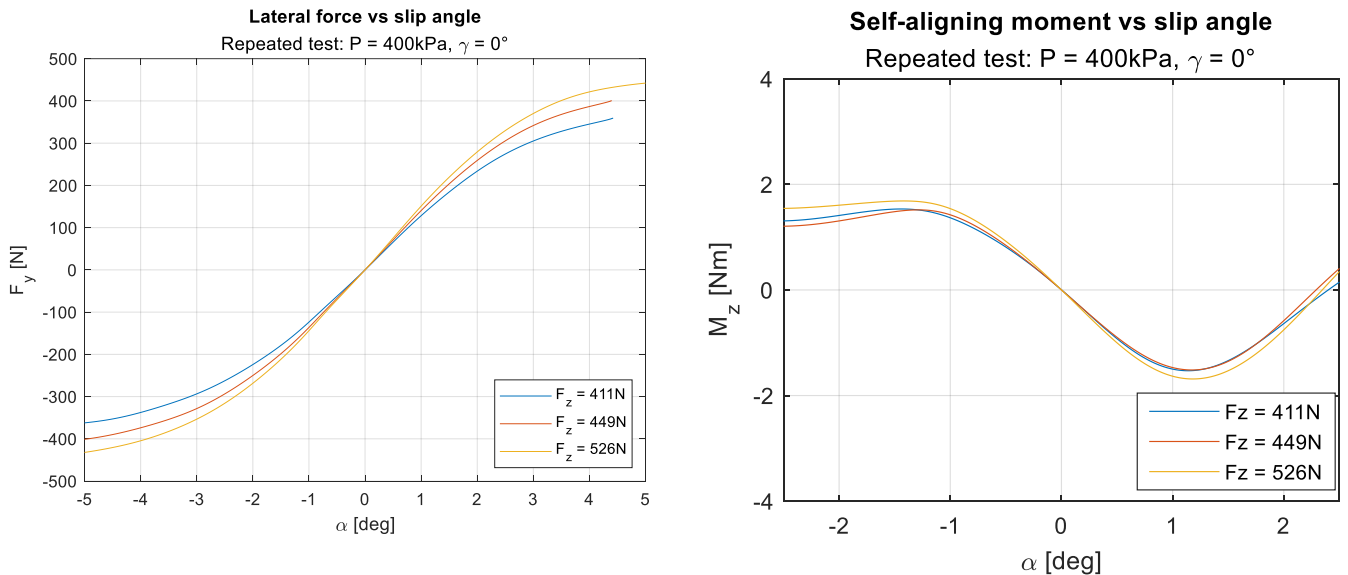


Figure 3.23: Lateral force (left) and self-aligning torque (right) plot as a function of the side slip angle, for pressure equal to 400 kPa , camber 0° and varying vertical load (411 N , 449 N , 526 N) for the repeated CST-T02 test.

3.3.3. SCA-T05

SCA-T05's case is different from the ones that have been described until now, because it did not present a strange behaviour in the processed characteristic curves, but it actually behaved strangely during the test itself. In fact, during the dynamic tests for camber angle different from 0° , when approaching the maximum slip angle on the side whom the tyre was cambered towards, it suddenly increased the vibrations and started wobbling, transmitting the vibrating motion also to the VeTyT structure. The behaviour would then come back to normal once the tyre steered away from the maximum slip angle.

First, it was thought to be a setup problem, but this hypothesis was soon excluded after a thorough check of the Vetyt setup status. To avoid damages to the VeTyT structure, it was decided to just perform the camber 0° curves, for all pressure and vertical load combinations. The slip angle span used for this time of test was $[-6^\circ, 6^\circ]$. Therefore, no data was acquired for curves at camber 5° and -5° during the original test session.

It was later decided to test the cambered curves, spanning a shorter interval of slip angles (about $[-4^\circ, 4^\circ]$) to avoid the high vibrations that appeared in the original tests when getting closer to slip angle $\pm 6^\circ$. This can be seen from Figure 3.24 where the lateral force and self-aligning torque for the SCA-T05 tyre are reported, for the testing condition of 300 kPa , 404 N and all camber values $(-5^\circ, 0^\circ, 5^\circ)$.

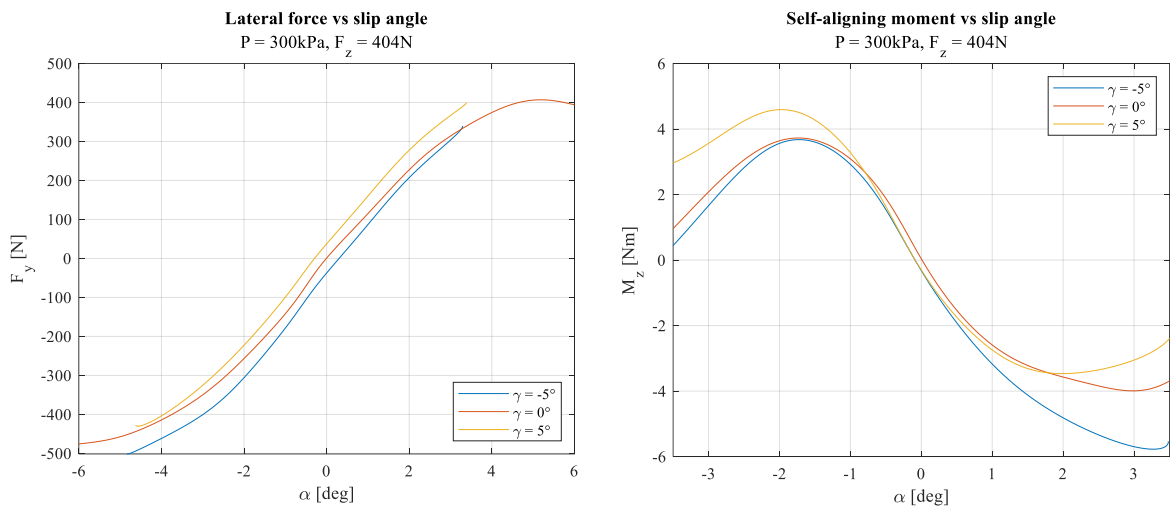


Figure 3.24: Lateral force (left) and self-aligning torque (right) plot as a function of the side slip angle, for pressure equal to 300 kPa , vertical load $F_z = 404 \text{ N}$ and varying camber $(-5^\circ, 0^\circ, 5^\circ)$ for the SCA-T05 tyre.

3.4. Comparison between tyre characteristic curves

The testing campaign that is the object of this thesis project examined several bicycle tyres, each with their unique characteristics. By looking at the tested tyres from the perspective of their functionality, it is evident that they can be sorted into three groups:

- *Cargo bike tyres*: tyres specifically designed to be mounted on two/three wheeled cargo bikes. Their main function is to carry goods together with the rider, therefore the payload can reach very high values. Among the tested tyres, the ones belonging to this category are:
 - SCH-T01
 - CST-T02
- *E-bike tyres*: tyres designed to be mounted on e-bikes, whose main function is the leisure activity or commuting. These bikes typically ride on city roads, for short-medium distances at consistent speeds. The tyres belonging to this category are:
 - SCH-T03
 - SCH-T04
 - SCA-T05
- *Road racing tyres*: tyres designed to be mounted on road bikes – or road racing bikes -, whose main function is the sports use on road, covering large distances at high speeds. Among the tested tyres, the ones belonging to this category are:
 - VIT-T10
 - VIT-T11

It can be of research interest to compare the characteristic curves, obtained through the “Standard Dynamic Analysis” (Section 3.2), from different tyres to see how the design and manufacturing choices of a certain type of tyre actually reflect on their behaviour and performance.

Section 3.4.1 will cover the comparison of tyres belonging to the same functionality group, whilst Section 3.4.2 will show a qualitative comparison between the three categories, performed by choosing a reference tyre for each one of the sets.

3.4.1. Comparison between tyres belonging to the same function group

In this Section, the results of a comparative analysis between the characteristic curves of tested tyres belonging to the same category is presented. The comparison will

examine curves obtained under specific testing conditions of camber angle, inflation pressure and vertical load that will be considered as representative of the trend of lateral force and self-aligning torque.

3.4.1.1. Cargo bike tyres

Cargo bike tyres are characterised by a small radius and a large section profile, when compared to the average city bike tyre. The two tyres that belong to this group are the SCH-T01 and the CST-T02, whose specifics are summarized in Table 3.13. They can endure vertical loads up to 95 kg (ca. 932 N) at relatively low inflation pressures: in fact, the maximum inflation pressure for the SCH-T01 is 400 kPa [27], while it is 450 kPa (65 psi) for the CST-T02 [28].

Brand	Serie	Name	Dimensions	ETRTO	Tyre code
Schwalbe	Balloon	Big Ben Plus	$20'' \times 2.15$	55 - 406	SCH-T01
CST	Brooklyn	/	$20'' \times 2.15$	55 - 406	CST-T02

Table 3.13: Analysed cargo bike tyres, with complete name, dimensions and internal tyre code.

The two tyres were mounted on the same rim (*Mach1 Kargo Disc 20'' (406 – 25c)* rim) and tested under the same values of pressure (400 kPa), vertical load (411 N , 526 N) and camber (-5° , 0° , 5°). For the sake of simplicity, the comparison was made on only one of those settings, that is taken as reference for the behaviour of the two tyres: inflation pressure equal to 400 kPa , vertical load equal to 411 N and camber 0° , as summarized in Table 3.14.

Figure 3.25 and Figure 3.26 show the plots of, respectively, the lateral force and the self-aligning torque for both tyres under the same testing conditions. Table 3.15 reports the lateral force values of both characteristic curves at slip angle equal to $\pm 2^\circ$ and $\pm 4^\circ$ and their cornering stiffnesses, while Table 3.16 reports the peak values of self-aligning torque with their relative slip angles.

Tyre code	Inflation pressure [kPa]	Vertical load [N]	Camber [$^\circ$]
SCH-T01	400	411	0
CST-T02	400	411	0

Table 3.14: Testing conditions chosen for the analysis of the considered tyres.

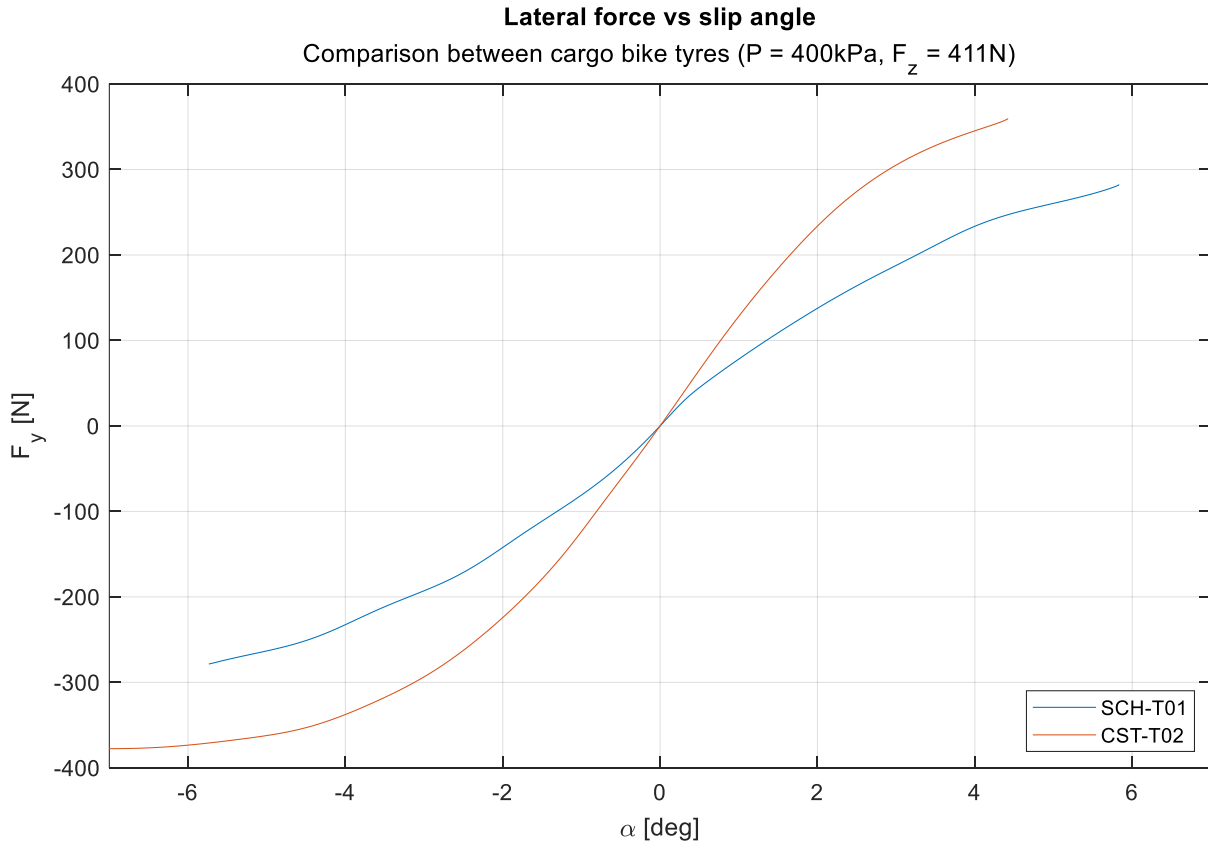


Figure 3.25: Lateral force plot as a function of the side slip angle, for pressure equal to 400 kPa , camber 0° and vertical load equal to 411 N for the analysed cargo bike tyres.

Tire code	Side slip angle $[\circ]$	F_y [N]	Side slip angle $[\circ]$	F_y [N]	Cornering Stiffness $[\text{N}/^\circ]$
SCH-T01	4	231.0	-4	-230.5	85.1
	2	137.7	-2	-142.2	
CST-T02	4	345.2	-4	-337.6	124.0
	2	233.7	-2	-224.1	

Table 3.15: Lateral force values at slip angle equal to $\pm 2^\circ$ and $\pm 4^\circ$ and cornering stiffness values for the analysed cargo bike tyres.

The two tyres present a very different lateral force behaviour, as can be observed from Figure 3.25. In fact, the CST-T02's cornering stiffness is 46% higher than the SCH-T01's, and therefore reaches higher lateral force values than the SCH-T01 at the same slip angles. However, it also seems to reach the non-linear behavior for lower slip angle

values (around $\pm 2^\circ$) whilst SCH-T01 seems to remain in the linear part of the characteristic curve for the whole span of tested slip angles.

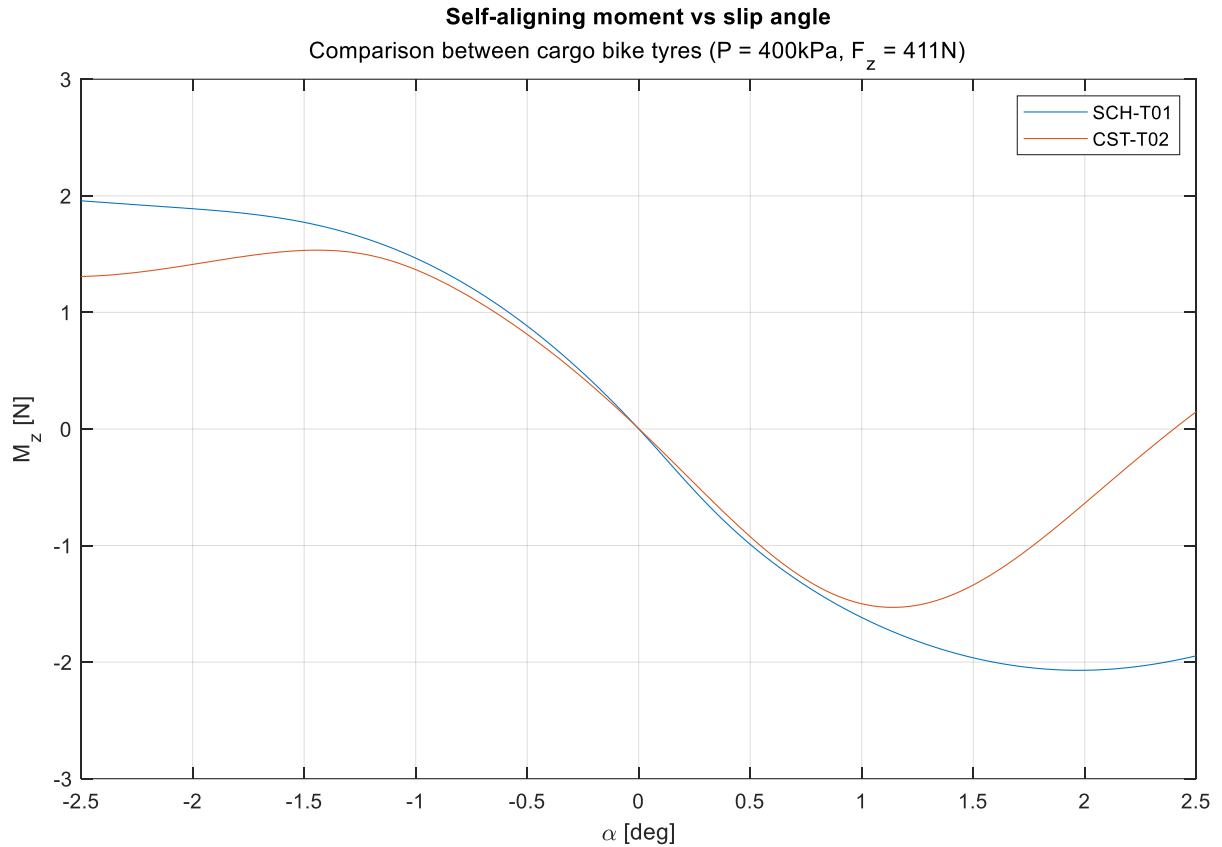


Figure 3.26: Self-aligning torque plot as a function of the side slip angle, for pressure equal to 400 kPa, camber 0° and vertical load equal to 411 N for the analysed cargo bike tyres.

Tire code	$\alpha_{M_z \text{ max}}$ [°]	$M_z \text{ max}$ [Nm]	$\alpha_{M_z \text{ max}}$ [°]	$M_z \text{ max}$ [Nm]
T01	2.0	-2.1	-2.5	2.0
T02	1.1	-1.5	-1.4	1.5

Table 3.16: Peak self-aligning torque values and relative slip angle values for the analysed cargo bike tyres.

For what concerns the self-aligning torque, the curves have an almost overlapping trend until $\pm 1^\circ$, after which each tyre assumes a different behaviour. The CST-T02 reaches its peak values in an almost symmetric way and then decreases with a non-linear behavior that is asymmetric with respect to the origin. SCH-T01 instead

continues to grow and reaches its peak at later values of slip angle, with a slighter asymmetry with respect to the origin. The behaviour at higher slip angles is highly non-linear, especially for CST-T02 that also presents different trends for positive and negative slip angles: this could be due to a manufacturing defect present in the tread of this tyre, seen in Section 3.3.2 (Figure 3.21), whose effect could have been amplified at higher slip angles.

3.4.1.2. E-bike tyres

E-bike tyres are characterised by a highly engraved tread, which creates canals that allow the water present on the road surface to easily flow away from the contact patch. The three tyres that belong to this group are the SCH-T03, the SCH-T04 and the SCA-T05, whose specifics are summarized in Table 3.17. They can carry up to 109 kg (ca. 1069 N) and they can be inflated at any pressure in the range 300 – 500 kPa [30]. It is important to keep in mind that the SCH-T03 is an evolution of the SCH-T04, with an improved compound that should allow more grip.

Brand	Serie	Name	Dimensions	ETRTO	Tyre code
Schwalbe	50km Energizer	Plus G-Guard 5/Addix-E	28" x 1.75	47 – 622	SCH-T03
Schwalbe	50km Energizer	Active Plus P-Guard 5	28" x 1.75	47 – 622	SCH-T04
Scalato	/	Mondano	28" x 2.15	55 – 622	SCA-T05

Table 3.17: Analysed e-bike tyres, with complete name, dimensions and internal tyre code.

The two tyres were mounted on the same rim (*Shimano Deore HB-M525A 28"* (622)) and tested under the same values of pressure (300 kPa, 400 kPa, 500 kPa), vertical load (343 N, 404 N, 488 N) and camber (-5°, 0°, 5°). For the sake of simplicity, the comparison was made on only one of those settings, that is taken as reference for the behaviour of the two tyres. The chosen combination is inflation pressure equal to 300 kPa, vertical load equal to 343 N and camber 0°, as summarized in Table 3.18.

Figure 3.27 and Figure 3.28 show the plots of, respectively, the lateral force and the self-aligning torque for both tyres under the same testing conditions. Table 3.19 reports the lateral force values of both characteristic curves at slip angle equal to ± 2° and ± 4°

and their cornering stiffnesses, while Table 3.20 reports the peak values of self-aligning torque with their relative slip angles.

Tyre code	Inflation pressure [kPa]	Vertical load [N]	Camber [°]
SCH-T03	300	343	0
SCH-T04	300	343	0
SCA-T05	300	343	0

Table 3.18: Testing conditions chosen for the analysis of the considered tyres.

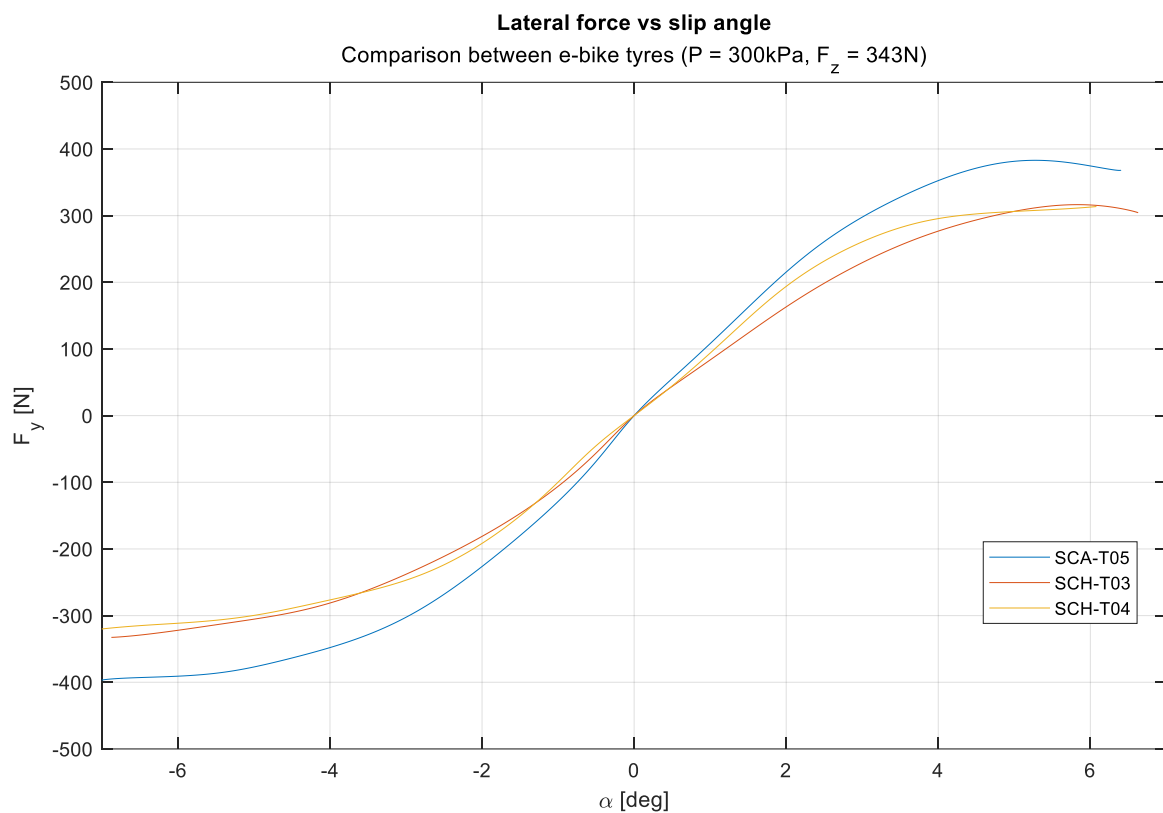


Figure 3.27: Lateral force plot as a function of the side slip angle, for pressure equal to 300 kPa , camber 0° and vertical load equal to 343 N for the analysed e-bike tyres.

Tire code	Side slip angle [°]	F_y [N]	Side slip angle [°]	F_y [N]	Cornering Stiffness [N/°]
SCH-T03	4	276.8	-4	-281.1	105.2
	2	163.1	-2	-181.1	
SCH-T04	4	295.5	-4	-276.5	100.1
	2	193.8	-2	-191.7	
SCA-T05	4	352.5	-4	-347.9	132.0
	2	215.4	-2	-226.3	

Table 3.19: Lateral force values at slip angle equal to $\pm 2^\circ$ and $\pm 4^\circ$ and cornering stiffness values for the analysed e-bike tyres.

From Figure 3.27 it can be seen that the lateral force follows a very similar trend for all three of the curves, however with some slight differences. The two Schwalbe tyres present almost overlapping curves. Looking at Table 3.19 it is possible to appreciate the relevant difference between the two, which lies in the cornering stiffness, that is 5 N/° higher for SCH-T04. SCH-T05 reaches higher values of lateral forces overall, and consequently also has the highest cornering stiffness value, 32% higher than the SCH-T04's.

Regarding the self-aligning torque, the behaviour of the three tyres is quite different. In particular, the SCH-T05 tyre increases rapidly in module for low slip angles with higher values compared to the Schwalbe tyres, which is coherent with the fact that it also has the highest lateral force values of the three tyres. It reaches the peak value of 3.0 Nm and then quickly decrease. The total behaviour is asymmetric with respect to the origin. Both Schwalbe tyres, instead, increase at a lower rate for low slip angles, with SCH-T03 having generally slightly higher values than SCH-T04. They reach the

peak self-aligning torque of $\pm 2.2 \text{ Nm}$ for SCH-T03 and $\pm 1.8 \text{ Nm}$ for SCH-T04, with a 0.4 Nm gap between the two peak values.

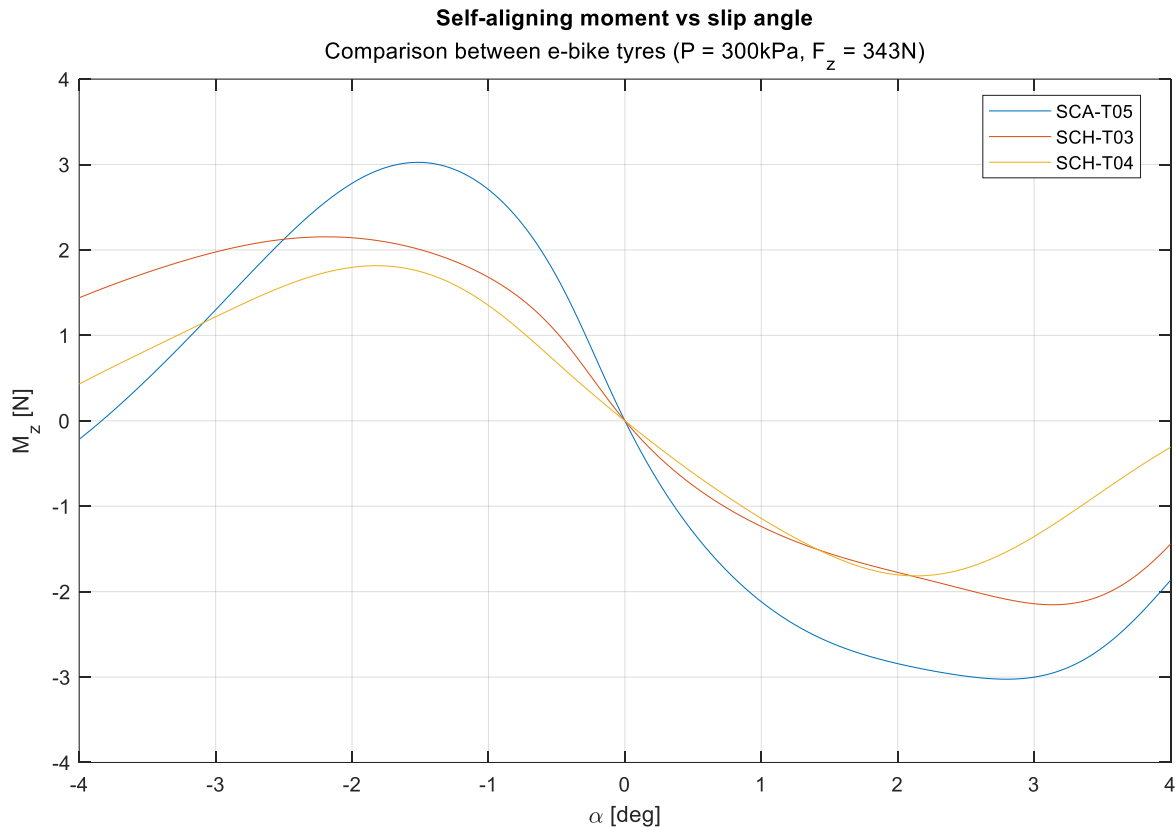


Figure 3.28: Self-aligning torque plot as a function of the side slip angle, for pressure equal to 300 kPa , camber 0° and vertical load equal to 343 N for the analysed e-bike tyres.

Tire code	$\alpha_{M_z \text{ max}} [\text{°}]$	$M_z \text{ max} [\text{Nm}]$	$\alpha_{M_z \text{ max}} [\text{°}]$	$M_z \text{ max} [\text{Nm}]$
SCH-T03	3.1	-2.2	-2.2	2.2
SCH-T04	2.1	-1.8	-1.8	1.8
SCA-T05	2.8	-3.0	-1.5	3.0

Table 3.20: Peak self-aligning torque values and relative slip angle values for the analysed e-bike tyres.

3.4.1.3. Road racing bike tyres

Road bike tyres are characterised by a very narrow profile section with grooves only in the circumferential direction. The two tyres that belong to this group are the VIT-T10 and the VIT-T11, whose specifics are summarized in Table 3.21. They can be inflated at a wide range of pressures, that go from 300 kPa up to 800 kPa. These two tyres share the same compound, and the only difference between them is the profile width, that is 2 mm wider for the VIT-T11.

Brand	Serie	Name	Dimensions	ETRTO	Tyre code
Vittoria	Road Racing / Competition	Corsa N.ext	28" x 26	26 – 622	VIT-T10
Vittoria	Road Racing / Competition	Corsa N.ext	28" x 26	28 – 622	VIT-T11

Table 3.21: Analysed cargo bike tyres, with complete name, dimensions and internal tyre code.

The two tyres were mounted on the same rim (rigid rim) and tested under the same values of pressure (350 kPa, 550 kPa, 750 kPa), vertical load (340 N, 400 N, 490 N) and camber (0°). For the sake of simplicity, the comparison was made on only one of those settings, that is taken as reference for the behaviour of the two tyres. The chosen combination is inflation pressure equal to 350 kPa, vertical load equal to 340 N and camber 0°, as summarized in Table 3.21.

Figure 3.29 and Figure 3.30 show the plots of, respectively, the lateral force and the self-aligning torque for both tyres under the same testing conditions. Table 3.23 reports the lateral force values of both characteristic curves at slip angle equal to $\pm 2^\circ$ and $\pm 4^\circ$ and their cornering stiffnesses, while Table 3.24 reports the peak values of self-aligning torque with their relative slip angles.

Tyre code	Inflation pressure [kPa]	Vertical load [N]	Camber [°]
VIT-T10	350	340	0
VIT-T11	350	340	0

Table 3.22: Testing conditions chosen for the analysis and cornering stiffness values of the considered tyres.

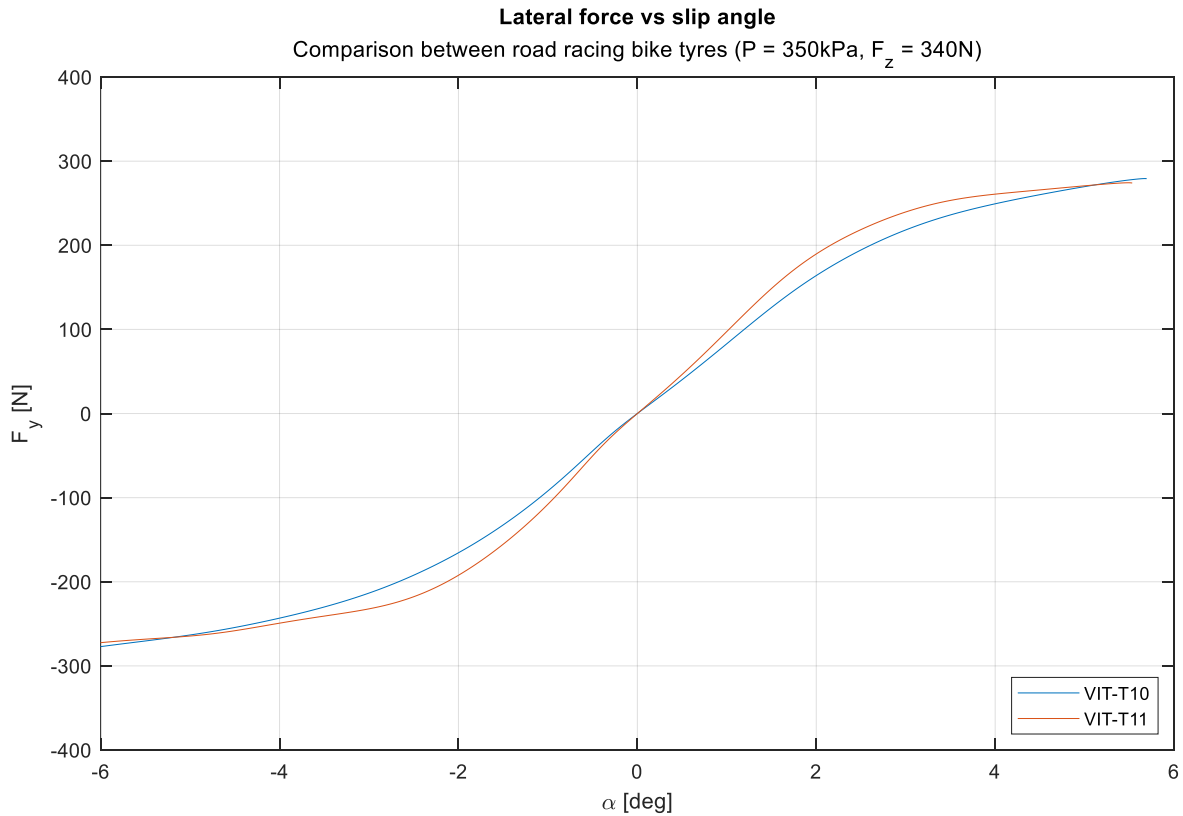


Figure 3.29: Lateral force plot as a function of the side slip angle, for pressure equal to 350 kPa , camber 0° and vertical load equal to 340 N for the analysed road racing bike tyres.

Tire code	Side slip angle $[\circ]$	F_y [N]	Side slip angle $[\circ]$	F_y [N]	Cornering Stiffness $[N/\circ]$
VIT-T10	4	249.4	-4	-243.2	89.14
	2	164.1	-2	-165.6	
VIT-T11	4	260.8	-4	-249.2	103.98
	2	189.7	-2	-192.3	

Table 3.23: Lateral force values at slip angle equal to $\pm 2^\circ$ and $\pm 4^\circ$ and cornering stiffness values for the analysed e-bike tyres.

Figure 3.29 and Table 3.23 clearly show how similar the two road racing tyres are: they follow a very similar trend and have overall similar values, with an almost perfect

symmetry with respect to the origin. However, it can be noticed that VIT-T11 grows faster for low slip angles, in the linear part of the characteristic curve, and this is also observed from the cornering stiffness values reported in Table 3.29, which is 14.4% higher than the VIT-T10's. This causes the difference between the two curves for low slip angles. This gap tends to increase, reaching its maximum at the transition point between the linear and the non-linear part. Then the two tyres enter the non-linear part of the curve, where they assume very similar values.

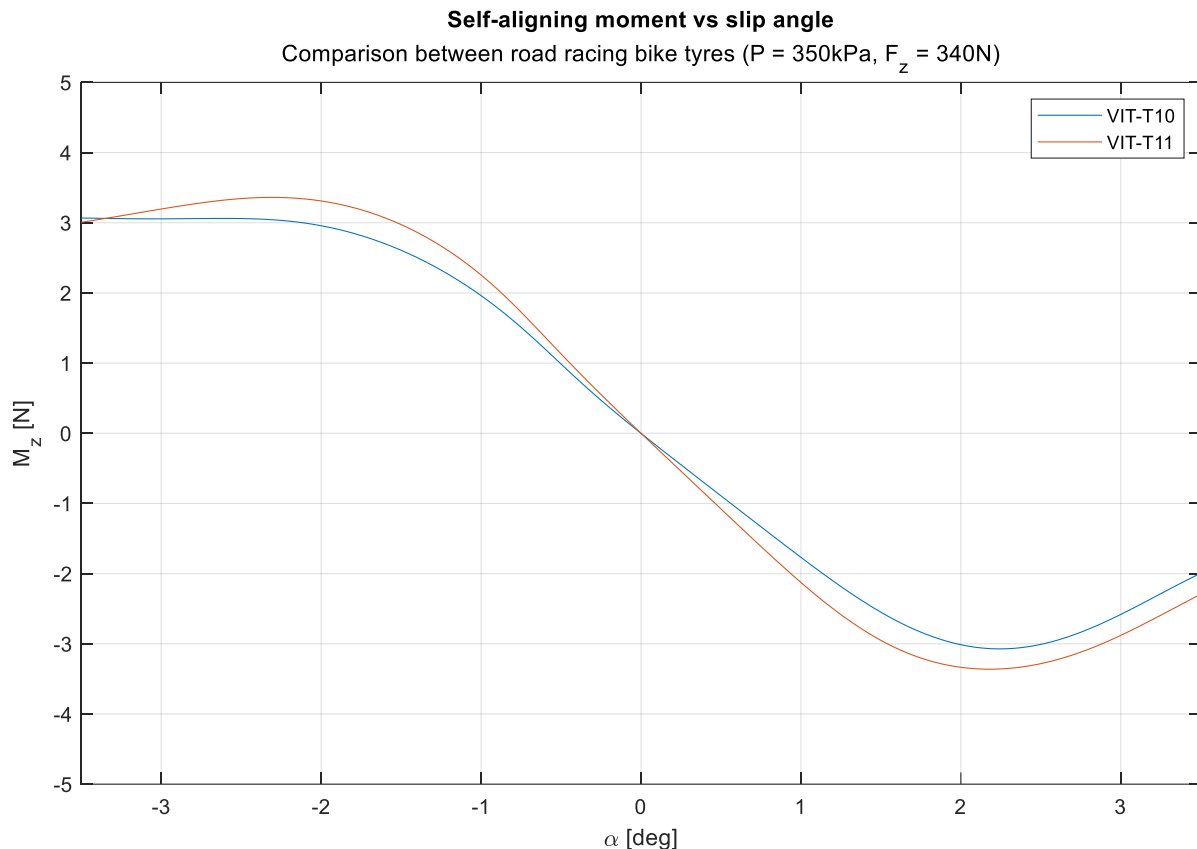


Figure 3.30: Self-aligning torque plot as a function of the side slip angle, for pressure equal to 350 kPa, camber 0° and vertical load equal to 340 N for the analysed road racing bike tyres.

Tire code	$\alpha_{M_z \text{ max}} [\text{°}]$	$M_z \text{ max} [\text{Nm}]$	$\alpha_{M_z \text{ max}} [\text{°}]$	$M_z \text{ max} [\text{Nm}]$
VIT-T10	2.25	-3.07	-2.25	3.03
VIT-T11	2.18	-3.36	-2.18	3.35

Table 3.24: Peak self-aligning torque values and relative slip angle values for the analysed road racing bike tyres.

The closeness of the two tyres' behaviour observed for the lateral force can also be appreciated for the self-aligning torque, in Figure 3.30 and Table 3.24. The difference in cornering stiffness, and therefore in the lateral force behaviour at low slip angles, causes the VIT-T11 to grow at a higher rate than the VIT-T10 and to reach higher values overall. As a consequence, VIT-T11 reaches its peak values at $\pm 2.18^\circ$, only slightly before VIT-T10 that reaches them at $\pm 2.25^\circ$. The gap between the peak values of the two curves is around 0.30 Nm and, after that, the two tyres enter the non-linear part of the curve, where they decrease in value with an almost identical trend. However, it can be seen that at high slip angles the M_z trends are not symmetric with respect to the origin: this could be due to a possible uneven wear of the flat track belt, that would amplify its effect thanks to the non-linearity.

The similarity between the two Vittoria tyres was expected due to the fact that they share the same internal structure and compound, however from this analysis the difference caused by the $2mm$ -increase in profile width can be appreciated, with the wider tyre being the one that reaches the highest values.

3.4.2. Qualitative comparison between tyre functional groups

It can be interesting to compare the characteristic curves of the three kinds of bicycle tyre from a qualitative point of view, in order to appreciate how the difference in function translates to the lateral force and self-aligning torque behaviour.

One curve for each class was chosen, however, in order for the curves to be comparable to a reasonable extent, the most similar testing conditions were chosen and are reported in Table 3.25. The vertical load between the three tyres has a maximum difference of 11 N (between SCH-T01 and VIT- T11), while the VIT-T11's inflation pressure differs of 50 kPa from the two considered Schwalbe tyres. It must also be taken into account that the cargo bike tyre and e-bike tyre were mounted on a deformable rim, while the road racing bike tyre was mounted on a rigid rim.

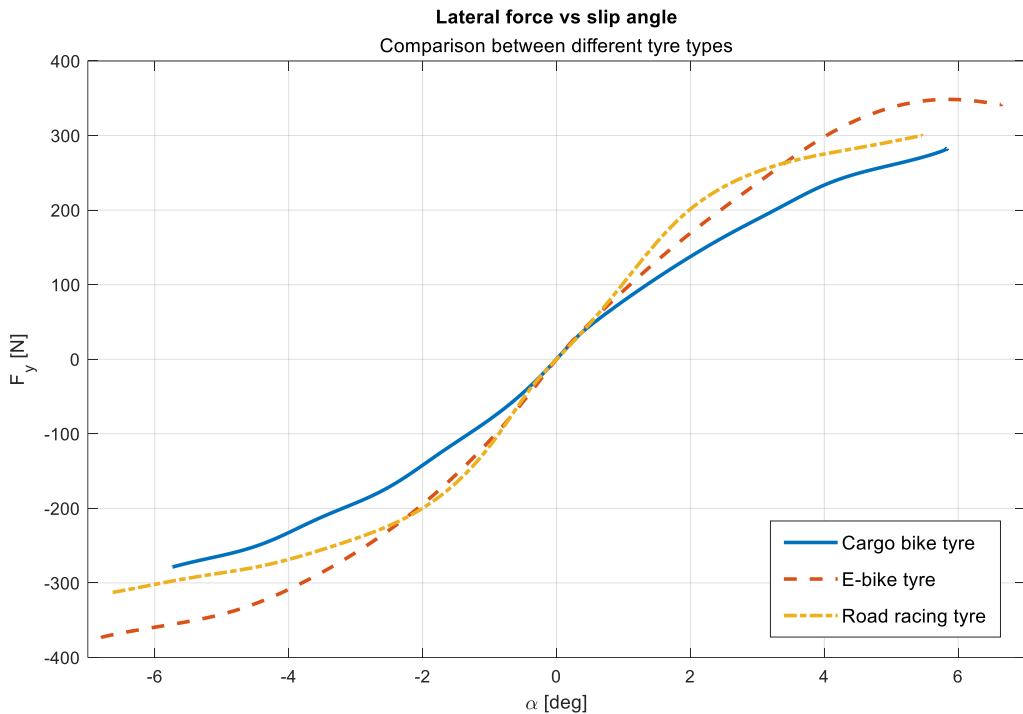


Figure 3.31: Lateral force plot as a function of the side slip angle for the analysed tyre categories under the testing conditions specified in Table 3.25.

Tyre type	Tyre code	Inflation pressure [kPa]	Vertical load [N]	Camber [°]	Cornering Stiffness [N/°]
Cargo bike	SCH-T01	400	411	0	85.1
E-bike	SCH-T03	400	404	0	108.1
Road racing bike	VIT-T11	350	400	0	111.4

Table 3.25: Testing conditions chosen for the analysis and cornering stiffness values of the considered tyres.

Looking at the lateral force characteristic curve in Figure 3.31, it can be noted that the cargo bike tyre reaches the lowest values overall. The e-bike tyre and the road racing tyre, instead, seem to reach very similar values for low slip angles, and in fact their cornering stiffness values are very close, having a gap of 3.3 N/° only, as it can be seen in Table 3.25.

The road racing bike tyre, however, ceases to be similar to the e-bike tyre once the non-linear part of the curve begins, reaching values that are lower than the e-bike tyre ones. In fact, it seems that the e-bike tyre has a longer linear section of the characteristic

curve, which allows it to reach higher values of lateral force in modulus. For what concerns the cargo bike tyre, it actually doesn't seem to be entering the non-linear part of the curve in the considered slip angle values.

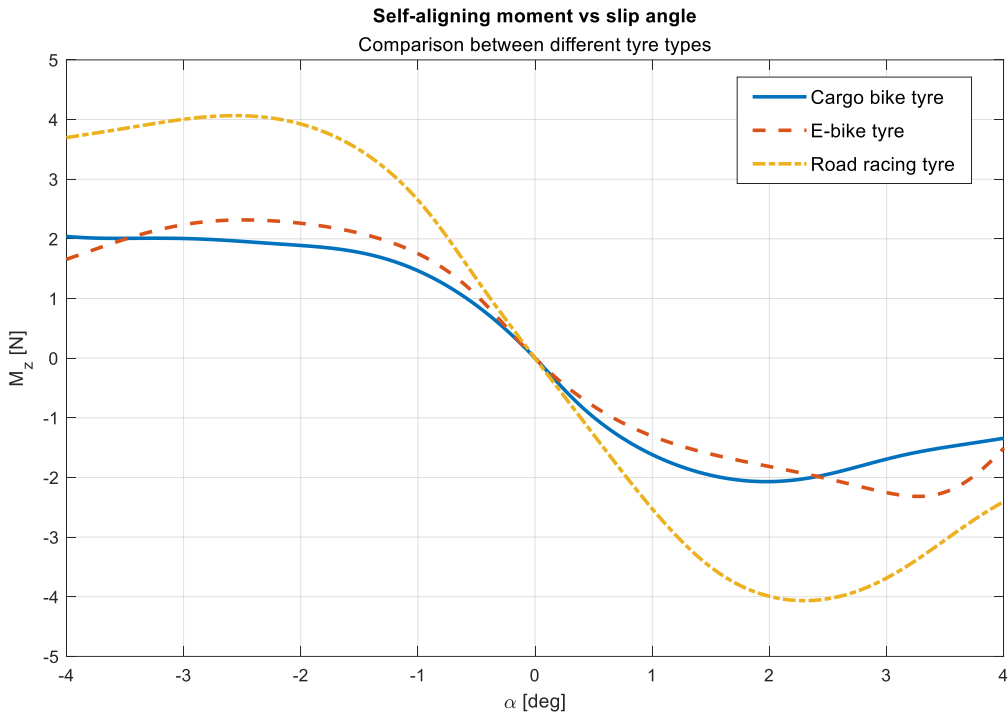


Figure 3.32: Self-aligning torque plot as a function of the side slip angle for the analysed tyre categories under the testing conditions specified in Table 3.25.

For the self-aligning torque (Figure 3.32), it can be noticed that the cargo bike tyre and the e-bike tyre have very similar trends and reach similar values, while the road racing tyre is the curve that reaches the highest values in modulus of the three categories, even getting to peak values that are almost the double of highest values of the other two tyres. It also shows two very well defined and symmetric peaks, while the other two present asymmetry in the non-linear zone of the graph.

Drawing conclusions, the cargo bike tyre was expected to have the lowest values in both characteristic curves (lateral force and self-aligning torque). In fact, its main function is not to provide optimum grip and/or performance, but to carry higher loads, filtering as much as possible the irregularities of a typical city road profile.

On the other hand, the e-bike tyre and the road racing tyres are mainly made for road use, therefore they have high grip as their key design goal, with the first having to be stable even at medium-high speeds while the latter must maximize performance.

This explains why both of them have a very high cornering stiffness, which consequently translates into higher lateral forces. Being the cornering stiffness values

so similar between the two tyres and knowing that the vertical load during the tests only differs by 4 N, it can be concluded that the difference in values observed in the self-aligning torque curve is caused by the combined effect of the inflation pressure and of geometric, structural and material differences. As reported in Table 3.25, the road racing tyre is the only one to have not been tested at 400 kPa, but at 350 kPa. Focusing on the linear zone and approximating F_y as equal between the two curves, it can be easily understood that the inflation pressure has a very high impact on the pneumatic trail, since it is the term that connects M_z to F_y , as explained in Section 3.1.2. On top of that, geometric, structural and material properties of the tyres come into play to determine the way in which the inflation pressure impacts the characteristics of each of the curves. The narrow profile, the less engraved thread and the softer compound of the road bike tyre, compared to the e-bike's, is probably chosen by the manufacturer to obtain these performances.

4 Static Analysis

In this Chapter the static tests, performed during the thesis work, are presented. They involved the study and the analysis of two important tyre properties: the lateral and the vertical stiffnesses. Correlated to the latter, the contact patch area was defined, thanks to specific films, and measured. Finally, starting from some properties of the tyre, the relaxation length was calculated.

All these properties were evaluated at different vertical load and inflation pressure conditions in order to go in detail on the effects related to a change of these external parameters. Moreover, the static experimental campaign considered the use of two different tyres for each measured quantity, making possible also a comparative analysis.

4.1. Vertical Stiffness Analysis

The vertical stiffness is the property of the tire that indicates how much the tyre is displaced under the action of a vertical force and it can be seen as the combination of the structural stiffness of the tyre and the air stiffness. The structural stiffness is function of the tyre's construction, mainly the sidewall's, and it is computed by measuring the tyre vertical stiffness at zero inflation pressure. On the other hand, the air stiffness is a characteristic that depends on the inflation pressure and it is calculated as the difference between the vertical stiffness and the structural one [44]. The calculation of the structural stiffness alone is challenging, for this reason our tests were focused on the determination of the overall vertical stiffness. This property is very important because it can be helpful in evaluating tyre performance, in particular the vertical dynamics (related to comfort and to the rolling impedance) [45]. Moreover, the higher is the vertical stiffness the lower is the rider's comfort [46]. Another important aspect is represented by the influence of the vertical stiffness on the contact patch dimension and thus on the development of lateral and longitudinal forces.

It is well-known in literature that the tyre, in the vertical dynamics of a general vehicle, can be modelled as an ordinary coil spring, thus the vertical stiffness is computed from the curve of the vertical load as function of the tyre drop.

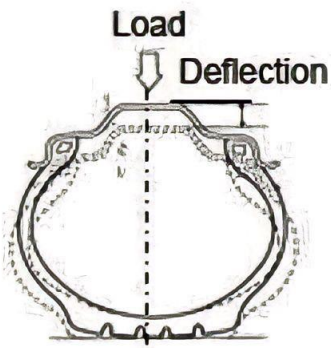


Figure 4.1: The tyre cross section under the action of a vertical load undergoes a vertical deflection (tyre drop).

The application of a vertical force on the hub, mainly due to the rider's weight, brings to a structural change of the part of the tyre in contact with the ground. Moreover, the contact patch surface increases and the overall height of the tyre decreases. Focusing on the vertical axis, it is possible to define the tyre drop as the difference between the height of the undeformed tyre and the height of the tyre when a vertical load is applied. It is important to specify that the tyre height is intended as the distance between the minimum internal diameter of the rim and the outer edge of the tyre. (Figure 4.1)

4.1.1. Set-up for the measurement

In order to define the vertical stiffness of the tyre, an experimental approach was developed. It is a simple method that is based on the use of a height gauge for the measurement of the tyre height.

Once the wheel is mounted, the vertical load and the inflation pressure are set, a thick steel plate is positioned on the flat track belt. This plate is used to have a non-deformable surface in contact with the tyre when the measurement is performed and to have a flat surface on which the height gauge can be positioned. The final set-up is shown in Figure 4.2.

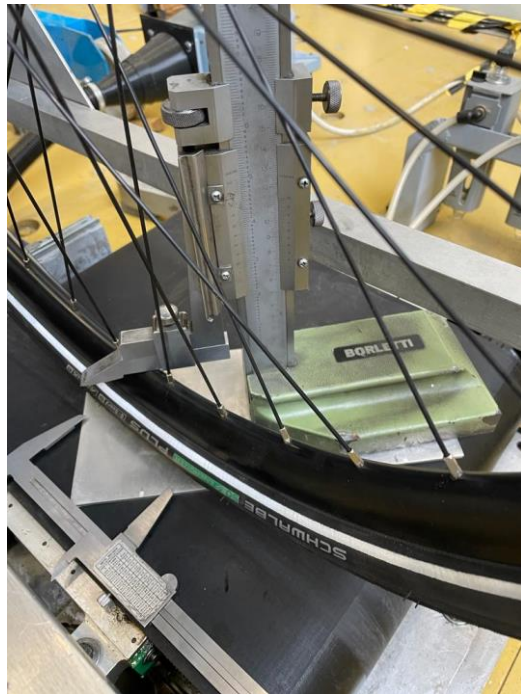


Figure 4.2: Complete set-up for the vertical stiffness measurement.

First, the undeformed height of the tyre has to be measured. The VeTyT frame is lowered to ensure a light touch between the tyre and the steel plate. The height gauge is positioned on the steel plate and the probe of the height gauge is inserted between the spokes, in correspondence of the point where the tyre is in contact with the steel plate. The probe measuring surface is put in contact with the rim, in this way the undeformed height of the tyre is measured.

Then, is fully lowered (full weight on the tyre) and the height gauge measures the tyre height under the application of a vertical load. The probe maintains the same position of the previous measurement, approximately the middle of the contact patch.

Each measurement is performed at least twice in order to consider the average of the measured values as the effective height, and to verify the data repeatability. In this way some measurement errors can be filtered.

Finally, the tyre drop is computed as the difference between the height of the undeformed tyre and the tyre height under the action of the vertical force.

The same procedure is followed for an increased value of vertical load. In this way a dataset is created and it is possible to plot the measured data in a Vertical load vs tyre drop graph. The relationship between the two variables is approximated as linear, thus a linear interpolation of the data is considered. The vertical stiffness for a given condition of pressure is the slope of the linear interpolation curve.

In the next section some examples of analysed tyres are reported.

4.1.2. Results

The experimental measurement of the vertical stiffness, described in the previous section, was performed for two tyres: SCH-T03 and SCH-T04. The choice of the two tyres was not random since the first one is a completely renewed version of the second one, thus a detailed comparison can be presented in terms of lateral stiffness.

Both the tyres were mounted on the rim *Shimano Deore HB-M525A 28"* (622) and were tested for three different inflation pressure values (300 kPa , 400 kPa , 500 kPa), each one for three different vertical loads (343 N , 404 N , 488 N).

At start the older version tyre (SCH-T04) is analysed. Table 4.1 shows the tyre drop values collected through the experimental measurements. In order to clearly understand the dependence of the tyre drop on the considered variables of inflation pressure and vertical load, the following graphs were drawn: in Figure 4.3a the tyre drop is shown as function of the vertical load, when varying the inflation pressure; in Figure 4.3b the tyre drop is shown as function of the inflation pressure, when varying the vertical load.

Pressure [kPa]	Vertical Load [N]	Tyre drop [mm]
500	488	4.4
	404	3.8
	343	3.3
400	488	4.9
	404	3.9
	343	3.4
300	488	5.9
	404	5.1
	343	4.6

Table 4.1: Tyre drop measurements for SCH-T04.

The results obtained from the measurements on this tyre are coherent with respect to the expected behaviour of the tyre drop. The increase of the vertical load leads to an increase of tyre drop (Figure 4.3a) with a trend that is almost linear. Moreover, the distance between the curve at 300 kPa and the one at 400 kPa is much greater than the distance between the curve at 400 kPa and the one at 500 kPa , even though the increase in pressure is constant.

On the other hand, the tyre drop decreases with the increase of the inflation pressure, but in this case the trend is not as linear as before (Figure 4.3b). It is possible to notice that the slope of the second piecewise interpolation function is different from the first one. It seems to reach a plateau value, however this insight cannot be confirmed due to lack of data for higher inflation pressures.

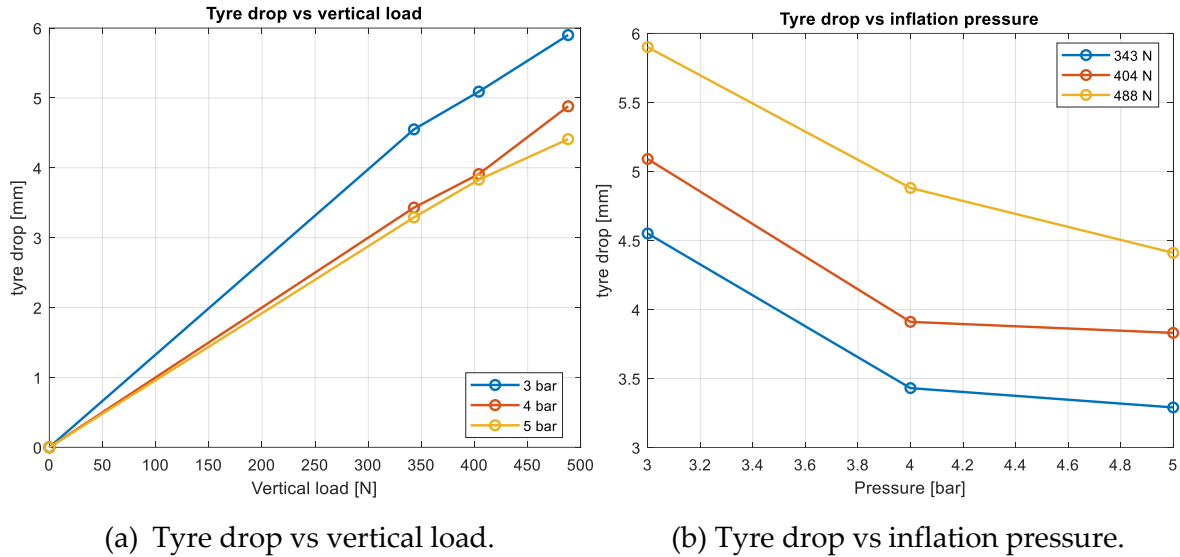


Figure 4.3: Tyre drop as function of vertical load and inflation pressure for SCH-T04.

The same analysis is done for the SCH-T03, the tyre drop values are collected in Table 4.2.

Pressure [kPa]	Vertical Load [N]	Tyre drop [mm]
500	488	4.7
	404	4.0
	343	3.6
400	488	5.1
	404	4.2
	343	3.9
300	488	6.9
	404	5.7
	343	5.4

Table 4.2: Tyre drop measurements for SCH-T03.

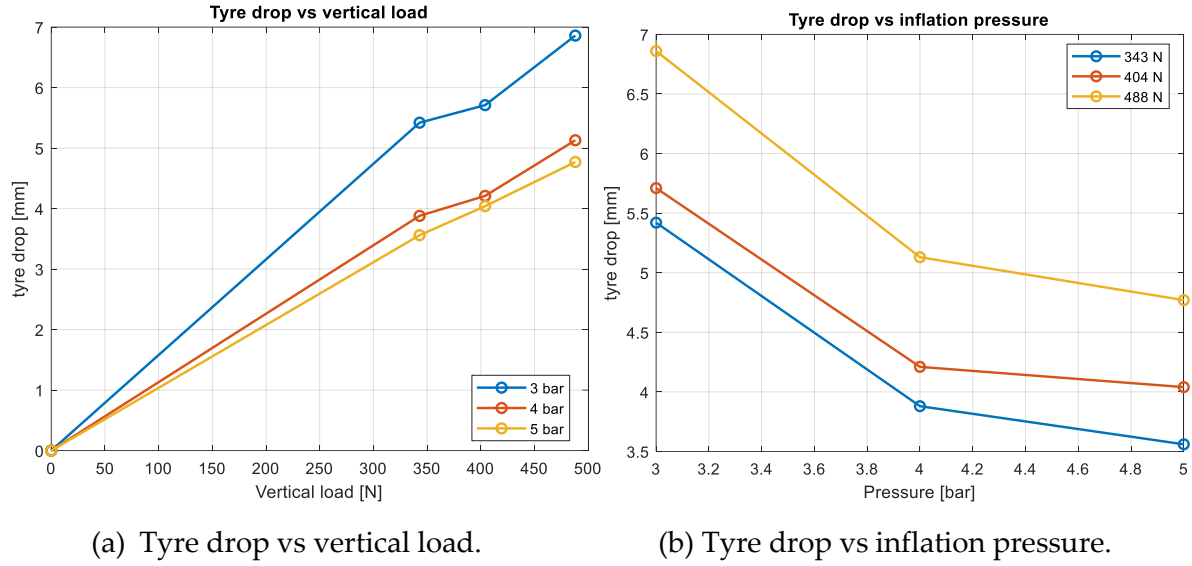


Figure 4.4: Tyre drop as function of vertical load and inflation pressure for SCH-T03.

Looking at Figure 4.4a the tyre drop increases almost linearly with the vertical load. Also, for this tyre the distance between the curve at 300 kPa and the one at 400 kPa is much greater than the distance between the curve at 400 kPa and the one at 500 kPa , even though the increase in pressure is constant. In Figure 4.4b it is possible to notice that the tyre drop tends to non-linearly decrease when the inflation pressure increases.

The two tyres can be compared by focusing on the tyre drop analysis, as said before, to look at the effect of the new Addix E-Compound ideated specifically for e-bikes, by Schwalbe®. For this purpose, in Figure 4.5a and 4.5b the tyre drop for both the tyres is shown as function of vertical load and inflation pressure.

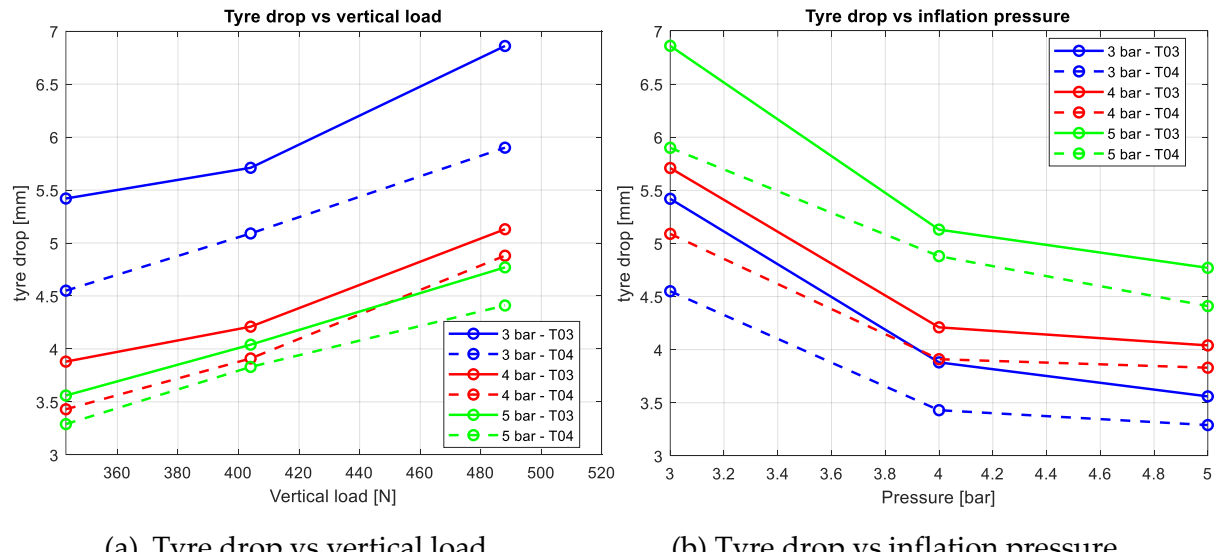


Figure 4.5: Tyre drop as function of vertical load and inflation pressure for, in the continuous line, SCH-T03 and for, in dashed line, SCH-T04.

The two figures (Figure 4.5a and 4.5b) put in evidence that the curves of the tyre drop are higher for SCH-T03 than for SCH-T04, for all inflation pressure values and vertical loads.

The two experimental measurements showed an almost linear relationship between the vertical load and the tyre drop in both cases. For this reason, it was decided to fit the collected data with a linear interpolation (Figure 4.6).

The slope of the linearised curve represents the vertical stiffness of the tyre in a defined condition of inflation pressure. In Table 4.3 the vertical stiffness values are collected for both SCH-T03 and SCH-T04.

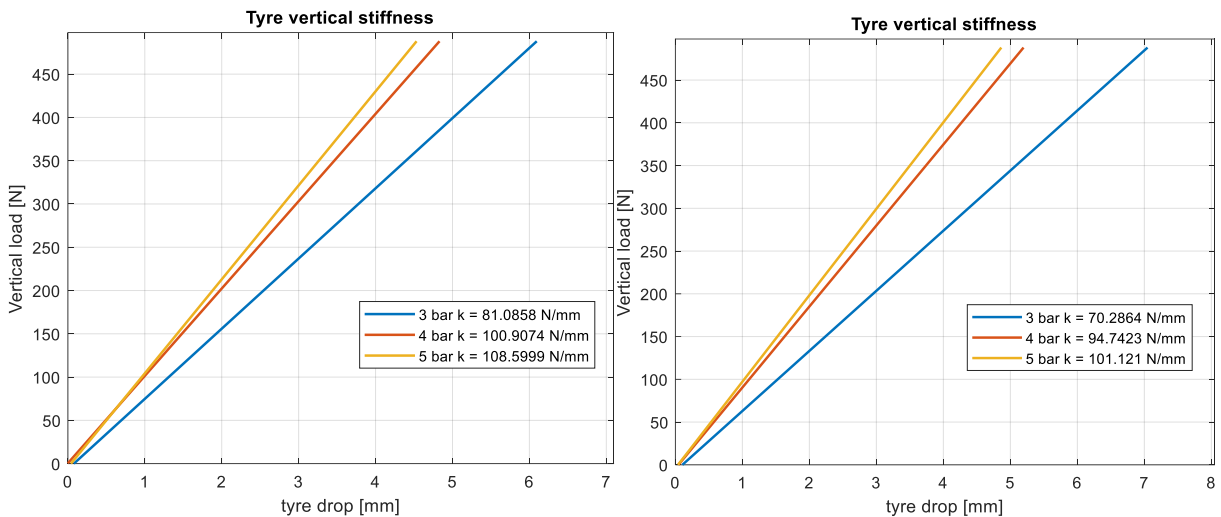


Figure 4.6: The vertical load function of the linearized tyre drop: at left SCH-T04, at right SCH-T03. In the legend, the vertical stiffness (k in legend) is indicated for the given inflation pressure value.

Looking at Figure 4.6 it is possible to notice that the vertical stiffness increases with the increase of the inflation pressure. This behaviour is expected as the increase of the pressure leads to an increase of the air stiffness, that is responsible of the increase of the tyre deformation resistance. It is not possible to precisely define if the increase of the tyre vertical stiffness is totally or partly due to the air stiffness. Furthermore, the increase is not linear, it is greater for the increment of inflation pressure from 300 kPa to 400 kPa with respect to the increment from 400 kPa to 500 kPa. A similar behaviour it was found in literature from a study on motorcycles tyres, in fact, for the tested tyres, the vertical stiffness seemed to saturate about 300 kPa [47].

According to the static measurements, it is evident that, for the same value of pressure, the vertical stiffness SCH-T04 is higher than the one of the new SCH-T03 and therefore, by hypothesis, has higher discomfort level.

It is well known in literature that the rolling resistance is related to the tire stiffness [48], in fact the more pliable the tire is, the higher is the rolling resistance. Moreover, the higher the pressure, the higher is the vertical stiffness, the lower is the rolling resistance. It would seem that the more we inflate the tire, the smaller the rolling resistance. In reality, increasing too much the tyre causes a reduction of the contact area, which may lead to the deterioration of the vehicle's driving performance [49]. The manufacturer published in the tyre catalogue the rolling resistance, the road grip, the off-road grip, the protection (puncture) and the durability, with a value from zero to a maximum of six. This information can validate the increase of the rolling resistance with the decrease of the vertical stiffness, as SCH-T03 has lower vertical stiffness and higher rolling resistance (Table 4.3). On the other hand, this tyre has higher grip both on road and off-road.

SCH-T04		SCH-T03	
Pressure [kPa]	Vertical stiffness [N/mm]	Pressure [kPa]	Vertical stiffness [N/mm]
300	81.0858	300	70.2864
400	100.9074	400	94.7423
500	108.5999	500	101.121



Table 4.3: Vertical stiffness values of SCH-T04 in the left part and of SCH-T03 in the right part; down, the indicators from the manufacturer: a) SCH-T04 [30]; b) SCH-T03 [50].

4.2. Contact Patch Analysis

The tyre contact patch is the area of a tyre's tread that touches a specific surface and, thus, it is the only connection between the vehicle and the road. For a tyre with a grooved tread pattern, it can be noted that the presence of void areas does not contribute to the contact patch area.

It is a very important element, for example, in the longitudinal dynamics of the vehicle, as the longitudinal force is calculated as the integral of shear stress generated in the contact patch when the vehicle is moving. Moreover, it has a specific role in the generation of the lateral force, in fact the lateral force is a consequence of the lateral deformation of the contact patch when a side slip angle is imposed to the tyre. For these reasons the study of the contact patch and of the parameters that influences its size and shape is of high relevance.

The tyre contact patch's size depends on a variety of factors such as the inflation pressure and the vertical load. Since tyres continuously roll whenever the vehicles are driven, each tyre's contact patch only exists temporarily when its tread conforms to the road. Furthermore, as pneumatic tyres are flexible, the contact patch can be different when the vehicle is in motion than when it is static. In this section we propose a comparison between different methods used to calculate the area of the contact patch, considering a static experimental measurement. Dynamic analysis of contact patches is still not possible with VeTyT test-rig, due to technical limitations of the current set-up.

The tyres selected for this analysis were: VIT-T10 and VIT-T11. They were chosen in order to have a further analysis on the behaviour of the contact patch when considering two tyres with the same compound (same model of tyre), but different in width. They were both mounted on the rigid rim and were tested for three different inflation pressure values P (350 kPa , 550 kPa , 750 kPa) according to the maximum inflation pressure indicated by the manufacturer (800 kPa), each one for three different vertical loads F_z (340 N , 400 N , 490 N).

Based on the different combinations of inflation pressure and vertical load, it is possible to predict approximately the value of the area of the contact patch, indeed, it can be seen as the ratio between the vertical load and the inflation pressure (Eq. 4.1) [51]:

$$\text{Area} = \frac{F_z}{P} \quad (4.1)$$

This equation assumes that the inflation pressure is equal to the contact pressure. The results are shown in Table 4.4.

		Contact patch Area = Vertical Load/Inflation Pressure [mm ²]		
		Vertical Load [N]		
		340	400	490
Inflation Pressure [MPa]	0.35	971.4	1142.9	1400.0
	0.55	618.2	727.3	890.9
	0.75	453.3	533.3	653.3

Table 4.4: Area contact patch = Load/Pressure at different loads (340 N, 400 N, 490 N) and pressures (0.35 MPa, 0.55 MPa, 0.75 MPa).

However, it is well known in the road tyres literature that the contact pressure does not assume a constant value in the whole contact patch [52] and, moreover, some studies put in evidence that the mean contact pressure could be either lower as well as higher than the inflation one [51]. These undefined aspects led the discussion to another kind of approach.

In order to precisely define the contact patch, the Fuji Prescale pressure measuring film [53] was used. The Prescale film allows to easily measure pressure distribution and it is composed of two films: a so called “A-film” and a “C-film”. The A-film is made of a PET base coated with the micro-encapsulated colour-forming material, while the C-film is made of a PET base coated with the colour-developing material. The microcapsules are designed to react according to a specific level of pressure, so that the colour density corresponds to a precise level of pressure.

It is possible to consider the previous discussion as an indication of the possible mean value of the contact pressure and, thus, it was chosen the “Super Low Pressure” film (500 kPa to 2500 kPa). It could have a possible error on the measurement up to $\pm 10\%$ in the range of recommended temperature (20 °C to 35 °C) and humidity (35% RH to 80% RH). It is important to consider that this kind of sheet can also extend its boundaries up to 250 kPa for the lower value and up to 3000 kPa for the upper value, but with a possible greater measurement error. Also testing in condition of temperature and humidity different from the recommended can cause measurement errors. Since the purpose of this study is to measure the area and not to evaluate the distribution of pressure, these errors can be negligible.

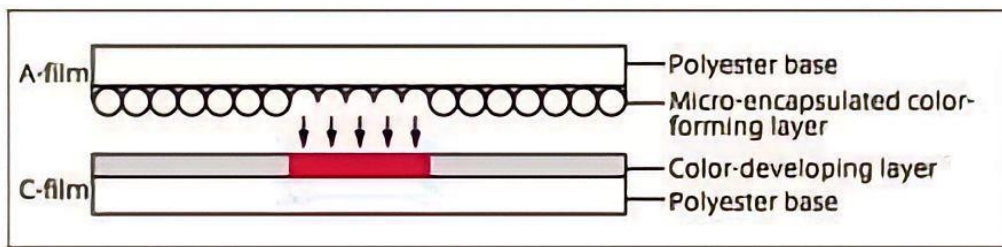


Figure 4.7: Working principle of the Prescale sheets: once the threshold pressure is overcome, the microcapsules in A-film react allowing the colour deposition on the C-film [53].

First, the films are placed on the flat track belt, having the rough surfaces of the films face each other (Figure 4.7). The tested tyre, at defined inflated pressure and under the specific vertical load, is mounted on the VeTyT, without touching the films. Lowering reasonably the frame of the VeTyT, the tyre applies a pressure (momentary or continuous) on the Prescale film that breaks the microcapsules and the colour-forming material reacts with the colour-developing material to generate colour. After some time (5 second for momentary pressure or 2 min for continuous pressure), the VeTyT frame is raised and a red patch, corresponding to the contact patch, is visible on the film.

VIT-T10 was taken as example for the comparison between the proposed procedures for calculating the contact patch area. The tests were performed in continuous pressure at about $18 - 20^\circ\text{C}$ and 50% RH, values measured with a temperature and humidity sensor. An example of the contact patch obtained from the test is shown in Figure 4.8. All the figures of the contact patch at different inflation pressure and vertical load are in Appendix A - Table 1 and Table 2.

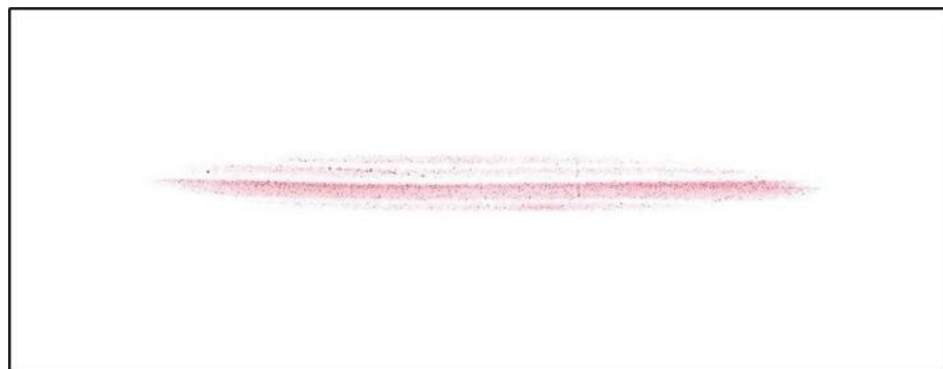


Figure 4.8: Contact patch of VIT-T10 at 350 kPa and 490 N.

Looking at Figure 4.8 it is possible to notice that there are shades of red that are more faded towards the outside of the contact patch and this is a proof of the non-constant

contact pressure in the contact patch. Moreover, there are a sort of white steps between the shades that represent the grooved tread pattern of the tyre used to provide a channel for the water, allowing the water to escape from underneath the tyre keeps the rubber in contact with the asphalt.

The contact patch of road bike tyres assumes an almost elliptical shape, for this reason a method for calculating the contact patch area is to measure the maximum length of the contact patch ($2a$), equal to twice the semi-major axis a , and the width of the contact patch ($2b$), equal to twice the semi-minor axis b . The area is computed according to Eq. 4.2.

$$Area = \pi \cdot a \cdot b \quad (4.2)$$

The results from this approximation are collected in Table 4.5, where the calculated area for different combinations of inflation pressure and vertical load is indicated.

Contact patch Area, ellipse approximation [mm ²]				
		Vertical Load [N]		
		340	400	490
Inflation Pressure [kPa]	350	756.3	770.5	895.4
	550	494.8	590.6	692.7
	750	434.3	494.8	603.2

Table 4.5: Area contact patch as elliptical, at different loads (340 N, 400 N, 490 N) and pressures (350 kPa, 550 kPa, 750 kPa). VIT-T10.

From this analysis the trend of the contact patch area varying singularly the inflation pressure and the vertical load is confirmed [54]. Increasing the vertical load, the contact patch area increases and this is due to the fact that the tyre drop increases and, thus, more tread is in contact with the flat track belt. On the other hand, increasing the inflation pressure, the contact patch area decreases thanks to the increase in the vertical stiffness of the tyre (air stiffness component as seen in the Section 4.1).

The contact patch has not a perfect elliptical shape as it is possible to see looking at Figure 4.9. Moreover, the ellipse does not take into account the empty parts of the contact patch due to the tread grooves.

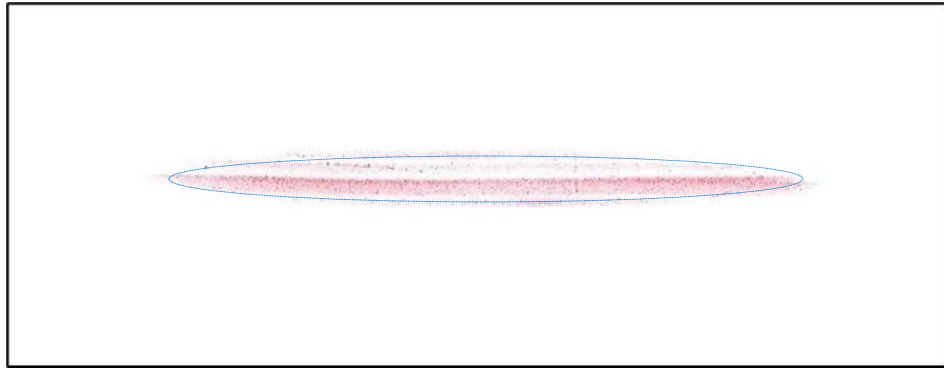


Figure 4.9: Contact patch of VIT-T10 at 350 kPa and 490 N compared with the elliptical approximation.

A more precise and accurate estimation of the area of the contact patches was obtained using the software ImageJ® [55], employed for the acquisition, the analysis and the processing of images. The contact patches were scanned and the images were processed by the software. It is important to set the scale, in this case A4, and then to select a threshold that colours accordingly the contact patch in red. In Figure 4.10 the interface of ImageJ® is shown, together with the set up that allows computing the relative area value.

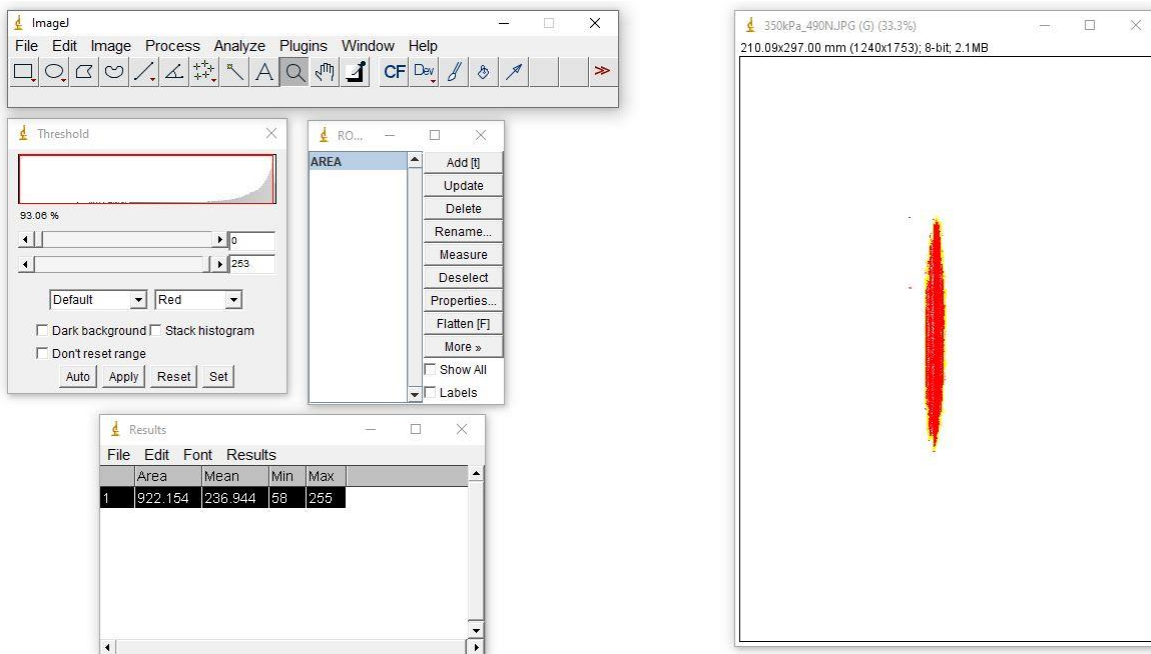


Figure 4.10: Example of contact patch analysis through ImageJ® software, importing the image, setting the scale, adjusting the saturation threshold (red area), selecting the area of interest (yellow circle), analysing and exporting the results. VIT-T10 at 350 kPa and 490 N .

The results from this analysis are shown in Table 4.6. The values of the contact patch area obtained with ImageJ® are higher than the one obtained with the elliptical approximation for almost all the combinations of inflation pressure and vertical load. This evidence can be explained looking at the contact patch, in fact, far from the centre, it is wider with respect to the approximated ellipse. The only exception is for the case at 350 kPa and 340 N, where, far from the centre, the contact patch is less wide than the approximated ellipse.

		Area with Imagej® [mm ²]		
		Vertical Load [N]		
		340	400	490
Inflation Pressure [kPa]	350	718.3	808.0	922.2
	550	566.1	628.4	796.1
	750	518.6	573.4	696.0

Table 4.6: Area contact patch with the software ImageJ®, under different loads (340 N, 400 N, 490 N) and pressures (350 kPa, 550 kPa, 750 kPa). VIT-T10.

The analysis with ImageJ® is more precise, but there are still problems linked to the scale setting, to the choice of the saturation threshold and, most of all, to the selection of non-uniform area (presence of tread grooves). To overcome these aspects, a colour-analysing Matlab® script was developed and used. It processes the scanned image firstly by transforming it into a grayscale image and then into a matrix of numbers between 0, representing the black colour, and 255, representing the white colour. It was reasonably chosen a threshold for the pixel colours that have to be counted and, in this way, all the pixels with, for sure, a colour different from pure white (*TotalColorPixels*) are counted. Then, they are converted into square millimetres (Eq. 4.3) through the *dpi* (dots per inch), the measure of resolution of the image.

$$Area = TotalColorPixels \cdot (0.0254/dpi)^2 \cdot 10^6 \quad (4.3)$$

Where *dpi* is equal to 150 from the property of the scanned image of the contact patch.

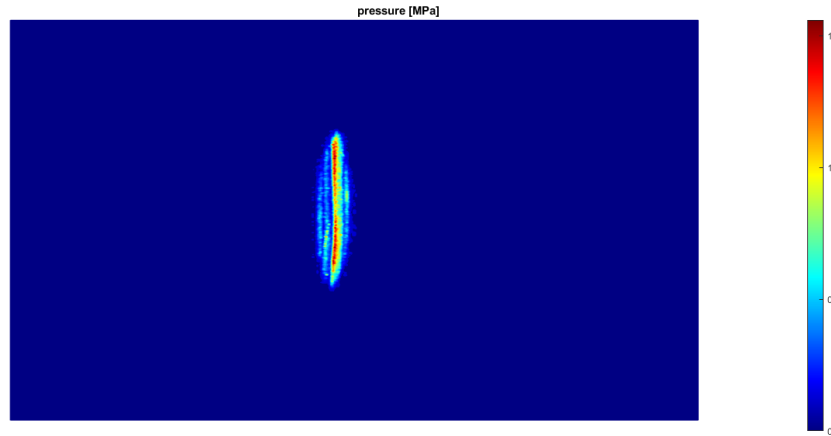


Figure 4.11: Contact patch of VIT-T10 at 350 kPa and 490 N with the Matlab® script. The colours indicate an approximated value of pressure and the figure is taken only as an indication even though the vertical load obtained by multiplying the average pressure inside the contact patch with the calculated area is 480 N (very similar to the applied load).

The Matlab® script is also able to define a pressure map, Figure 4.11, thus it is possible to appreciate the separations between the grooves as well as the fact that, in the represented case, the tyre is pressing more on the ground by its right side. The latter is an evidence that could be explained by a possible asymmetry in the tread width or with a possible mass positioning error, i.e., the masses used for setting the vertical load were not aligned with the longitudinal axis of the VeTyT. This last approach for determining the contact patch area is considered the most precise between all the ones presented in this discussion, for this reason it is taken as a reference for the determination of the contact patch area also for the VIT-T11. The area values are shown in Table 4.7.

Area with Matlab® script [mm ²]							
	Vertical Load [N]						
	340		400		490		
	Value	%	Value	%	Value	%	
Inflation Pressure [kPa]	350	627.2	-	687.1	10%	874.6	39%
	550	500.1	-20%	596.7	-5%	743.7	19%
	750	464.1	-26%	519.8	-17%	650.4	4%

Table 4.7: Area contact patch of VIT-T10 with the Matlab® script, at different loads (340 N, 400 N, 490 N) and pressures (350 kPa, 550 kPa, 750 kPa). The “%” column indicates the percentage variation of the considered contact patch area value with respect to the one at 340 N and 350 kPa.

It is important to point out that each approach presented in this section confirms the same behaviour of the contact patch area, in fact, increasing the vertical load the contact patch area increases, while increasing the inflation pressure (towards over inflation condition) the contact patch area decreases. The maximum value is obtained for the lowest value of inflation pressure (350 kPa) and the highest value of vertical load (490 N). The minimum value is obtained for the highest value of inflation pressure (750 kPa) and the lowest value of vertical load (340 N). A better visualization of the results is depicted in Figure 4.12.

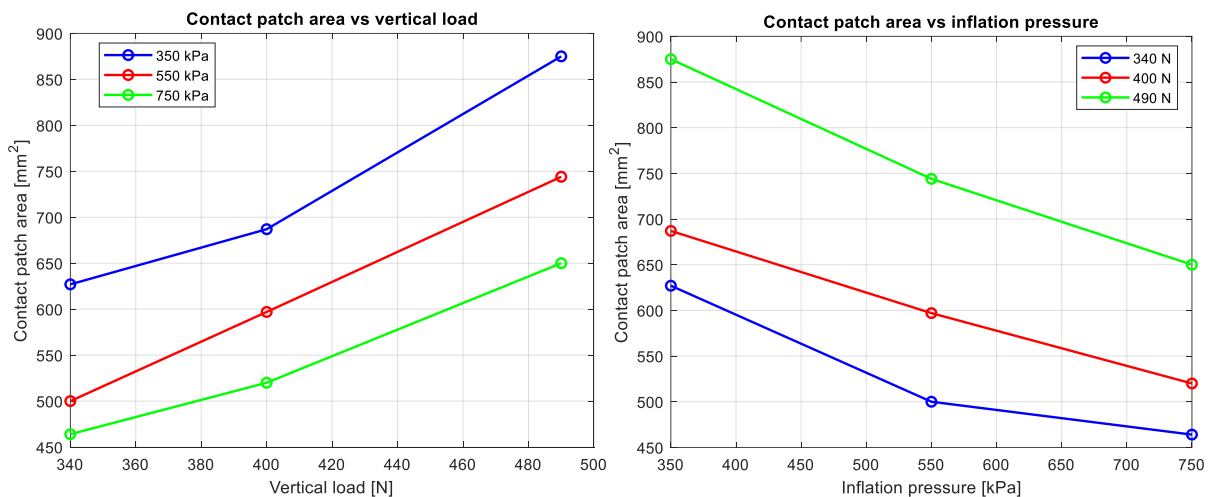


Figure 4.12: For the VIT-T10: on the left, the contact patch area as function of vertical load, when varying the inflation pressure; on the right, the contact patch area as function of inflation pressure, when varying the vertical load.

Considering the wider tyre VIT-T11, the contact patch area values obtained with the Matlab® script are summarized in Table 4.8. Also in this case, the contact patch area increases increasing the vertical load or decreasing the pressure. The maximum value is obtained for the lowest value of inflation pressure (350 kPa) and the highest value of vertical load (490 N). The minimum value is obtained for the highest value of inflation pressure (750 kPa) and the lowest value of vertical load (340 N).

Area with Matlab® script [mm ²]							
		Vertical Load [N]					
		340		400		490	
		Value	%	Value	%	Value	%
Inflation Pressure [kPa]	350	647.5	-	707.3	9%	896.4	38%
	550	511.2	-21%	615.3	-5%	750.1	16%
	750	465.3	-28%	521.6	-19%	613.7	-5%

Table 4.8: Area contact patch of VIT-T11 with the Matlab® script, at different loads (340 N, 400 N, 490 N) and pressures (350 kPa, 550 kPa, 750 kPa). The “%” column indicates the percentage variation of the considered contact patch area value with respect to the one at 340 N and 350 kPa.

In order to have a better understanding of the difference between the two tyres in terms of contact patch area, it is possible to compute a percentage variation in area for all the combinations of inflation pressure and vertical load. The percentage variation represents the variation of the contact patch area of the VIT-T11 with respect to the contact patch area of the VIT-T10 (Eq. 4.4). The values are collected in Table 4.9.

$$\%Variation = \frac{Area_{VIT-T11} - Area_{VIT-T10}}{Area_{VIT-T11}} \quad (4.4)$$

Percentage variation [%]							
		Vertical Load [N]					
		340		400		490	
		Value	%	Value	%	Value	%
Inflation Pressure [kPa]	350	3%		3%		2%	
	550	2%		3%		1%	
	750	0%		0%		-6%	

Table 4.9: Percentage variation in area at different loads (340 N, 400 N, 490 N) and pressures (350 kPa, 550 kPa, 750 kPa).

Looking at Table 4.9 it is possible to notice that the wider tyre has a higher contact patch area in almost all the combinations of inflation pressure and vertical load, with the only exception at 490 N and 750 kPa. For this condition, the scanned contact patch

of VIT-T10 seems to have a smear in the upper part [Appendix A, Table 1, 750 kPa and 490 N] and, thus, the exception can be justified as a measurement error. The percentage variation in area assumes very small values (between 0% and 3%) such that it is very difficult to assert that the wider the tyre the higher is the contact patch area. Indeed, since the order of magnitude of the measured quantity is very low, the uncertainties of measurement are present as well as possible wear of the tyres, then it can be a good approximation considering that the two tyres actually have the same contact patch area for every measured condition.

A further analysis could be done looking at the difference in shape of the contact patch. From literature it is possible to understand that a wider tyre has a wider and shorter contact patch [56]. Concerning the two analysed tyres, since the difference in width is very small (2 mm over 26 – 28 mm of total width), it is not possible to observe an evident difference in the shape of the contact patches (Figure 4.13).

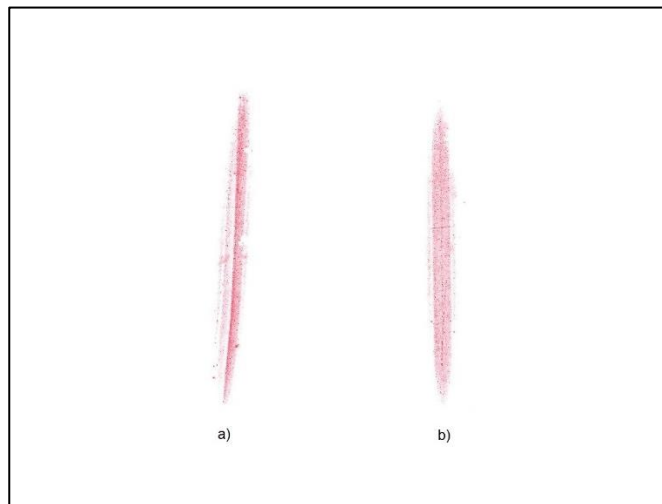


Figure 4.13: On the left (a), the contact patch of VIT-T10 at 550 kPa and 490 N; on the right (b), the contact patch of VIT-T11 at 550 kPa and 490 N.

4.3. Lateral Stiffness

The lateral stiffness of the tyre, intended as the resistance of the tyre under the action of a lateral force, was experimentally evaluated. Considering the tyre cross section represented in Figure 4.14, it is applied a lateral force due to the pulling action on a plate positioned under the tyre. Assuming the rim hold in the same position, this lateral force leads to a lateral displacement (d) of the tyre in contact with the plate.

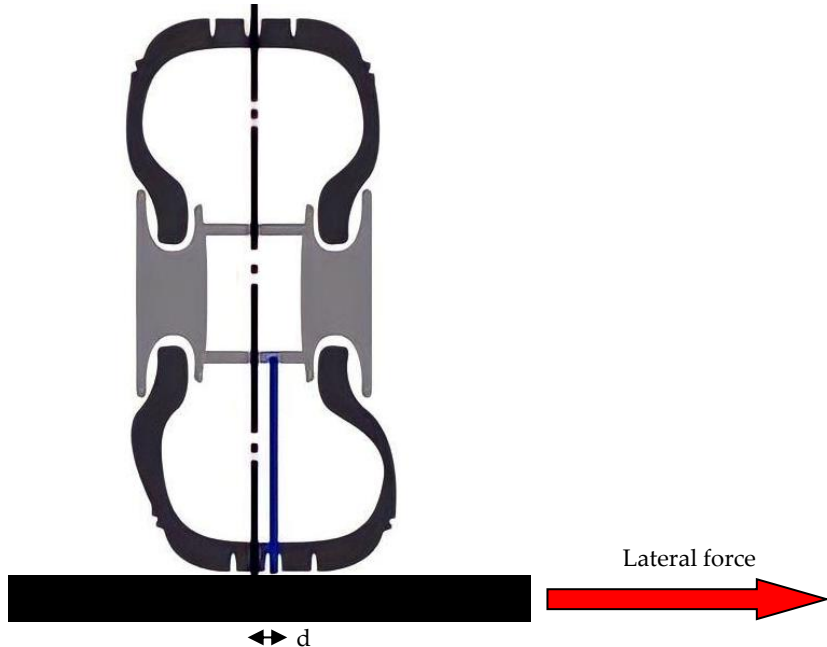


Figure 4.14: Tyre cross section under the action of a lateral force. The displacement “ d ” is the distance between the vertical axis of the undeformed tyre (black line) and the vertical axis of the deformed tyre (blue line).

We present an update from a previous method [25] that consisted in the use of an aluminium plate, covered with adhesive sandpaper, placed between the tyre and the flat track. Looking at Figure 4.15, it is possible notice that the total pulling force F_p applied to the plate is not equal to the force applied to the tyre (F_y), since a portion is lost due to friction (F_μ). For this reason, an additional thin steel plate was placed between the aluminium plate and the flat track belt and lubricated with oil, to reduce as much as possible the friction. In addition, a clamp was used to connect the tip of the rim to the chassis to reduce the lateral displacement of the rim.

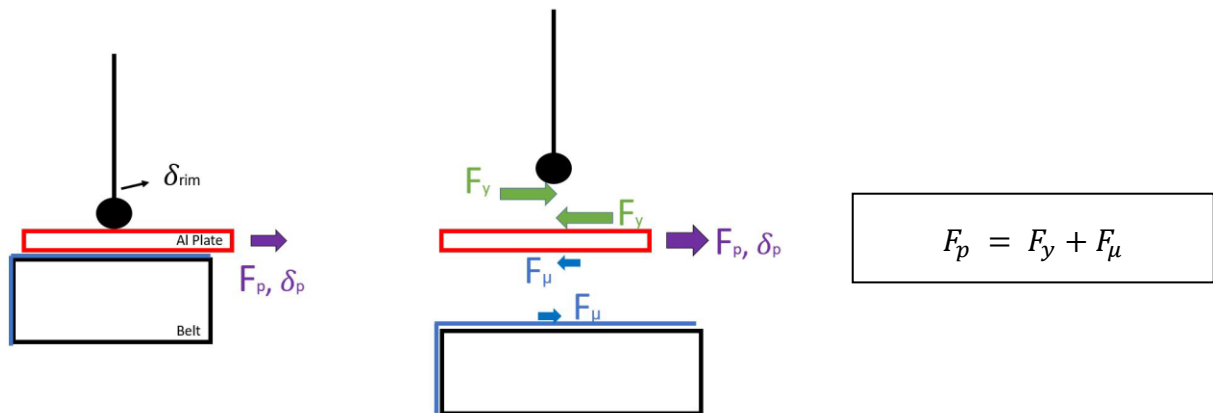


Figure 4.15: On the left, it is represented a detailed scheme of the forces acting on the set-up, where the rectangles stands for the belt (in black) and the aluminium plate (in red), the full black circle represents the tyre and the black line is the rim [25]; on the right it is expressed the equilibrium equation of forces at plate in the lateral direction.

The plate was pulled and, with the use of one dial gauge for the plate displacement and one for the rim displacement, the final displacement of the tyre was obtained as follows (Eq. 4.5).

$$\delta_{tyre} = \delta_{plate} - \delta_{rim} \quad (4.5)$$

Where the terms δ_{plate} and δ_{rim} refer to the plate displacement (measured with a dial gauge) and the rim displacement (measured with a dial gauge) respectively.

The lateral force applied to the tyre (F_y) was computed through an equilibrium equation (Eq. 4.6) in which the only variable is the total lateral force F_w measured by the Watt's linkage load cells.

$$F_y = F_w \cdot \left(\frac{L}{L_2} \right) \quad (4.6)$$

Where L is the distance between the rods of the Watt's linkage and the universal joint, L_2 is the distance between the contact patch centre and the universal joint and F_w is the total lateral force measured by the Watt's linkage load cells.

Drawbacks of the described method may be both the rotation of the aluminium plate and a possible steering of the tyre, despite the stiff connection with the chassis. A better configuration to the friction problem was investigated. In order to have a repeatable and accurate experimental method, since the dial gauges measure in the order of $mm/100$, the following guideline has been defined.

The procedure can be distinguished in three main phases: set-up, acquisition and data analysis.

The tools required are listed below:

- aluminium plate with two holes placed at the ends of the short side, with a sheet of sandpaper glued to one side ($P < 100$);
- Teflon-coated metal sheet;
- flexible steel wire rope (steel cord);
- d-ring shackle lock;
- long eye bolt;
- metal L-plate with one hole in the vertical surface;
- clamp and wooden blocks.

4.3.1. Set-up for the measurement

Once the wheel is mounted, the vertical load and the inflation pressure are set, the Teflon-coated metal sheet is positioned on the flat track belt with the aluminium plate

on top of it, to have the sandpaper upwards oriented. This operation is necessary to reduce the friction under the plate since Teflon-aluminium contact is featured by very low friction coefficient (0.24 between Teflon and aluminium [57]). The VeTyT frame is then lowered, trying to align the centre of the rim with respect to the centre of the plate. The aluminium plate and the eye bolt are connected by a system created with the use of the flexible steel wire rope and of the d-ring shackle lock. The wire rope is terminated at one end with a hard eye, thanks to a wire rope thimble, while the other end is inserted in the two holes, forming a loop. The eye part is then inserted in the d-ring shackle lock (Figure 4.16). The loop of the eye bolt is inserted into the d-ring shackle lock, while the threaded part is passed inside the hole in the vertical surface of the metal L-plate (firmly fixed to the ground). Finally, a nut is screwed on the threaded part of the eye bolt until it reaches the vertical surface of the metal L-plate.

By screwing the nut, we can pull the aluminium plate and move laterally the tyre. To make the rim stiffer, wooden blocks are placed between the rim and the VeTyT frame and locked in position with a clamp (Figure 4.17).



Figure 4.16: System used to connect the aluminium plate and the threaded metal rod.



Figure 4.17: The clamp rigidly connects the rim to the VeTyT frame thanks to the use of wooden blocks.

Four dial gauges must then be added to the set-up, for measuring both the plate and tyre displacement. They are divided as follows:

- two dial gauges are placed horizontally with respect to the vertical surface of the aluminium plate. They are positioned in marked points, equidistant with respect to the centre of the plate itself, thanks to the use of a caliper;
- two dial gauges indicators are placed horizontally with respect to the rim surface. They are positioned in marked points, equidistant with respect to the centre of the rim, thanks to the use of a caliper.

The use of two dial gauges for the aluminium plate is necessary to evaluate the displacement of its centre (average between the two measured values) δ_{plate} , while the use of the two dial gauges at the rim is necessary to derive the displacement of centre of the rim δ_{rim} (average between the two measured values). The final displacement of the tyre can be computed according to Eq. 4.5. In this way the effect of an eventual rotation of the aluminium plate and of the eventual steering of the tyre is taken into account.

The set-up for the evaluation of the lateral stiffness is shown in Figure 4.18.



Figure 4.18: Complete set-up for the lateral stiffness measurement.

4.3.2. Acquisition phase

The signals from the Watt's linkage load cells can now be recorded, while a technician starts screwing the nut to displace the plate. The displacement is measured by the couple of dial gauges and the procedure is repeated for five times, always taking note of the measurements from the dial gauges.

The force recorded by the Watt's linkage load cells as function of acquisition time is shown in Figure 4.19.

If the F_w value at the start of the acquisition is different than zero, it must be subtracted to the whole acquisition so that the shown F_w value is just the one caused by the test. As it can be noticed, there are five steps due to the five displacements considered. Therefore, the arithmetic average of the F_w is calculated for every step and then associated with the corresponding displacement. The effective values of the lateral force exerted on the tyre, F_y , is computed with an equilibrium equation (Eq. 4.6), known F_w from the previous described elaboration.

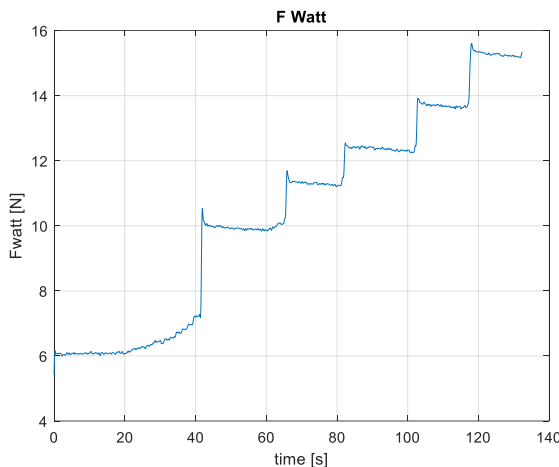


Figure 4.19: Example of total lateral force F_w measured by the Watt's linkage load cells as function of acquisition time. (VIT-T11 at 350 kPa and 340 N)

After that, the clamp and the wooden blocks are removed, the VeTyT is lifted and the metal plate is replaced to the initial condition for the second repeated test, with the same configuration.

4.3.3. Data Analysis

The data analysis phase consists in the study of the plot of the collected measured data in a F_y versus δ_{tyre} graph. An example is shown in Figure 4.20, where the two tests performed are defined with two different colors (blue and red) and the circles

represent the experimental data. The relationship between the two variables is approximated as linear, thus a linear interpolation of the data is considered and represented in Figure 4.20 with two curves. The lateral stiffness for a given condition of inflation pressure and vertical load is the average between the slope of the two curves obtained by the linear interpolation.

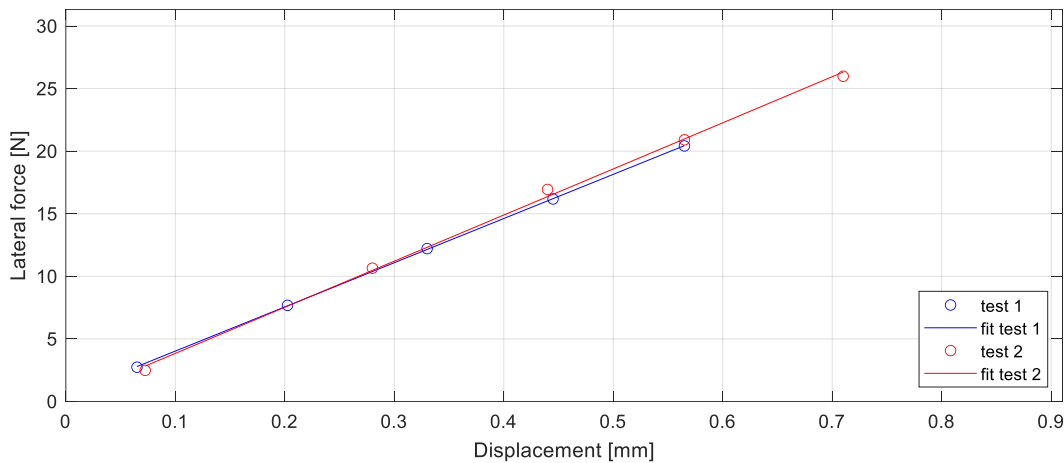


Figure 4.20: Example of a complete measurement results for a given condition of inflation pressure and vertical load. The circles are the measured data and the curves are the linear interpolation of the measured data. In blue the test 1 and in red the test 2. (VIT-T10 at 350 kPa and 490 N)

4.3.4. Results

The experimental measurement of the lateral stiffness, described in the previous sections, was carried out for two tyres: VIT-T10 and VIT-T11. They were chosen in order to have a further analysis on the behaviour of the lateral stiffness when considering two tyres with the same compound (same model of tyre), but different in width.

Both the tyres were mounted on the rigid rim and were tested for three different inflation pressure values (350 kPa, 550 kPa, 750 kPa), each one for three different vertical loads (340 N, 400 N, 490 N).

For the VIT-T10 two sequential tests were carried out and the value of the lateral stiffness is obtained by an arithmetic average. The values are reported in Table 4.10 as function of inflation pressure and vertical load.

Lateral stiffness [N/mm]							
		Vertical Load [N]					
		340		400		490	
		Value	%	Value	%	Value	%
Inflation Pressure [kPa]	350	40.00	-	51.55	-	36.08	-
	550	42.00	5%	68.11	32%	75.24	109%
	750	52.00	30%	58.00	13%	55.00	52%

Table 4.10: VIT-T10 lateral stiffness values for different conditions of inflation pressure (350 kPa, 550 kPa, 750 kPa) and vertical load (340 N, 400 N, 490 N).

It can be noticed that the lateral stiffness depends both on the vertical load and on the inflation pressure. The percentage value for each load is calculated by taking as reference the value at the lowest pressure.

Moreover, keeping the vertical load constant:

- For vertical load equal to 340 N, the lateral stiffness increases with the increase of the inflation pressure;
- For vertical load of 400 N, the lateral stiffness increases and then decreases with the increase of the inflation pressure;
- For vertical load equal to 490 N, the lateral stiffness increases and then decreases with the increase of the inflation pressure.

While, keeping the inflation pressure constant:

- For inflation pressure 350 kPa, the lateral stiffness increases and then decreases with the increase of the vertical load;
- For inflation pressure 550 kPa, the lateral stiffness increases with the increase of the vertical load;
- For inflation pressure 750 kPa, the lateral stiffness increases and then decreases with the increase of the vertical load.

Considering the 2-mm wider tyre VIT-T11, also in this case two sequential tests were carried out and the value of the lateral stiffness is obtained by an arithmetic average. The values are reported in Table 4.11 as function of inflation pressure and vertical load.

		Lateral stiffness [N/mm]					
		Vertical Load [N]					
		340		400		490	
Inflation Pressure [kPa]	Value	%	Value	%	Value	%	
	350	31.71	-	33.23	-	34.53	-
	550	42.00	32%	52.45	58%	46.87	36%
750	46.02	45%	37.53	13%	39.00	13%	

Table 4.11: VIT-T11 lateral stiffness values for different conditions of inflation pressure (350 kPa, 550 kPa, 750 kPa) and vertical load (340 N, 400 N, 490 N).

It can be noticed that the lateral stiffness depends both on the vertical load and on the inflation pressure. The percentage value for each load is calculated by taking as reference the value at the lowest pressure.

Moreover, keeping the vertical load constant:

- For vertical load equal to 340 N, the lateral stiffness increases with the increase of the inflation pressure;
- For vertical load of 400 N, the lateral stiffness increases and then decreases with the increase of the inflation pressure;
- For vertical load equal to 490 N, the lateral stiffness increases and then decreases with the increase of the inflation pressure.

While, keeping the inflation pressure constant:

- For inflation pressure 350 kPa, the lateral stiffness increases with the increase of the vertical load;
- For inflation pressure 550 kPa, the lateral stiffness increases and then decreases with the increase of the vertical load;
- For inflation pressure 750 kPa, the lateral stiffness decreases and then increases with the increase of the vertical load.

The two tyres belong to the same model, with the only difference in the width. A deeper analysis can be done considering the comparison between the tyres tested, trying to point out the similarities and the differences. The most important difference is that the values of the lateral stiffness of the VIT-T10, for each combination of vertical load and inflation pressure, are higher than the ones of the VIT-T11. A low tyre width

corresponds to a higher tyre lateral stiffness. This behaviour could be associated to the fact that reducing the tyre width, for a given rim width, the tyre cross section could be more trapezoidal [58]. This effect leads to a better support of side forces and so a greater lateral stiffness. Furthermore, the reduction in the tyre width leads to a smaller deformation of the sidewall area, which brings to an increase in the lateral stiffness.

It is possible to consider an analogy with studies on car tyres. In the article in SAE international journal [59], the effect of the rim width on the tyre stiffnesses was investigated. A wider rim leads to an increase of the lateral stiffness up to 43% over the whole wheel load range for tyres of the dimension 17" resp. 18" [59].

Both the tyres have the same behaviour at constant vertical load, when varying the inflation pressure. For this reason, the plots of the lateral stiffness as function of inflation pressure, when varying the vertical load, are shown in Figure 4.21.

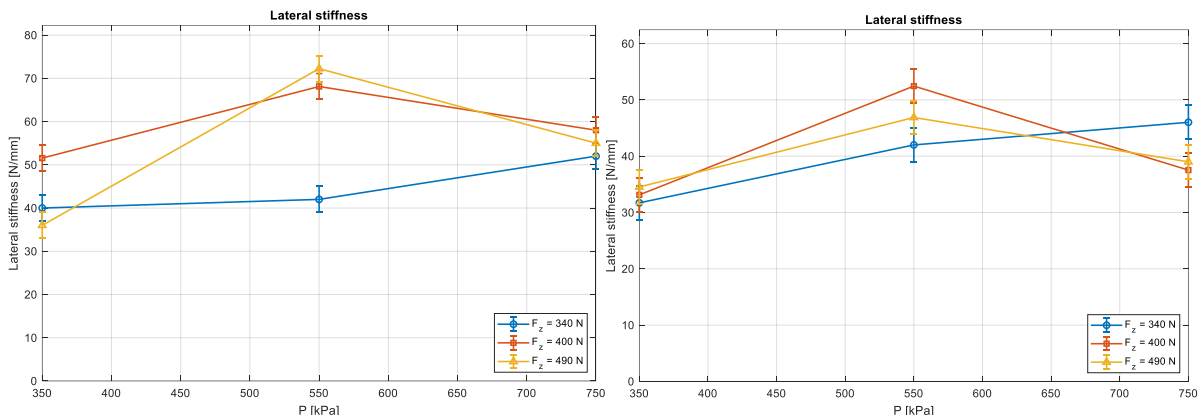


Figure 4.21: On the left, the lateral stiffness as function of inflation pressure, when varying the vertical load, of the VIT-T10; on the right, the lateral stiffness as function of inflation pressure, when varying the vertical load, of the VIT-T11.

The Figure 4.21 takes into account an uncertainty of $\pm 3\text{ N/mm}$ on the lateral stiffness to include approximations and measurement errors. Despite of the accurate description of the experimental method, it is difficult to ensure the correct measurement performed by the operator who reads the dial gauges values. The dial gauges are very sensitive to a slight displacement. Furthermore, Teflon coating does not make the contribution of F_μ null, thus a little difference between the force applied to the tyre and the force applied to the plate exists. Moreover, the lateral force derives from an average on the total lateral force F_w .

For the lowest vertical load tested (340 N), the lateral stiffness increases with the inflation pressure. For increasing values of vertical load the behaviour changes, the lateral stiffness reaches a saturation point at the intermediate value of inflation pressure and then decreases.

The same saturation can be found in other papers in the literature of road tyres [[60], [47]]. Moreover, a simplified formula to estimate the lateral stiffness can be used by considering a torus-like pneumatic tyre approximation [[25], [61]]. It would be difficult to formulate conclusions concerning the influence of pressure on the lateral stiffness behaviour without performing additional experiments.

4.4. Relaxation Length Analysis

The relaxation length is the property of a pneumatic tyre, in a defined condition (i.e., inflation pressure and vertical load), that describes the lagging behaviour of the lateral force response to the introduction of a side slip angle [62]. It is important since it characterizes the dynamic response of pneumatic tyres, in particular the vehicle handling [63]. In addition, the relaxation length has an effect on speed wobble [P1262-5130], that is the 4 – 10 Hz oscillation of the wheel(s) of single-track vehicles (i.e., motorcycles) during manoeuvring or at higher speeds [64]. Its value can change when considering different tyre conditions and different kinds of single-track vehicles. Moreover, in literature it was found that for motorcycle and scooter tyres the typical relaxation length value is in the range of 40 – 250 mm [65], while for bicycles the range is about 60 – 150 mm [25]. The literature also describes the longitudinal relaxation length as the parameter that reflects the longitudinal transient characteristics of the tyre [66]. In this section the relaxation length is analysed and can be defined as the distance that a tyre rolls before the lateral force reaches 63% of its steady-state value, when a slip angle is introduced [67]. This definition allows us to find the relaxation length starting from the measurement of the lateral force. Approximating the transient phenomenon with a first order differential equation (Eq. 4.7) [68], it is possible to fit the experimental measurements with the solution of the first order differential equation (Eq. 4.8) in order to find the parameter τ (time constant). Knowing that $\tau = \lambda/V$ and the forward speed V , then the relaxation length (λ) can be easily computed.

$$\frac{\lambda}{V} \cdot \frac{d F_y}{dt} + F_y = \bar{F}_y \quad (4.7)$$

Where:

- F_y [N]: transient lateral force;
- \bar{F}_y [N]: steady state value of the lateral force;

- λ [m]: relaxation length;
- V [m/s]: forward speed.

With solution:

$$\frac{F_y}{\bar{F}_y} = (1 - e^{-\frac{v}{\lambda}t}) \quad (4.8)$$

The graphical representation of this solution is shown in Figure 4.22, considering a variation of the relaxation length (λ) value in three levels (low, medium, high).

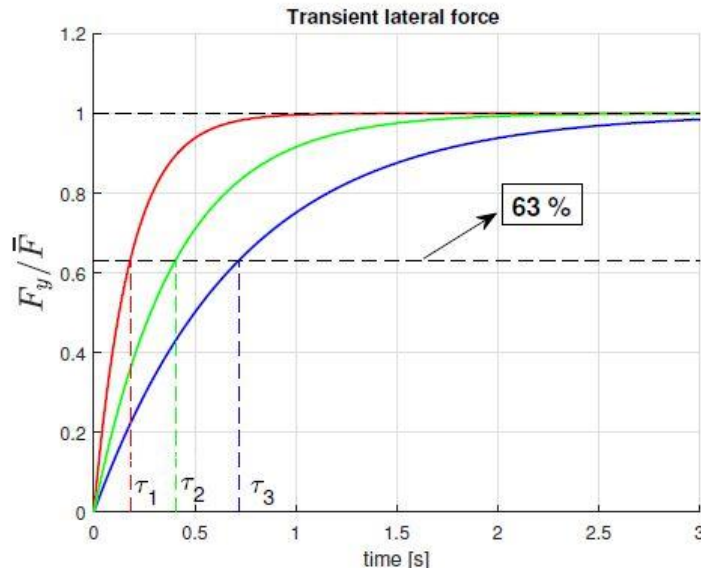


Figure 4.22: time solution of the first order differential equation when varying the relaxation length. The blue curve refers to the high λ , the green curve to the medium λ and the red to the low λ .

Looking at Figure 4.22 it is possible to see that the curve with the highest λ (blue curve) is slower in reaching the steady state lateral force, while, on the contrary, the curve with the lowest λ (red curve) is faster in reaching the steady state lateral force. Considering a single curve, the value of time for which the curves assume the value of 63% is the time constant τ . From this value, knowing the forward speed, the relaxation length is computed. The shorter the relaxation length, the better handling the tyre will offer. Through this method it is possible to point out also the presence of a forward speed dependence. When performing a curve too fast, the tyre may fail to provide the desired lateral force.

The relaxation length, in the most recent tyre models, is calculated according to a rigid ring model [65], which separates the tyre–road interaction into two parts. The first part is the contact patch, that has its own relaxation equation, while the second part is the tyre’s carcass, modelled as a rigid belt elastically connected to the rim by means of springs and dampers. The contact patch - rigid belt connection is modelled with residual springs and dampers. If the damping of the tyres and the effect of the self-aligning torque are neglected in this model, the relaxation length (σ) is computed with a simple first order equation:

$$\sigma = a \cdot m + C_{bF_\alpha} \cdot \left(\frac{1}{C_y} + \frac{r^2}{C_{xx}} + \frac{1}{C_{res}} \right) \quad (4.9)$$

Where:

- a [m] is the half-length of the contact patch;
- m [–] is the ratio of the adhesion zone length to the total length of the contact patch [m];
- C_y [N/m] is the lateral stiffness;
- C_{xx} [$N \cdot m/rad$] is the rotational stiffness due to the camber mode;
- C_{res} [N/m] is a residual stiffness, computed as: $1/C_{res} = 1/C_c + 1/C_s$, where C_c [N/m] is the C-shape modal stiffness, while C_s [N/m] is the S-shape modal stiffness;
- C_{bF_α} [N/rad] is the cornering stiffness of the tyre.

Another way to calculate the relaxation length is through the ratio between the cornering stiffness (C_{Fy} [N/rad]) and the lateral stiffness (K_y [N/m]) of the tyre.

$$\lambda = \frac{C_{Fy}}{K_y} \quad (4.10)$$

This way of calculating the relaxation length results in a combination of a dynamically measured quantity (the cornering stiffness) and a statically measured quantity (the lateral stiffness). However, comparing the bicycle tyre relaxation length obtained with the Eq. 4.10 and the one obtained according with the Eq. 4.8, the two values could be about 40% different [35].

In this section the relaxation length is obtained by computing the ratio between the cornering stiffness and the lateral stiffness for two tyres: VIT-T10 and VIT-T11. In order to understand the relaxation length dependencies on the inflation pressure and on the vertical load, it was chosen to report the relaxation length for three different inflation

pressure values (350 kPa , 550 kPa , 750 kPa) and three different vertical load values (340 N , 400 N , 490 N).

The cornering stiffness values, computed accordingly to the definition described in Sector 3.1.3, and the lateral stiffnesses, computed in the Section 4.3.4, are resumed in Table 4.12 and Table 4.13 respectively.

Cornering stiffness [$\text{N}/^\circ$]				
		Vertical Load [N]		
		340	400	490
Inflation Pressure [kPa]	350	89.14	99.55	109.85
	550	88.53	97.38	110.36
	750	80.41	92.17	105.35

Cornering stiffness [$\text{N}/^\circ$]				
		Vertical Load [N]		
		340	400	490
Inflation Pressure [kPa]	350	103.64	111.47	119.66
	550	90.29	105.65	117.21
	750	86.26	95.55	111.16

Table 4.12: The cornering stiffness values for different conditions of inflation pressure (350 kPa , 550 kPa , 750 kPa) and vertical load (340 N , 400 N , 490 N), for: on the left, the VIT-T10 tyre; on the right, the VIT-T11 tyre.

Lateral stiffness [N/mm]				
		Vertical Load [N]		
		340	400	490
Inflation Pressure [kPa]	350	40.00	51.55	36.08
	550	42.00	68.11	75.24
	750	52.00	58.00	55.00

Lateral stiffness [N/mm]				
		Vertical Load [N]		
		340	400	490
Inflation Pressure [kPa]	350	31.71	33.23	34.53
	550	42.00	52.45	46.87
	750	46.02	37.53	39.00

Table 4.13: The lateral stiffness values for different conditions of inflation pressure (350 kPa , 550 kPa , 750 kPa) and vertical load (340 N , 400 N , 490 N), for: on the left, the VIT-T10 tyre; on the right, the VIT-T11 tyre.

Applying the Eq. 4.9, the relaxation length values of the two tyres for all the combinations of inflation pressure and vertical load are collected in Table 4.14.

Relaxation length [mm]							
		Vertical Load [N]					
		340		400		490	
		Value	%	Value	%	Value	%
Inflation Pressure [kPa]	350	127.68	-	110.65	-	174.44	-
	550	120.77	-5%	81.92	-26%	84.04	-52%
	750	88.60	-31%	91.05	-18%	109.75	-37%

Relaxation length [mm]							
		Vertical Load [N]					
		340		400		490	
		Value	%	Value	%	Value	%
Inflation Pressure [kPa]	350	187.28	-	192.21	-	198.56	-
	550	123.18	-34%	115.41	-40%	143.27	-28%
	750	107.40	-43%	145.89	-24%	163.31	-18%

Table 4.14: The relaxation length values for different conditions of inflation pressure (350 kPa, 550 kPa, 750 kPa) and vertical load (340 N, 400 N, 490 N), for: at the top, the VIT-T10 tyre; at the bottom, the VIT-T11 tyre. The “%” column indicates the percentage variation of the considered relaxation length value with respect to the one at 350 kPa.

VIT-T11, the wider tyre, has higher relaxation length values for each combination of vertical load and inflation pressure with respect to VIT-T10.

This result is due to its higher cornering stiffness and its lower lateral stiffness. This effect results in a slower tyre response for the wider tyre.

Looking at the trend of the relaxation length when varying the inflation pressure and the vertical load, we note that for the lowest value of inflation pressure (350 kPa) the relaxation length value is the highest. This means that the response of the tyre becomes “lazy” at low inflation pressure values. The minimum value of relaxation length is not obtained with a fixed combination of inflation pressure and vertical load.

The relaxation length values collected in Table 4.14 are shown in Figure 4.23 for the VIT-T10 and in Figure 4.24 for the VIT-T11. The relaxation length is reported as function of the vertical load, when varying the inflation pressure. Another peculiar behaviour that is common among the two analysed tyres can be noticed looking at the

curves at 550 kPa and 750 kPa. At the lowest level of vertical load, the curve at 550 kPa is above the one at 750 kPa, thereby, an increase in the pressure value leads to the relaxation length reduction. However, for the other two values of the vertical load the trend is inverted, with the 750 kPa curves having higher relaxation length values than the 550 kPa ones.

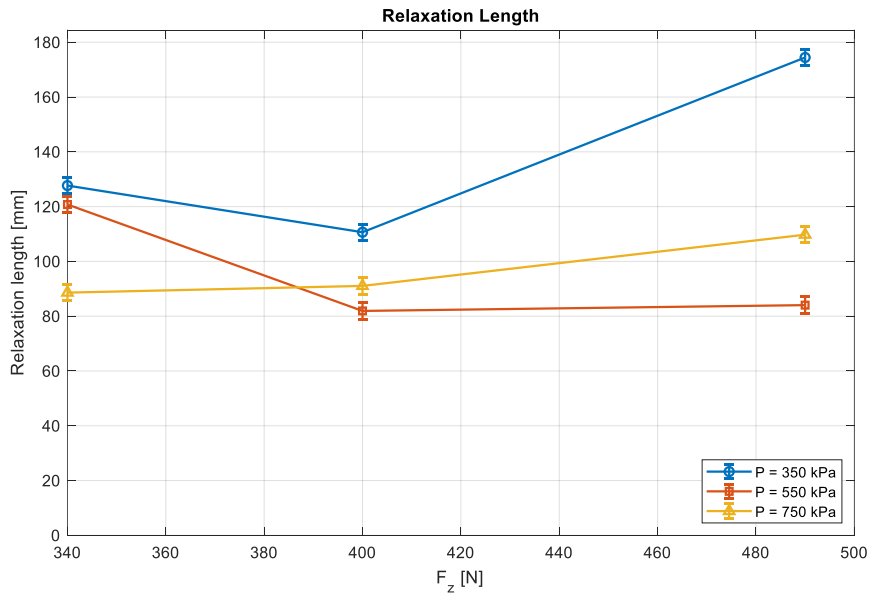


Figure 4.23: The relaxation length of the VIT-T10 as function of vertical load, when varying the inflation pressure.

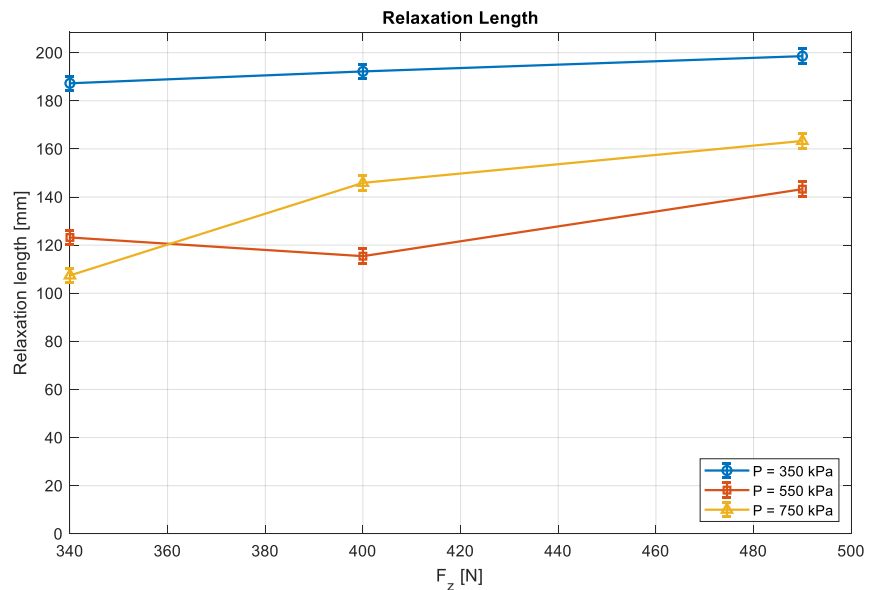


Figure 4.24: The relaxation length of the VIT-T11 as function of vertical load, when varying the inflation pressure.

Figure 4.23 and Figure 4.24 take into account an uncertainty of $\pm 3\text{ mm}$ on the relaxation length to include all the approximations and measurement errors present in the determination of the cornering stiffness and of the lateral stiffness.

The manufacturer seems to have conceived the design of the tyre in order to have lower relaxation length for values of vertical load similar to the weight of the rider (around 70 kg) and at intermediate values of inflation pressure. The choice to have this behaviour at intermediate pressure has the purpose of avoiding the drawbacks of overinflated and underinflated tyres, since lower pressures increase the contact patch area which increases fuel consumption, as well as the wear, higher pressures cause the opposite effect on the contact patch, reducing traction and performance.

5 VeTyT improvements

The aim of this Chapter is to present two preliminary studies on improvements that can be made on the VeTyT system. Moreover, the studies included a deep analysis of the main problem, the individuation of various alternative solutions and the selection of the most suitable one for our system. In the following, a new lateral translation system and a modified “height calibration” system are developed (Section 5.1). An important part of the analysis of tyres tested with the VeTyT is the processing of the data obtained through the acquisition system during the test sessions. This step was achieved by means of specific Matlab® scripts, which however, lacked cohesion and flexibility, therefore slowing down the elaboration process. This led to the necessity of creating a more comprehensive script, that could automatize and speed up the processing of the acquisition data while being flexible, intuitive and user-friendly. The Section 5.2 will deep-dive into the specifics of the new Post Processing program and detail possible future improvements.

5.1. Future structural updates to VeTyT

The first version of VeTyT test-rig was designed in 2019 [bicycle tyres development of a new test-rig to measure mechanical characteristics], thus it can be considered as a fairly new prototype. For this reason, it is step by step updated in its structure, changing or introducing elements, increasing its efficiency and accuracy.

5.1.1. New lateral translation system

After hundreds of dynamic tests performed through the VeTyT system, it was realised that an experimental campaign can be more efficient with a lateral translation system. The main reasons for this modification lie in an economical and practical point of view. When a dynamic test is in progress, small amount of residual rubber, coming from the tyre and the flat track belt wear, accumulated. Focusing on the flat track belt wear, with a full “Standard Dynamic Analysis” it is possible to perform at least 50 dynamic tests and, since the tyre is placed in a fixed position, this implies a big amount of wear in the same area, which is limited to a portion with at most twice as wide as the tyre. It was noticed that a rut was present in the belt, which can be considered as an obstacle

for the steering action, as well as a cause of uncertainty in the test results. Therefore, the current solution to this problem is changing the belt. However, this means having to buy a new belt, while the old one is only consumed on a limited portion, and to perform a long and complex changing procedure, which includes the displacement of the VeTyT structure and, consequently, the procedures of alignment. Hence, it is not optimal on both economical and practical points of view.

The lateral translation would allow the use of almost all the belt width and it would facilitate also the procedure of changing the belt of the flat track, when needed. Moreover, the procedures of alignment could be totally avoided.

The most widespread systems for the translation are the linear guideways. They allow the linear motion of a mass, with a very low coefficient of friction, by re-circulating rolling elements between a profiled rail and a bearing block. The mass to be displaced is clamped on the bearing block with bolts, which is able to slide on the rail. For this preliminary design the Hiwin® Company [69] was chosen as reference to present a prototype of linear guideway for our purpose.

The first step consisted in the presentation of all possible system configurations. Two possibilities were analysed: the lateral translation of the VeTyT structure and the lateral translation of the flat track.

The VeTyT system is in contact with the ground through 3 points, two at the front, represented by the supports of the Watt's linkage, and one at the rear, represented by the support of the universal (cardan) joint. In order to displace laterally the VeTyT structure it is necessary to displace laterally its point of contact with the ground. For this reason, it is necessary to use two linear guideways, one for the translation of the Watt's linkage supports and one for the translation of the universal (cardan) joint support. The use of two linear guideways allows a better distribution of the vertical load derived from the weight of the VeTyT's structure ($50 - 55\text{kg}$), including each mass connected to the structure (shaft, fork and wheel). Moreover, a single big bearing block is needed for the rear guideway, since a big support must be clamped on it, while two bearing blocks are needed for the front guideway on whom the two Watt's linkage supports are clamped.

This configuration presents problems related to the necessity to introduce rigid bars in the system: a first rigid bar that would connect the two bearing blocks at front, to avoid the relative displacement between the two Watt's linkage supports, and a second rigid bar that would connect the front and the rear systems, to avoid a yaw rotation of the VeTyT structure when it is displaced laterally. These bars would have to be long, which would cause the deflection at the midspan and consequently a modification of the system itself. For these important reasons this configuration was discarded.

The flat track system is a poly-V belt driven by an electric motor, through a pulley. Both the electric motor and the flat track are clamped to the ground, in particular the latter is clamped to a metal plate which is clamped to the ground. The lateral

translation of the flat track can be performed by simply translating the metal plate. In this case the vertical load over the linear guideway system is composed by the weight contributions of the VeTyT structure, the shaft, the fork, the wheel and the flat track system (*150 kg*). This configuration would only need very simple modifications to be carried out, with the only drawback being having to displace the electric motor according to the flat track displacement. For these reasons the preliminary design was done on this system.

The most effective way to design a new system is to do research on the market in order to find a compatible structure to be used for our purpose. The Hiwin® catalogue provides a big number of solutions as well as an online CAD configurator for linear guideways. The only design constraint is the big plate dimensions that must be coupled with the bearing blocks. The biggest block from the catalogue is *170 mm* wide and *295 mm* long, much smaller than the plate (*685 x 685 mm*). The use of one rail with one guide carriage is unfeasible, since the plate cannot be physically bolted on the guide carriage. It was considered, then, the possibility to use two rails, which facilitate the mounting procedure with the use of a single bed, with two bearing blocks each, to guarantee better distribution of the vertical load. This configuration allows to reduce the importance of the vertical load, allowing the selection of almost all the combinations of rail – blocks proposed by the manufacturer. It was considered, thus, an additional less relevant constraint on the height of the translation system. Therefore, the selected block belonged to the EG type [70], whose design, citing the official website, “offers a low profile, high load capacity, and high rigidity. It also features an equal load rating in all four directions and self-aligning capability to absorb installation – error, allowing for higher accuracies”.

- The most relevant features of the blocks and rails are summarized:
- Series: EG
- Block Type: W. Flange block to gain width (*100 mm*)
- Load type: C (heavy load), to be more conservative
- Blocks per rail: 2
- Number of rail: 2
- Rail length: *1370 mm*. More than double the width of the metal plate to allow the complete displacement of the flat track out of the VeTyT structure
- Rail height: *27.5mm*

Figure 5.1 shows the preliminary design of the lateral translation system.

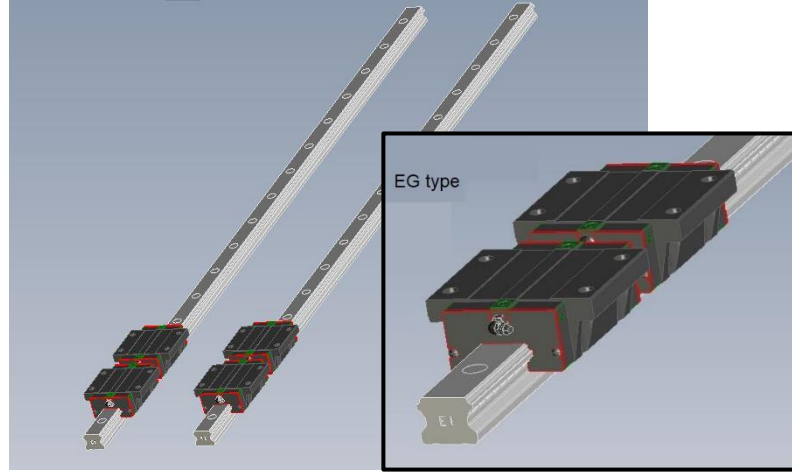


Figure 5.1: Lateral translation system preliminary design.

An important phase, after the selection of the suitable linear guideway, is the mounting procedure. It is highly recommended to follow a specific procedure in order to guarantee the required accuracy. The process is explained on the website as well as in the catalogue of the manufacturer [70].

The flat track must be fixed in position, and, for this reason, the guideway system is static (or under low-speed motion). The preliminary design includes the calculation of the static safety factor f_{sl} of the single bearing block (Eq. 5.1), a parameter that depends on environmental and operating condition.

$$f_{sl} = \frac{C_0}{P} \quad (5.1)$$

Where P is the calculated working load [kN] and C_0 is the static load rating [kN], intended as the static load of constant magnitude and direction resulting in a total permanent deformation of 0.0001 times the diameter of the rolling element and the raceway at the contact point subjected to the largest stress. If the amount of permanent deformation exceeds the limit, there is an obstacle to the smooth operation of the linear guideway.

The CAD configurator provides, together with the CAD of the linear guideway system, the C_0 factor (64.84 kN), while the P factor is given (about 1.50 kN), considering a certain service factor. The resultant static safety factor is 43.23, which represents a very large value that allows the system to resist impact loads, vibrations and high working loads ($f_{sl} > 7$). [70]

The last aspect to be covered is related to the flat track fixing to the ground. As the blocks can move with a low friction coefficient together with the flat track, then it is necessary to stop the blocks movement. It was considered the possibility to place

ground fixing elements sideway the blocks, pressing on the rail. The method prevents the blocks movements, however, it damages the upper part of the rail.

The method proposed in this analysis includes the design of a stopper that has the task of stopping the blocks, acting on its corner. It was conceived as a metal plate on which two bolted metal plates are welded in a vertical position, creating an edge. The base metal plate is used to have a space for clamping the stopper to the ground. The two vertical metal plates were conceived to be bolted in order to ensure a 90° corner. The edge, during its employment, is in contact with the block corner, undergoing lateral loads. Moreover, it also undergoes longitudinal forces due to the vibrations caused by the belt movement when performing a dynamic test. Since the upper part of the edge is involved in the action of these forces, two lateral reinforcements were added by welding to increase the resistance of the stopper. The dimensions are chosen in order to resist and to reach, in height, the blocks corner. The preliminary design of the stopper is presented in Figure 5.2.

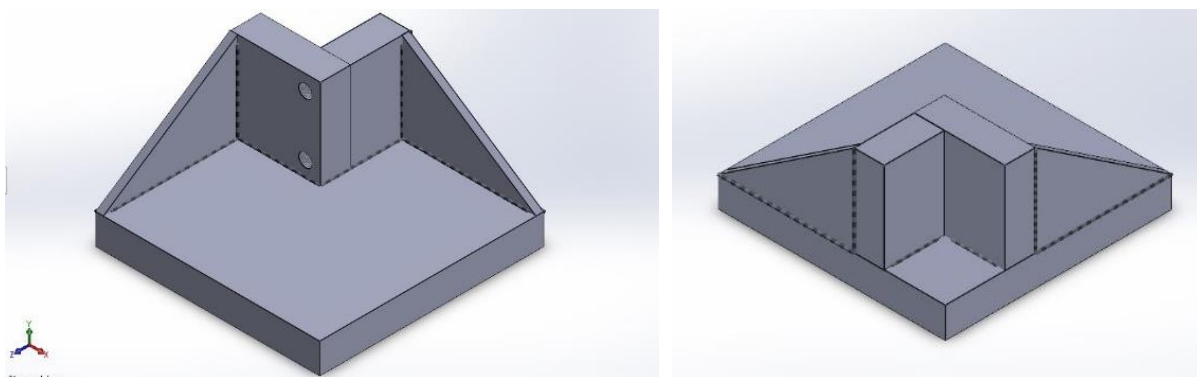


Figure 5.2: Stopper preliminary design

The preliminary design included the static analysis on the object performed through Solidworks®. The material selected and its properties are collected in Table 5.1.

Material	Ductile iron
Yield strength	$5.51 \cdot 10^8 N/m^2$
Young's modulus	$1.2 \cdot 10^{11} N/m^2$
Poisson's ratio	0.31
Density	$7100 kg/m^3$

Table 5.1: Stopper material and material properties.

The total mass of the stopper is 4.11 kg (the two bolts are excluded).

The bolts material, its dimensions and the material properties are shown in Table 5.2.

Number of bolts	2
Material	Steel
Young's modulus	$2.1 \cdot 10^{11} \text{ N/m}^2$
Bolt resistance	$6.20 \cdot 10^8 \text{ N/m}^2$
Poisson's ratio	0.28
Preload (axial)	5 N
Head and nut diameters	13.6398 mm
Nominal diameter	9.0932 mm

Table 5.2: Bolts properties.

The load condition considered is the worst possible scenario with two distributed forces, in longitudinal and lateral directions, acting on a portion of the stopper corner, i.e., the one in contact with the bearing block. Moreover, the value is set equal, for both the directions, to 1000 N in order to take into account a safety factor on the maximum lateral force measured during the entire testing campaign (600 N).

The stopper is considered clamped to the ground, so a FEM analysis was performed. The von Mises stress results are reported in Figure 5.4.

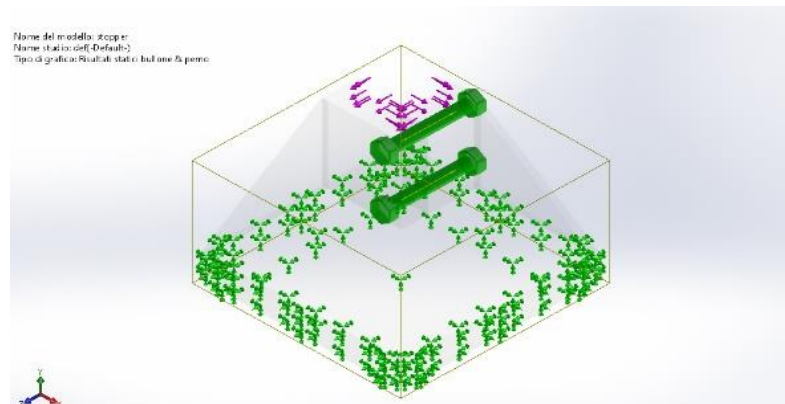


Figure 5.3: Interactions: distributed loads, bolts, external supports.

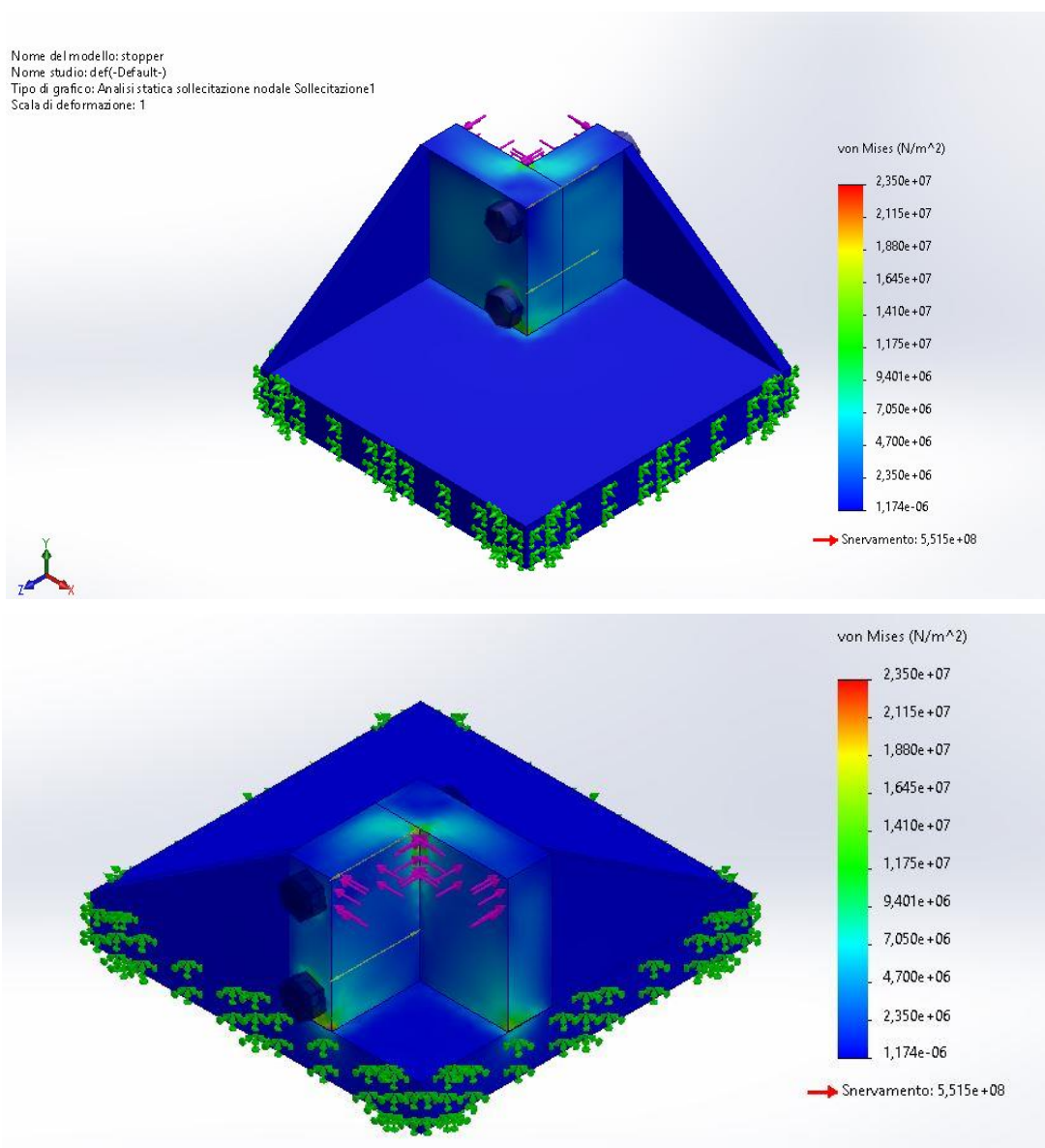


Figure 5.4: Von Mises stress analysis. At top, the frontal part of the stopper; at bottom, the rear part of the stopper.

Looking at Figure 5.4 it is possible to notice that the most stressed parts are the ones corresponding to the bolts and the ones corresponding to the welds, thus where junctions are present.

It is important to consider that the maximum von Mises ($2.35 \cdot 10^7 \text{ N/m}^2$), is much lower than the yield strength of the material, allowing a safety factor of 23.37. Moreover, thanks to the software, it is possible to perform a rapid fatigue assessment, which concluded that “the solicitation seems to be so low that fatigue can be not considered as a problem”. The bolts safety was checked and confirmed by the software itself.

The final configuration, linear guideline and stopper, can be appreciated in Figure 5.5.

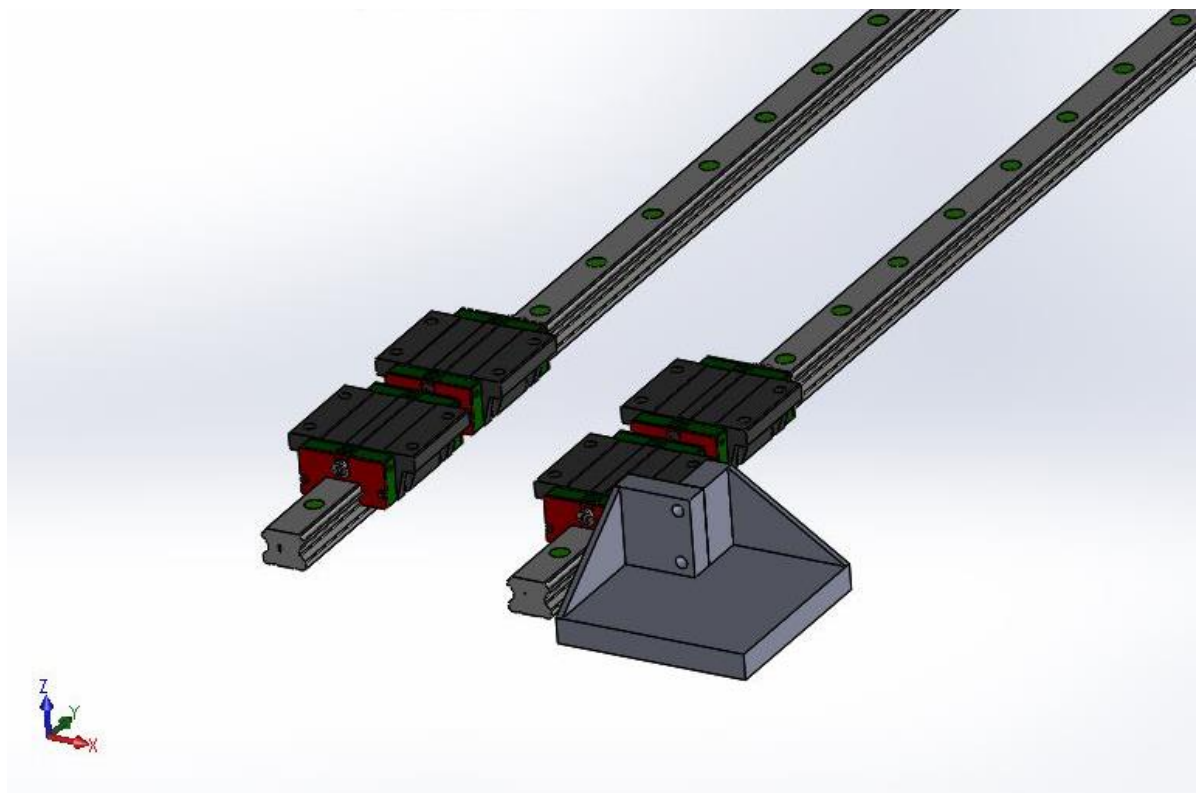


Figure 5.5: Linear guidelines with the stopper positioned to avoid the movement of the block.

5.1.2. Modified “height” calibration system

The assembly of the load cell that measures the vertical load is characterized by a rigid connection with the chassis in the upper part, through a system composed by a threaded bar and nuts, while, in the lower part, the spherical tip of the load cell is in contact with the steering shaft (Figure 5.6). The upper connection has a second purpose, in fact it allows the “height” calibration. Acting on the nuts, it is possible to regulate the position of the VeTyT structure in terms of changing the position of its longitudinal and vertical axes. This procedure becomes relevant when different wheels and rims are mounted, since, for example, an increase in the wheel diameter leads to an upward pitch rotation of the VeTyT structure. The effect of this rotation is a misalignment of the chassis with respect to the flat track belt.



Figure 5.6: The assembly of the load cell that measures the vertical load.

The stiffening of the chassis with steel cables and reinforcements led to a reduced space in the upper area of the VeTyT, limiting the possibility to screw the nuts of the threaded bar and increasing the set-up time. The necessity to eliminate this heavy process assumes particular relevance. For this reason, in this subsection, modified systems of “height” calibration are analysed.

The first idea was to use a jack, a mechanical or hydraulic device whose main task is lifting heavy equipment. This device would fully replace the threaded bar – nuts system, maintaining the same tasks and connections. Moreover, it would be rigidly connected to the chassis in the upper part and to the spherical joint in the lower part. The jack types that could be used to implement this solution are both the scissor jack and the bottle jack. The first performs the lifting action through the screwing of a screw

tread, the second performs the same action thanks to the hydraulic pressure provided by a pump. However, the solution required should be ready-to-use and the market does not have a jack suitable to the small volume available. It would be necessary to design, produce and test a VeTyT-specific jack.

The simplest solution consists in modifying the current system. The treaded bar could be replaced by a turnbuckle-style connecting rod: similar to turnbuckles, these rods have right-hand threads on one end and left-hand threads on the other so you can make a linkage that adjusts for tension. Rods have a hex-shaped body so that you can adjust them with a wrench. The working principle is shown in Figure 5.7.

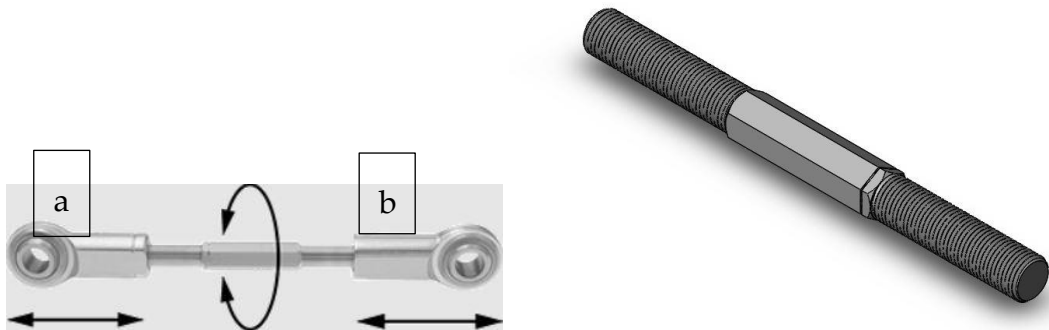


Figure 5.7: On the left, the turnbuckle-style connecting rods working principle. On the right, the turnbuckle-style connecting rods CAD.

The two elements *a* and *b* in Figure 5.7 (left) could be screwed onto the two free ends of the rod. Then, while keeping them from rotating around their axle, if the central rod is screwed, the two elements can be displaced axially, moving away or towards each other. In this way it is possible to perform the “height” calibration. The adaptation to our system would be done by first inserting one nut in each side of the rod, then by screwing one side to the spherical joint and the other side to the upper part of the chassis. The two nuts would be used for locking purposes after the calibration phase. This system would allow higher dimensional flexibility compared to the jack, while being a quite simple mechanism.

5.2. Software Development

The output of any test performed with the VeTyT test-rig is a DAT file that contains the acquired time signals of the four load cells and the encoder in five different

channels. This file is created through LabView, a software that allows the operator to read and acquire the signals. However, the acquired data is raw and cannot be directly used to analyse the tests: they need to be filtered and elaborated, to obtain the wanted physical quantities, such as lateral force and self-aligning torque.

Therefore, a Matlab® program named ‘postProcessing.m’ has been developed to extract the raw data from the DAT file and automatically give back the elaborated data and the necessary plots for the report. This section will describe the functionalities of the Post Processing program, explaining its structure and how it works, as well as future possible improvements. The code for the software can be found in the Appendix B.

5.2.1. Starting point

The previous testing campaigns also used Matlab® codes to elaborate and process the raw data files. However, each type of analysis (e.g. camber variation, load variation, cornering stiffness, etc.) had its own script which also was specific to a particular test. They lacked flexibility, meaning that when, for example, a new test configuration was to be processed, the operator had to change many variables to adapt it from one set to another. Moreover, having the information spread across so many different scripts made the data elaboration process much less intuitive and user-friendly, especially for someone that is not used to working with Matlab®.

For these reasons, the idea behind the development of a Post Processing software was to take the existing processing methods, refine them and put them together in a single main script that could process the data and perform all the needed analyses, while being flexible, intuitive and user-friendly.

5.2.2. Post processing

5.2.2.1. Software inputs

The software is organized in one main script called ‘postProcessing.m’. However, for it to work, the workspace must not only contain the main script, but also two important folders:

- ‘*Input*’ folder: it must contain all the DAT files that are to be processed through the software, i.e., all the acquisition files for the test that is going to be analysed and the zero file that corresponds to the load cell reset of that test session.
- ‘*Toolbox*’ folder: it contains all the additional scripts and functions that are required for the main script to work smoothly. The full content of the Toolbox folder can be seen in Figure 5.8.

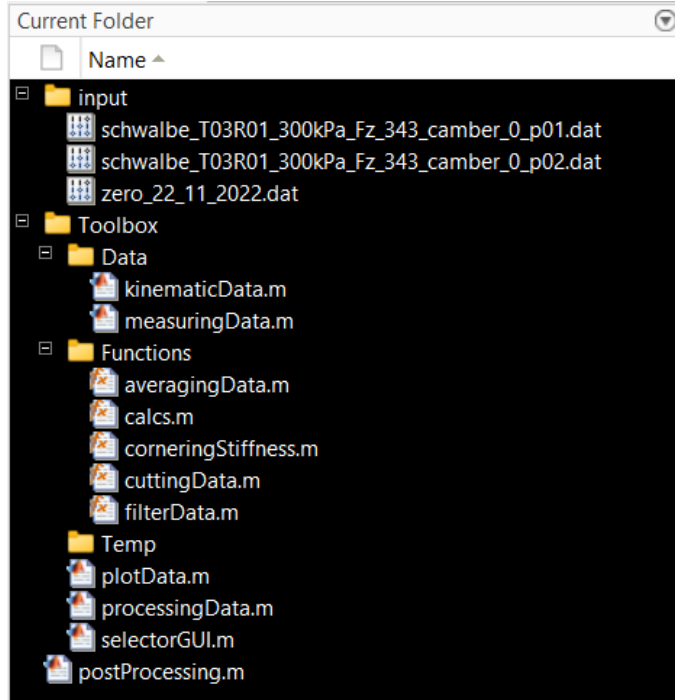


Figure 5.8: Workspace content.

For the script to perform the analysis, it is necessary to specify the tyre that is going to be analysed and which of the testing parameters must be processed. The following lines of code are directly taken from the ‘inputs’ section of the Post Processing program.

```

measuringData                                % VeTyT measurement data set
kinematicData                                 % VeTyT kinematics data set

tireBrand          = 'scalato';                % Tyre brand
tireCode           = 'T05';                     % Tyre code
rimCode            = 'R01';                     % Rim code
slope              = 1;                        % Slip angle signal slope

% IMPORTANT: 0 must always be the first element in the camberval vector
cambervals        = [0 -5 5];                  % Tested camber angle [°]
loadVals          = [343 404 488];             % Tested vertical load [N]
pVals              = 400;                      % Tested pressure [kPa]
dataTest.alphacut = 1;                        % Cut-off slip angle [°]
datavetyt.m_wheel = 12.73;                    % Mass axis+fork+wheel [kg]
zero               = load(['zero_22_11_2022.dat']); % zero file

```

By providing this information, the program is able to choose from the Input folder all the DAT files that correspond to the specified tyre and parameter combinations. It can process all the combinations of pressure, load and camber tested at once, provided they are inserted in the correct vectors (pVals, loadVals and camberVals).

5.2.2.2. Software Outputs

The main body of the Post Processing software can be divided into two core parts: Data Processing and Data Visualization. The first one elaborates the raw data contained into the DAT file by filtering and performing the calculations needed to obtain the wanted physical quantities, while the latter uses the elaborated data to produce the plots and the tables that are needed to fill in the official reports of the "Standard Dynamic Analysis".

5.2.2.3. Data Processing

To get to the clean data from the raw DAT file, the acquisition signals must undergo a series of passages.

Firstly, the operator must choose which tests to take into consideration. This is because, even if the tyre and tested conditions were already specified, each parameter combination was tested at least twice, which means that for each parameter combination there are at least two DAT files, whose name will end in 'p01' or 'p02' (if only two repetitions). The tests were repeated to have a back-up acquisition in case one of the two contained errors of any kind.

Therefore, to be able to properly choose an acquisition that contains a clean test, without errors or strange behaviours, an overlapped preview of the F_w and slip angle signals for both test is displayed (Figure 5.9). The operator is then offered two options: to analyse a single test between the available ones or to perform the analysis on a time average of the displayed tests (Figure 5.10a). The first one leads to a simple menu that allows to choose the wanted test (Figure 5.10.b), while the latter leads to a multiple-choice menu in which the operator must select between whom of the available options is the average going to be calculated (Figure 5.10.c).

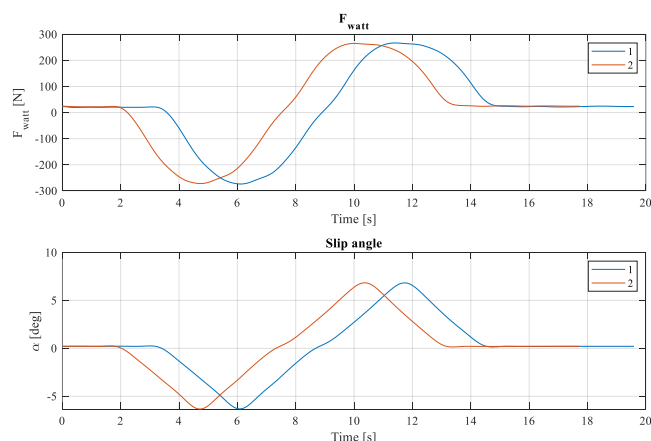


Figure 5.9: F_w and slip angle versus time plots, for both repetition of the test at 400kPa, camber 0° and 488N for the SCH-T03 tyre.

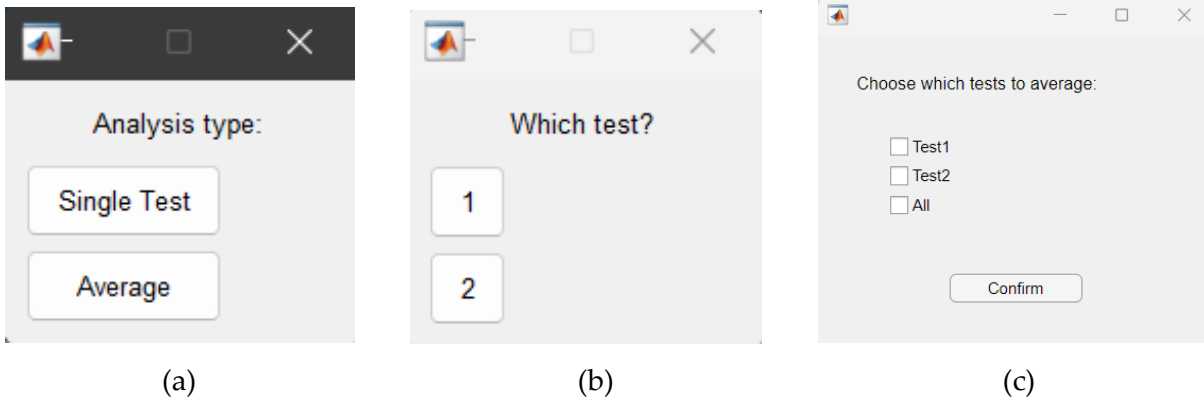


Figure 5.10: Menu interfaces of the Post Processing software for the choice of the analysis type (a), of the single test to analyse (b), of the tests to be averaged (c).

Once the wanted raw data files are selected, each of the tested combination is singularly processed through a for-loop that elaborated the data through the following steps:

- *Filtering*: through the function ‘filterData.m’, the raw data undergoes a first cleaning, by being subtracted the values contained in the zero file. Also, the time vectors are generated thanks to the sampling frequency ($F_{samp} = 1612.9\text{ Hz}$). Then the data passes through a non-causal, zero-phase, low-pass filter (Matlab® function ‘idfilt’) that uses a cut-off frequency that can be imposed by the operator by modifying its value in the ‘measuringData.m’ dataset.
- *Cutting*: the function ‘cuttingData.m’ trims the slip angle vector so that it is only reduced to the part in which we want to perform the test. In fact, the part of the slip angle motion law, imposed by the linear actuator, that is taken into consideration is the section in which the wheel steers from one maximum slip angle to the other, the extremities are not taken into account, as shown in Figure 5.11. The other acquired signals are cut accordingly, so that they all have the same length.

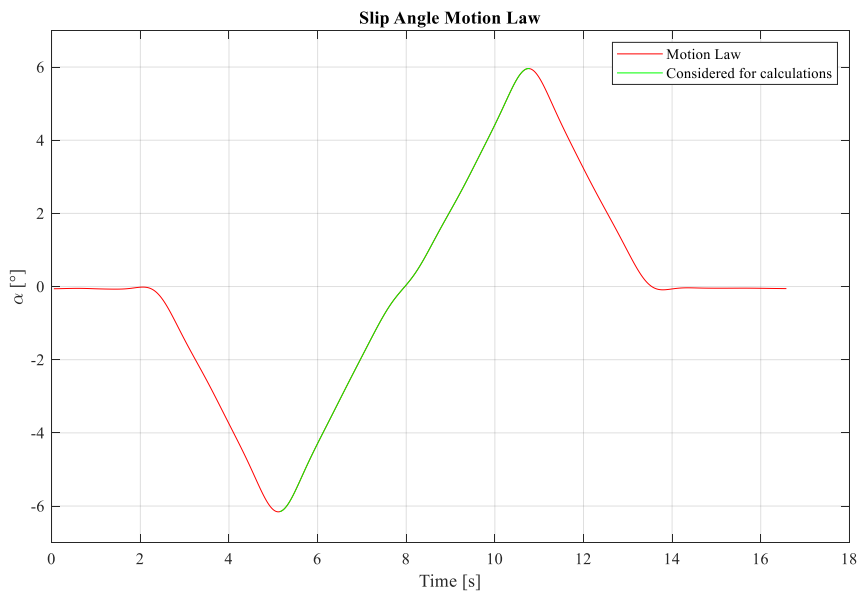


Figure 5.11: Slip angle signal motion law: in red is the whole acquired signal, in green is the part taken into consideration for the tests.

- *Averaging*: if the analysis type chosen is ‘average’, the selected tests will be averaged between each other through the function ‘averagingData.m’
- *Calculations*: thanks to the ‘calcs.m’ function, the acquired data is elaborated into the desired physical quantities (F_y , M_z), applying eventual corrections.
- *Cornering stiffness*: the function ‘corneringStiffness.m’ reads the elaborated data and calculates the cornering stiffness as the slope of the polynomial fitting of the F_y versus slip angle data. The interval of the characteristic curve to be considered for the cornering stiffness calculation is defined by the input variable `dataTest.alphaCut`, which indicates the absolute value of the limit slip angles for the considered interval.

At the end of the for-loop, all the elaborated data are stored into a struct that contains as many fields as tested combinations analysed. Every field consists in a sub-struct that contains all the acquired and calculated quantities, properly filtered, cut and elaborated.

The program also asks the operator whether he wants to save the struct, so that it can be used to skip the whole elaboration process and go directly to the visualization block, if needed.

5.2.2.4. Visualization

Once the raw data has been processed and elaborated, it is ready to be visualised. The software offers the following types of analysis:

- *Varying load*: plots the characteristic curves at constant camber, constant pressure and different vertical load values.
- *Varying camber*: plots the characteristic curves at constant vertical load, constant pressure and different vertical camber values.
- *Cornering stiffness*: generates a table that reports all the cornering stiffness values found for different vertical loads and camber values, at constant pressure.

The type of analysis can be chosen through a check-box menu, that allows to select more than one type of analysis and is also provided with a 'All' button in case the operator wanted to perform all the analysis types at once (Figure 5.12).

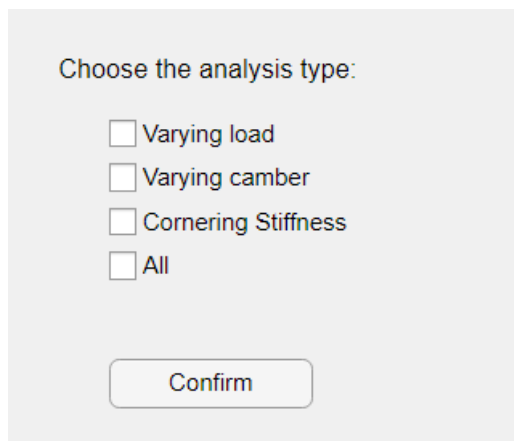


Figure 5.12: Checkbox menu for the analysis type choice.

The software asks the operator whether he wants to save the generated plots; if this option is selected, the program will save the files into a 'Plots' folder, which will contain a 'fig' folder, housing all the plots saved in .fig format, and a 'emf' folder, with all the plots saved in .emf format.

The .fig format is the standard Matlab® figure format: if a Matlab® plot is saved in fig format, it can be accessed at any moment and modified as if it was just generated. The .emf format, instead, allows to save the plot into vectorial images, that can be used for the official reports for a better image quality.

5.2.3. Report Generator

Writing the official reports for the 'Standard Dynamic Analysis' (see Section 3.2 for reference) can be a lengthy process. All of the tables have to be filled in manually and all of the plots have to be placed in the document by the operator, which make the creation of the reports very time-consuming. Hence, the idea of automatising the

report generation process was thought, as a code part to add to the existing Post Processing software.

From the preliminary research study, it was clear that the best way to implement such code would lie in using the ActionX commands. From the official Matlab® documentation, the command “`c = actxserver(progid)` creates a local OLE Automation server, where `progid` is the programmatic identifier (ProgID) of an OLE-compliant COM server. The function returns a handle to the default interface of the server” [71]. Imposing ‘word’ as the `progid` variable, it is possible to directly control and modify Word documents from Matlab®.

Since most of the information that must be written in the report is elaborated or directly generated in the Post Processing script, it is of rapid access and can be easily imported into Word by using Word’s methods, controlled by ActionX.

Therefore the ‘`reportGenerator.m`’ script was written. After having loaded the struct containing the full analysis of the tyre whose report is going to be generates, the script is able to open a report template and to fil it with text, graphs and tables, formatted following the standard report format. It then asks the operator whether they want to save the newly generated file and, finally, if they want to close it. The code for this script can be found in Appendix B.

This will drastically cut the times of writing of the report, since the base formatting is directly automatised, leaving the operator to only add their comments to the results and some more complex tables, which could also lead to more insightful conclusions, since the operator will have more time to dedicate to the analysis.

A possible development of this script could consist in integrating it in the main Post Processing script as a toggleable option, in order to be able to automatically generate the report just after having performed the analysis.

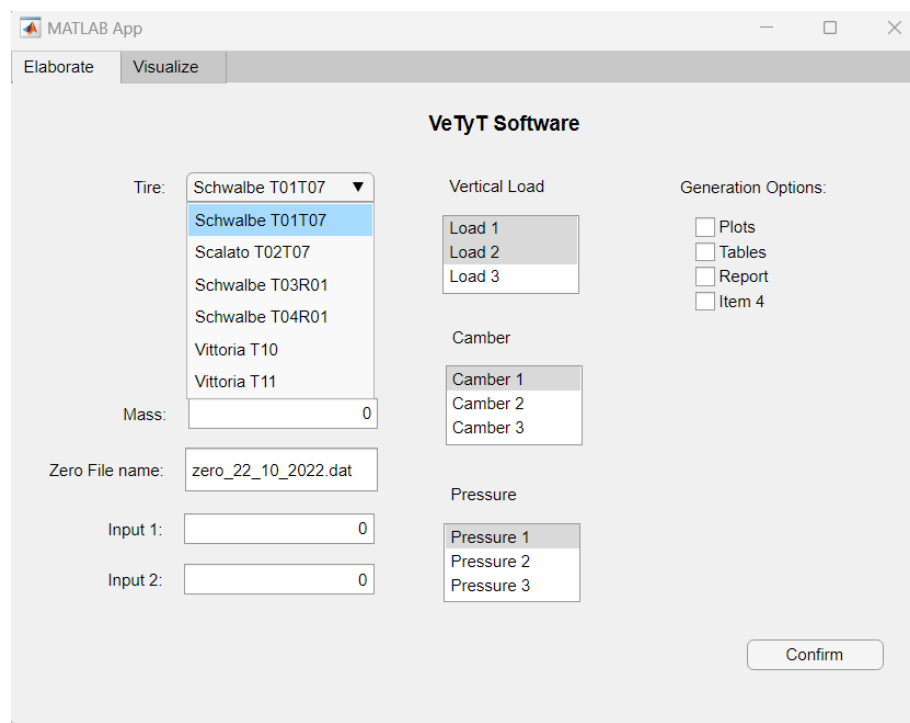
5.2.4. Future software developments

The Post Processing software is a very useful tool that allows a faster elaboration of the tested data, thanks to the automatization of the processing and displaying of the data. However, there is a key improvement, whose bases have already been placed, that is yet to be fully implemented: the user interface.

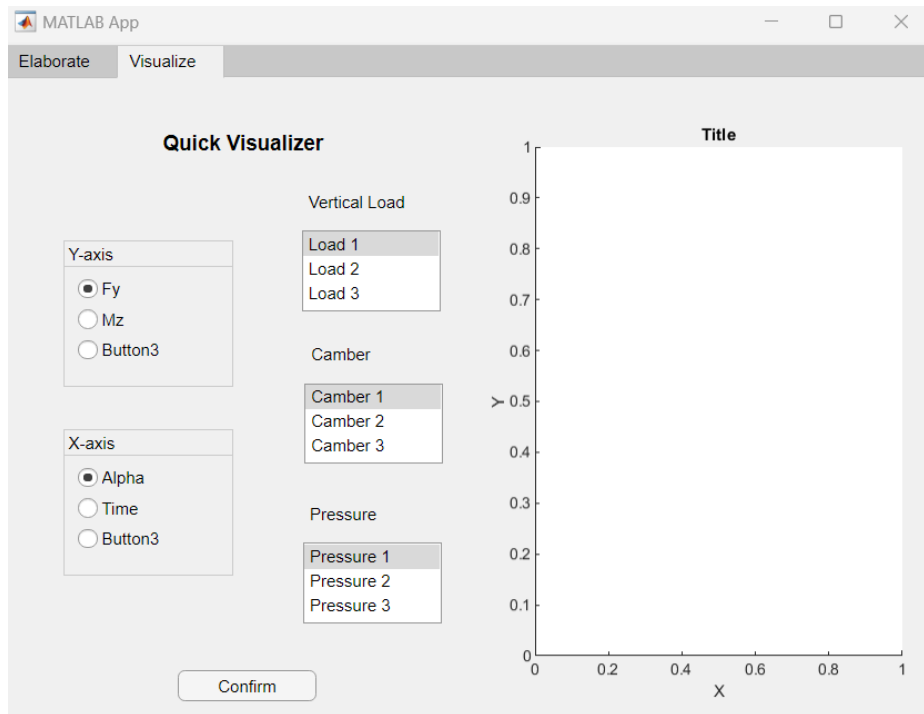
5.2.4.1. Guided User Interface (GUI)

Even if a great effort was made to make the post processing program as user-friendly as possible, it is still a Matlab® script and therefore may not be suitable for everyone, especially for an operator that has little to no Matlab® experience. For this reason, one of the next steps in the development of the Post Processing software is transforming it

from a script into a real application with a simple and intuitive guided user interface (GUI). This process is simplified by the Matlab® App Designer, which allows the creation of applications in the Matlab® environment. An initial draft of how the Post Processing application could look like has been made. The basic idea is to create two main tabs. The first one would be dedicated to setting the characteristics of the data processing, such as the zero file, the test parameters, and what output must be generated (Figure 6.a). The second tab would be focused on the instantaneous visualization of plots, after having processed the data in the first tab (Figure 6.b). The idea is to be able to rapidly check the trends of the tested quantity, even few minutes after having performed the test.



(a)



(b)

Figure 5.13: Drafts of dashboards for the Post Processing application, for the data elaboration (a) and visualization (b).

6 Conclusion and future developments

The aim of this thesis was to show what kind of analysis could be performed with the "VeTyT" test-rig, which is located at the "Laboratory for Safety of Transport" (La.S.T.) of Politecnico di Milano, and to study how the testing process and the "VeTyT" rest rig could be improved. This device was specifically designed for the measurement of bicycle tyre properties and characteristic curves in order to increase the knowledge and data about the behaviour of bicycle tyres. Moreover, it presents high flexibility since it can accommodate different tyres, from road cycling tyres to cargo bike and city e-bike tyres, and more. Also, the rim size and rim type are flexible parameters: the size can vary from 16" to 29", with a rigid or spoked rim. The test-rig is designed to be placed both on a rotating drum and on a flat track system, with the second being the one that was used for this campaign. The modifications made to the test bench during the years were aimed at decreasing the uncertainty of measurement, increasing the technological level as well as the number of technical documents aimed at instructions for use. In November 2022 the "VeTyT" was officially certified, providing this device with a recognised seal of quality.

The thesis work consisted in dynamic and static experimental campaigns, whose main target was to study the influence of different parameters, such as inflation pressure, camber angle and vertical load, on tyre properties and characteristic curves. The high number of tested tyres allowed also a comparative analysis in order to have a deep understanding of the differences between tyres with the same functionality, while changing the tyre manufacturer, the tyre width or the tyre compound, and between tyres with different functionality. Finally, more attention was paid to the development of a software able to read and elaborate the raw data acquired from the measurements, providing the required analysis in terms of plots and tyre properties. Some suggestions for future developments of the software as well as structural modifications are given.

Chapter 3 provided an extract of the many possibilities in the study of bicycle tyres offered by performing dynamic tests with the "VeTyT" test-rig. After having recalled the fundamental concepts known from literature about road vehicles' tyres in Section 3.1, the "Standard Dynamic Analysis" is introduced in Section 3.2. It consists in the analysis of the characteristic curves for lateral force and self-aligning torque for all the tested tyres in various tyre conditions, that also forms part of the official test reports that are given to the customers that requested the test on the tyre. This is a fundamental analysis to understand the general performance of the tyre, and see how it behaves

specifically when vertical load, inflation pressure and camber angle are varied. This thesis reports the examples of two of the tested tyres (a cargo bike tyre and a e-bike tyre). From the study of the lateral force curves, it is also possible to derive the cornering stiffness, a characteristic property of the tyre that influences the handling behaviour of bicycle and consequently its stability.

Section 3.3 showed some characteristic curves obtained from the "Standard Dynamic Analysis" that presented unusual trends. Possible causes for these behaviours were investigated and a comparison was made with the curves obtained on a second testing session under the same conditions. The main reason for the strange behaviours was found to be in the wear of the flat track belt. For the CST-T02, a manufacturing defect was also found.

The tyres analysed in this testing campaign could be divided into three groups based on their function: cargo bike tyres, e-bike tyres and road racing bike tyres. Section 3.4 proposed two studies on the comparison of the characteristic curves based on these tyre sets. Firstly, different tyres belonging to the same functionality sets were compared to appreciate how different design philosophies provide different behaviours, even when the final function is the same. Secondly, a qualitative comparison between the three functionality groups was performed, by observing their characteristic curves tested in similar conditions. This highlighted how differences in design and manufacturing that exist between different types of tyres are translated into their physical behaviour and therefore into their performance.

Regarding the static experimental campaign, in Chapter 4, some important results are obtained and discussed in-depth.

The Schwalbe® company presented a completely renewed version of the SCH-T04, the SCH-T03. Conceived as tyres for e-bikes, it is possible to exploit the additional electric power for covering higher distances. From this point of view, it is important to make a comparison between their vertical stiffnesses (Section 4.1), as it is a parameter that can affect the comfort of the rider and the tyre performances. The pivot element that characterizes the vertical stiffness is the tyre drop, which is the measure of the vertical deformation of the tyre under the action of a vertical load. Varying the vertical load, it is possible to obtain the vertical stiffness of the tyre for both the considered tyres. It was noticed that the vertical stiffness exhibits a precise behaviour when changing the inflation pressure, in fact, the increase in pressure led to an increase of the vertical stiffness that is less than linear. This effect is mainly explained by the increase in the air stiffness contribution in the lateral stiffness. Moreover, the new SCH-T04 had lower vertical stiffness for the same values of pressure with respect to the older version, guaranteeing, by hypothesis, lower discomfort and higher rolling resistance. This can be considered a positive effect since the rider can ride longer distances with higher comfort, while the rolling resistance can be compensated by the electric motor.

Another study was conducted on the tyre's contact patch (Section 4.2), with the purpose of confirming the contact patch's well-known behaviour under different vertical load and inflation pressure conditions. The chosen tyres were two Vittoria Road Racing / Competition Corsa N.est with two different width (26 -28 mm). This choice aims also at understanding how the tyre width affects the contact patch area. For both tyres, when increasing the vertical load, the contact patch area increases, while increasing the inflation pressure the contact patch area decreases. Comparing the two tyres while considering a certain level of uncertainty present in the measurements, it was stated that the contact patch area does not change with the increase of the tyre width. A more in-depth study on the shape of the contact patch together with the choice of tyres with higher difference in width could lead to even more evident results.

In Section 4.3 the tyre lateral stiffness was estimated considering the two Vittoria tyres already seen in the contact patch analysis. This important parameter was measured with a precise procedure which brought to the following results: for the lowest vertical load tested, the lateral stiffness increases with the inflation pressure; while for increasing values of vertical load the behaviour changes, in fact the lateral stiffness reaches a saturation point at the intermediate value of inflation pressure and then decreases. Moreover, the wider tyre has lower lateral stiffness, this effect can be caused by a possible change in the tyre cross section.

If the information about the cornering stiffnesses is added to the measured lateral stiffnesses, it is possible to carry out the analysis of an important parameter that defines the dynamics of the tyre: the relaxation length (Section 4.4). The wider Vittoria tyre has higher relaxation length values for each combination of vertical load and inflation pressure because it has higher cornering stiffness and lower lateral stiffness with respect to the narrower tyre. This effect results in a slower tyre response for the wider tyre, which means that the lateral force needs more time for reaching the steady state value after a change in the side slip angle. The relaxation length of the two tyres displays a peculiar behaviour when varying the inflation pressure and the vertical load: for the lowest value of inflation pressure, the relaxation length value is the highest; for the intermediate pressure, for lower values of vertical load, the relaxation length is higher than the one at highest pressure, while it is lower than the one at highest pressure for higher values of vertical loads.

After reporting the main improvements and results of this thesis work, some future structural updates are analysed (Section 5.1). They consist in the presentation of a lateral translation system and a modified "height calibration" system. Both aim to make the "VeTyT" system more efficient, avoiding hard procedures and reducing the economical waste. The linear guideway system was considered for translating lateral the flat track system by the specific use of two guideways, each with two bearing blocks. This preliminary design analysis includes also the definition of a stopper, used to block the lateral movement of the flat track system on the linear guideways. The

analysis ends up with a static safety factor for the blocks equal to 43.23 and a static safety factor for the stopper of 23.37, both ensuring a conservative service factor. For the “height calibration” system it is presented, as solution, a modification of the existing system. The tread that connects the vertical load measuring load cell to the upper part of the chassis is replaced by a turnbuckle-style connecting rod. This linkage is adjustable in terms of relative distance, by screwing the central rod. In this way the VeTyT structure realigns with the flat track system.

To be able to process and visualise the data collected from the tests, while keeping it an intuitive and user-friendly process, a Matlab® script called “Post Processing” was developed (Section 5.2). It takes as input the DAT acquisition files and automatically elaborates them, by filtering the data, cutting it, and performing all the calculations needed to obtain the desired quantities for the analysis as output. All the elaborated data is stored into a struct that can be saved. After that, the program offers three different types of the visualization of the data: load variation, camber variation and cornering stiffness. The program then generates the plots and the tables required by the operator and saves them in formats that are ready to be used in the official reports for the “Standard Dynamic Analysis”. Future improvements for the Post Processing program could be the implementation of an automatic report generator and the development of a Guided User Interface in the Matlab® App Designer environment.

Bibliography

- [1] L. B. F. N. S. Ferretto, "Pathways to active mobility planning," *Research in Transportation Economic*, 2021.
- [2] UNFCCC, "The Paris Agreement," [Online]. Available: <https://unfccc.int/process-and-meetings/the-paris-agreement#:~:text=Its%20overarching%20goal%20is%20to,above%20pre%2Dindustrial%20levels.%E2%80%9Dsc>. [Accessed 2023].
- [3] R. R. F. & B. M. Scarinci, "Needed reduction in mobility energy consumption to meet the goal of a 2000-watt society," *Transportation Research Part A: Policy and Practice*, 2017.
- [4] "CO2 emissions from cars: facts and figures (infographics)," the European Parliament, 2023. [Online]. Available: <https://www.europarl.europa.eu/news/en/headlines/society/20190313STO31218/co2-emissions-from-cars-facts-and-figures-infographics>. [Accessed 2023].
- [5] A. C. K. D. D. M. Stefan Gössling, "The Social Cost of Automobility, Cycling and Walking in the European Union," *Ecological Economics*, vol. 158, pp. 65-74, 2019.
- [6] B. W. A. & V. G. Petzer, "The legal street: a scarcity approach to urban open space in mobility transitions," *Urban Transformations*, 2021.
- [7] J. K. Bhanu Prakash Sandaka, "Alternative vehicular fuels for environmental decarbonization: A critical review of challenges in using electricity, hydrogen, and biofuels as a sustainable vehicular fuel," *Chemical Engineering Journal Advances*, vol. 14, 2023.
- [8] "Fossil fuel cars make 'hundreds of times' more waste than electric cars," the Guardian, 2021. [Online]. Available: <https://www.theguardian.com/business/2021/mar/01/fossil-fuel-cars-make-hundreds-of-times-more-waste-than-electric-cars>. [Accessed 2023].
- [9] L. R. R., "Soft Mobility and Urban Transformation," *TeMA - Journal of Land Use, Mobility and Environment*, vol. 2, 2010.
- [10] "worldometer," [Online]. Available: <https://www.worldometers.info/bicycles/>.
- [11] "The benefits of cycling," ECF, 2018.
- [12] "Cycle more Often 2 cool down the planet !".ECF.
- [13] B. R. T. M. C. E. K. D. I. K. T. G. Pope CA 3rd, "Lung cancer, cardiopulmonary mortality, and long-term exposure to fine particulate air pollution," *JAMA*, vol. 287, no. 9, pp. 1132-1141, 2002.
- [14] I. N. A. M. S. S. Guure CB, "Impact of Physical Activity on Cognitive Decline, Dementia, and Its Subtypes: Meta-Analysis of Prospective Studies," *BioMed Research International*, 2017.
- [15] R. & T. R. Goodman, "The decline of everyday walking in the UK: Explanations and policy implications," *Sustainable Transport*, 2003.

- [16] L. Fransen, "The promise of cycling for a reduction in car mobility in the Netherlands," 2022.
- [17] "Traffic safety basic facts on cyclists," *European Commission*, p. 24, 2018.
- [18] J. P. a. R. Buehler, "Cycling towards a more sustainable transport future," *Transport Reviews*, vol. 37, no. 6, pp. 689-694, 2017.
- [19] P. M. R. B. M. R. S. R. K. R. Miller M, " Measurement and Modeling of a Cargo Bicycle Tire for Vehicle Dynamics Simulation," *Applied Sciences*, 2013.
- [20] R. B. a. J. Pucher, "Covid-19 Impacts on Cycling, 2019-2020," *Transport*, vol. 41, no. 4, pp. 393-400, 2021.
- [21] J. C. H. B. Y. S. Y. C. a. H. Y. Wen-Long Shang, "Impacts of covid-19 pandemic on user behaviors and environmental benefits of bike sharing. A big-data analysis," *Applied Energy*, 2021.
- [22] N. M. C. a. J. P. Gianantonio Magnani, "On-road measurements of high speed bicycle shimmy, and comparison to structural resonance," pp. 400-405, 2013.
- [23] A. C. G. M. Nicolò Tomiati, "A nonlinear model of bicycle shimmy," *Vehicle System Dynamics*, vol. 57, pp. 1-21, 2018.
- [24] G. M. a. M. M. Nicolò Tomiati, "An experimental investigation of the bicycle motion during a hands-on shimmy," *Vehicle System Dynamics*, vol. 59, no. 9, pp. 1443-1459, 2021.
- [25] V. L. Uslenghi L, "Indoor testing of cycling tyres and quality assurance of Vetyt test rig," 2021.
- [26] "CORSA N.EXT," Vittoria S.p.a., [Online]. Available: <https://www.vittoria.com/us/en/corsa-next>. [Accessed 2023].
- [27] "BIG BEN PLUS," Schwalbe, [Online]. Available: <https://www.schwalbe.com/en/tour-reader/big-ben-plus>. [Accessed 2023].
- [28] "PRO BROOKLYN | C1996," CST, [Online]. Available: <https://csttires.eu/brooklyn-pro/>.
- [29] "ENERGIZER PLUS," Schwalbe, [Online]. Available: <https://www.schwalbe.com/en/tour-reader/energizer-plus>. [Accessed 2023].
- [30] "Calameo: Schwalbe catalogue 2017," Shwalbe, [Online]. Available: <https://www.calameo.com/read/002916135162e94b146f8>.
- [31] "MONDANO," Scalato, [Online]. Available: <https://scalato.com/mondano/>. [Accessed 2023].
- [32] V. & D. A. & G. E. & T. L. & M. M. Cossalter, "Identification of the characteristics of motorcycle and scooter tyres in the presence of large variations in inflation pressure," *Vehicle System Dynamics*, 2014.
- [33] T. M. C. G. e. a. Doria A, "Identification of the mechanical properties of bicycle tyres fro modelling of bicycle dynamics," *Veh Syst Dyn.*, vol. 51, no. 3, pp. 405-420, 2013.
- [34] A. & T. L. & J. T. & P. T. & P. M. & A. S. & C. L. Doria, "Identification of the Mechanical Properties of Tires for Wheelchair Simulation," *The Open Mechanical Engineering Journal*, vol. 10, pp. 183-200, 2016.
- [35] A. E. Dressel, "Measuring and Modeling the Mechanical Properties of Bicycle Tires," 2013.
- [36] H. S. J. e. a. Maier O, "Vertical and longitudinal characteristics of a bicycle tire," *Tire Sci Technol*, vol. 46, no. 3, p. 153–173, 2018.

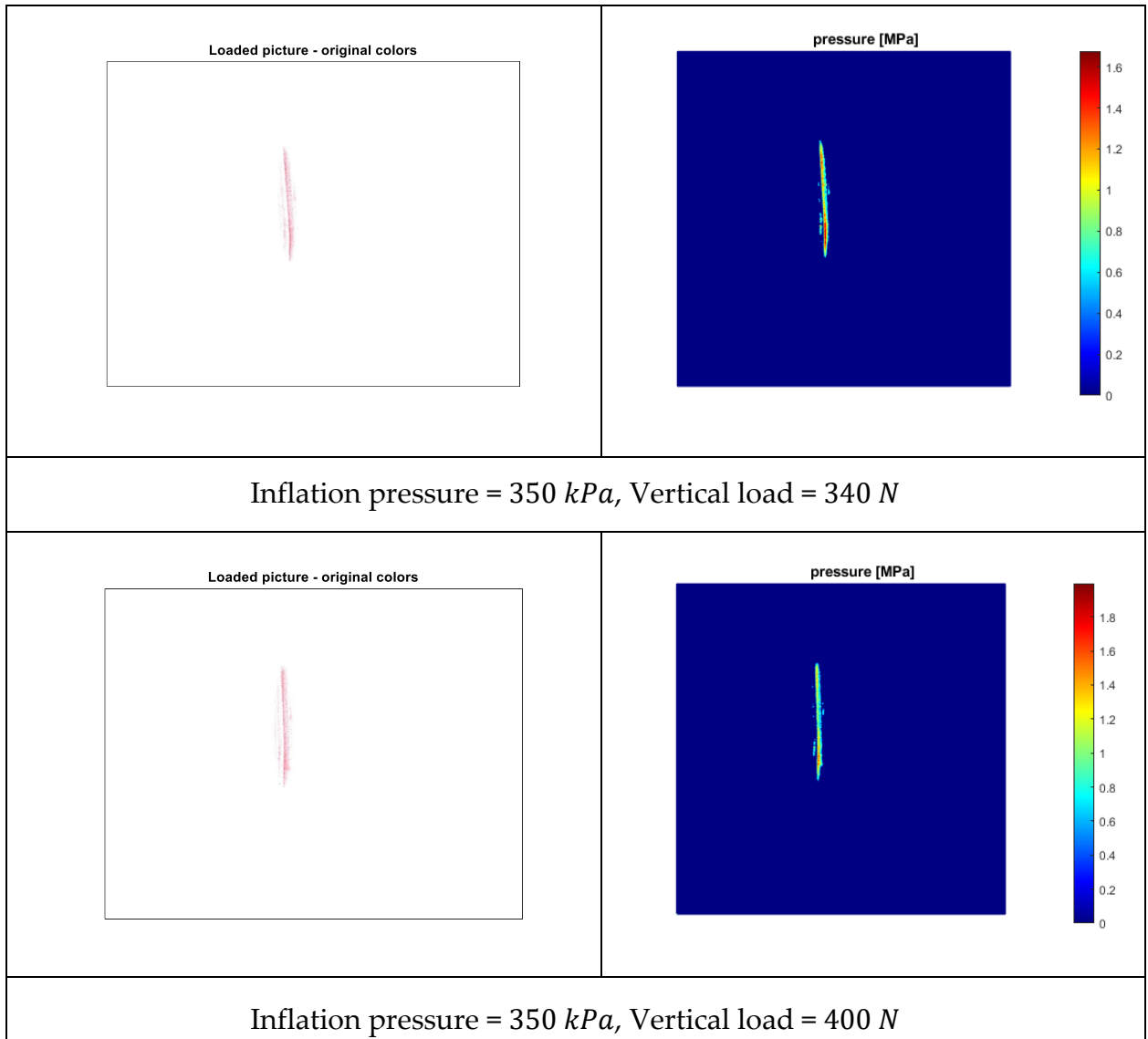
- [37] G. Dell'Orto, F. Ballo and G. Mastinu, "Experimental methods to measure the lateral characteristics of bicycle tyre - a review," *Vehicle system Dynamics*, pp. 1-18, 2022.
- [38] G. Dell'Orto, F. Ballo, G. Mastinu and M. Gobbi, "Bicycle tyres - Development of a new test-rig to measure mechanical characteristics," 2022.
- [39] G. Mastinu, M. Pennati and M. Gobbi, "Design and construction of a test rig for assessing tyre characteristics at rollover," *SAE Technical Papers*, pp. <https://saemobilus.sae.org/content/2002-01-2077/>, 2002.
- [40] G. Mastinu, M. Gobbi, G. Previati, G. Magnani and F. Ballo, "Measurement of forces and moments of bicycle tyres," *Bicycle and Motorcycle Dynamics 2019 Symposium on the Dynamics and Control of Single Track Vehicles*, pp. 405-420, 2019.
- [41] P. T. M. SpA, "Poly-V Belts and Pulleys."
- [42] W. F. M. & D. L. Milliken, *Race Car Vehicle Dynamics*, 1995.
- [43] J. Anderson, "Fuzzy Logic Approach to Vehicle Stability Control of Oversteer," June 2011. [Online]. Available: https://www.researchgate.net/figure/Cornering-Stiffness-C-a_fig1_265494260. [Accessed 2023].
- [44] "ISO 19940:2017," ISO, [Online]. Available: <https://www.iso.org/obp/ui/#iso:std:iso:19940:ed-1:v1:en:tab:1>. [Accessed 2023].
- [45] J. Heine, "Optimizing your tire pressure for your weight," *Bicycle Quarterly Press*, 1989.
- [46] "Introduction to Larger Radial Stiffness," Academic Accelerator, [Online]. Available: <https://academic-accelerator.com/Manuscript-Generator/Radial-Stiffness/Larger-Radial-Stiffness>. [Accessed 2023].
- [47] C. V. C. G. Massaro M, "The effect of the inflation pressure on the tyre properties and the motorcycle stability," *Journal of Automobile Engineering*, vol. 227, no. 10, pp. 1480-1488, 2013.
- [48] A. L. K. J. W. M Dudziak, "Static tests the stiffness of car tires," *IOP Conference Series: Materials Science and Engineering*, vol. 776, no. 1.
- [49] M. & H. M. & M. M. Kučera, "Selected tire characteristics and their relation to its radial stiffness," *MM Science Journal*, vol. 2016, pp. 1524-1530, 2016.
- [50] "Calameo: Shwalbe catalogue 2022," Schwalbe, [Online]. Available: <https://www.calameo.com/read/0029161356a0de0782f1c>.
- [51] D. J. v. Vuuren, "RELATIONSHIP BETWEEN TIRE INFLATION PRESSURE".
- [52] P. DW, "Prediction of pavement fatigue and rutting life using different tire types," *KSCE Journal of Civil Engineering*, vol. 12, no. 5, p. 297–303, 2008.
- [53] "Fujifilm Prescale: PRESSURE MEASUREMENT FILM," Fujifilm, [Online]. Available: <https://fujiprescalefilm.com/>. [Accessed 2023].
- [54] "Contact Patch of Tyres – All You Need To Know," Tyremarket, 2017. [Online]. Available: <https://www.tyremarket.com/tyremantra/contact-patch-tyres-need-know/>. [Accessed 2023].
- [55] "Image Processing and Analysis in Java," Imagej, [Online]. Available: <https://imagej.net/ij/>. [Accessed 2023].
- [56] "Understanding Rolling Resistance & Impedance For Cyclists," FLO, [Online]. Available: <https://blog.flocycling.com/aero-wheels/understanding-rolling-resistance-impedance-for-cyclists/>. [Accessed 2023].

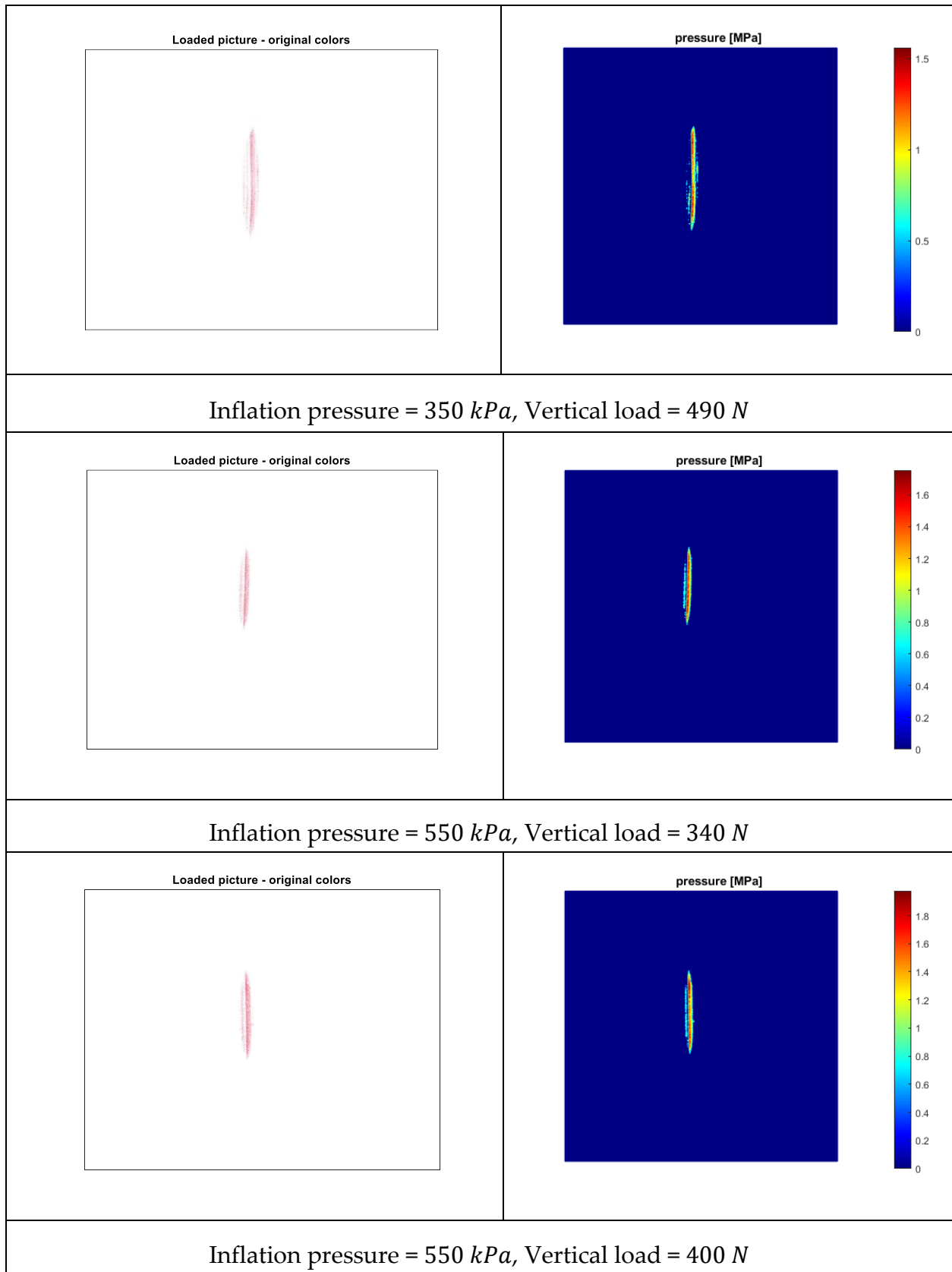
- [57] GlobalSpec, "Friction Coefficient for Teflon and Aluminum," General Magnaplate, 2007. [Online]. Available: <https://cr4.globalspec.com/thread/11912/Friction-Coefficient-for-Teflon-and-Aluminum>. [Accessed 2023].
- [58] "Contact patch size," mtbr, [Online]. Available: <https://www.mtbr.com/threads/contact-patch-size.996851/>. [Accessed 2023].
- [59] H. v. P. S. W. A. a. P. G. Abel, "Optimization of Lateral Vehicle Dynamics by Targeted Dimensioning of the Rim Width," *SAE Int. J. Passeng. Cars - Mech. Syst.*, vol. 8, no. 4, pp. 1196-1208,, 2015.
- [60] P. K, "Effect of tyre inflation pressure on the vehicle dynamics during braking manouvre," *Maintenance and Reliability*, vol. 15, no. 2, pp. 134-139, 2013.
- [61] G. Mastinu and M. Ploechl, Road and Off-Road Vehicle System Dynamics Handbook, 2014.
- [62] H.B.Pacejka, Tyre and Vehicle Dynamics, Butterworth and Heinemann, 2006.
- [63] O. A. O. ChongfengWei, "The effects of tyre material and structure properties on relaxation length using finite element method," vol. 102, pp. 14-20, 2006.
- [64] "Relaxation length: What is it & what affects It?," SIMPLETIRE, [Online]. Available: <https://simpletire.com/learn/tire-news-information/relaxation-length>. [Accessed 2023].
- [65] T. L. Doria A, "Out-of-plane vibrations and relaxation length of the tyres for single-track vehicles," *Journal of Automobile Engineering*, vol. 230, no. 5, pp. 609-622, 2016.
- [66] D. L. L. W. H. e. a. Lu, "Tire Dynamics Modeling Method Based on Rapid Test Method," *Chinese Journal of Mechanical Engineering*, vol. 33, no. 85, 2020.
- [67] A. D. a. A. Rahman, "Measuring sideslip and camber characteristics of bicycle tyres," *Vehicle System Dynamics*, vol. 50, no. 8, pp. 1365-1378, 2012.
- [68] V. Cossalter, Motorcycle dynamics, 2002.
- [69] "Hiwin," [Online]. Available: <https://www.hiwin.it/>. [Accessed 2023].
- [70] "EG Series – Low profile Ball Type Linear Guideway," Hiwin, [Online]. Available: <https://motioncontrolsystems.hiwin.us/configurator/eg-series-block>. [Accessed 2023].
- [71] "'actxserver' documentation," Mathworks.com (Matlab®), [Online]. Available: <https://it.mathworks.com/help/matlab/ref/actxserver.html>. [Accessed 2023].

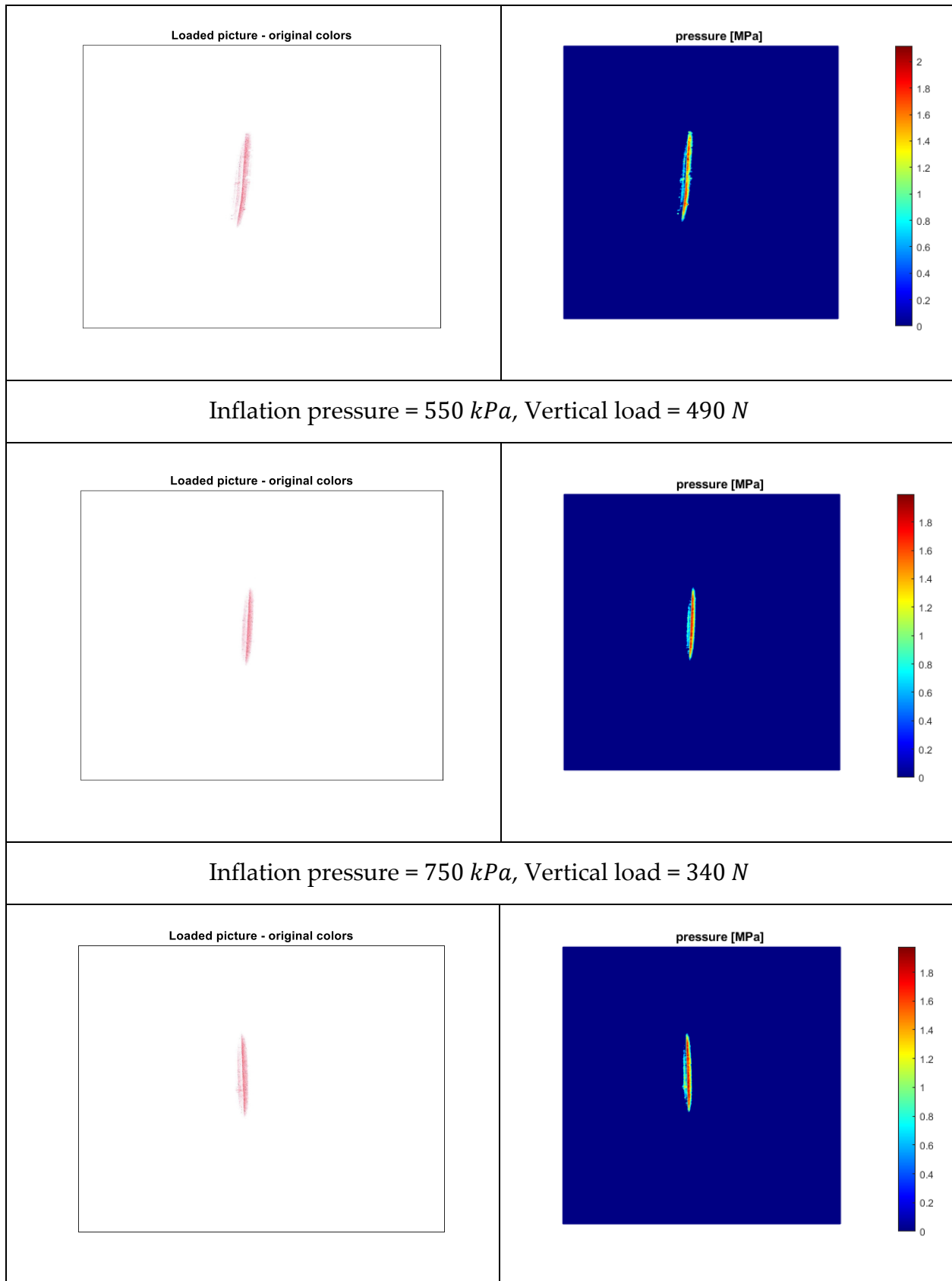
A Appendix A

A.1. Contact patch

The contact patch analysis in Section 4.2 provides the image of only one example of contact patch defined with the Prescale measuring film. In this Appendix, in Table 1 and Table 2, all the images obtained and processed for the two considered road racing bike tyres (VIT-T10 and VIT-T11) are reported in order to have a complete visualization of the effect when changing a parameter (vertical load or inflation pressure).







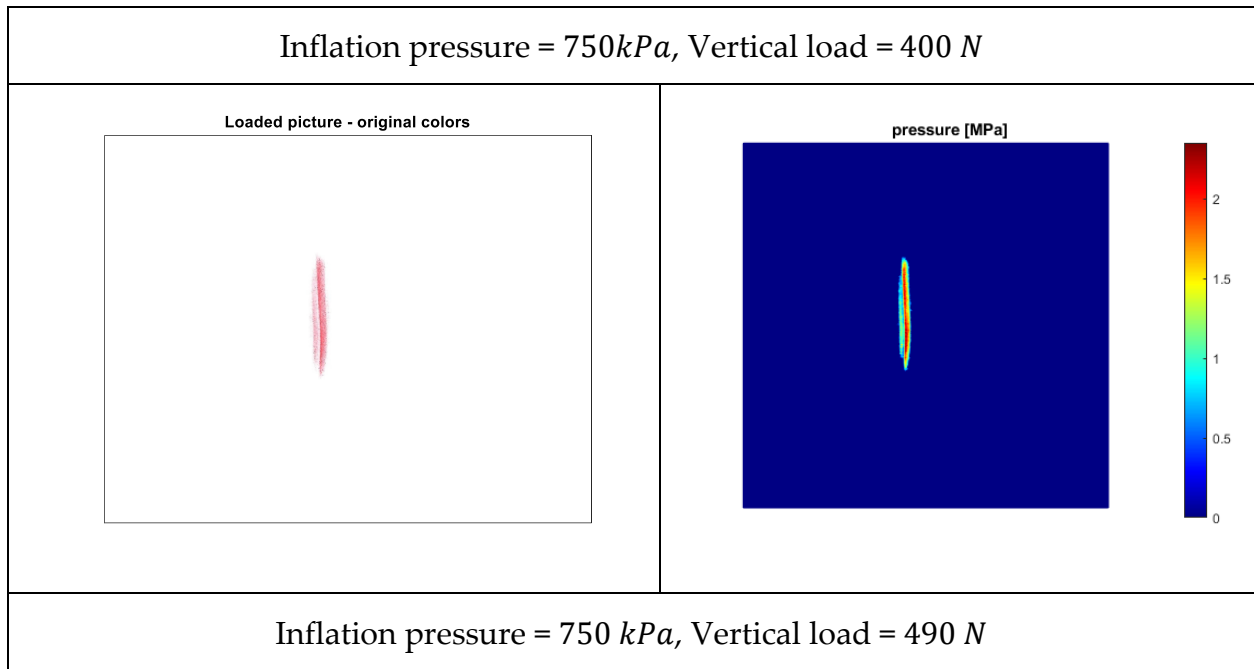
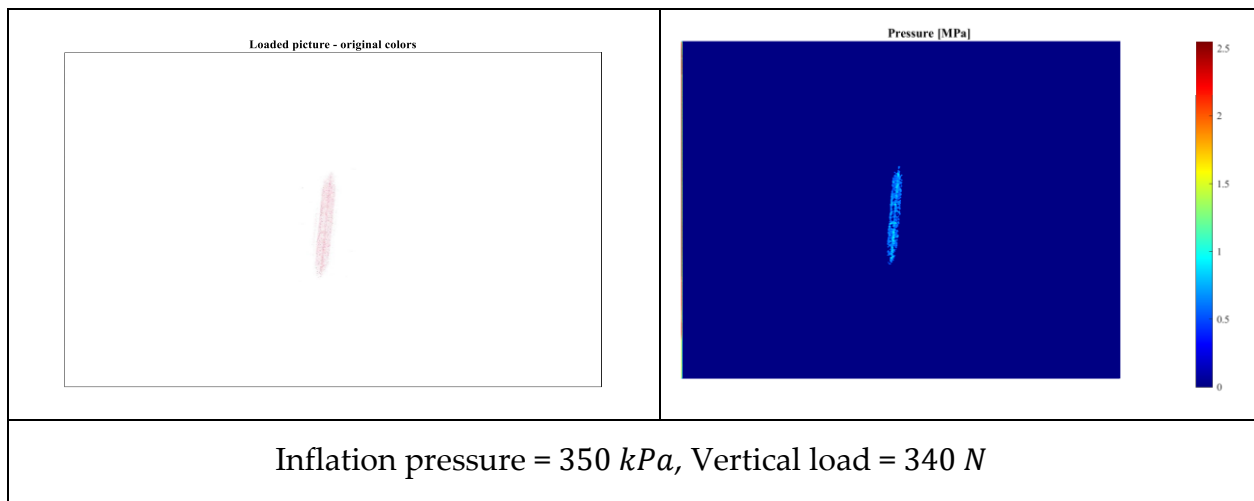
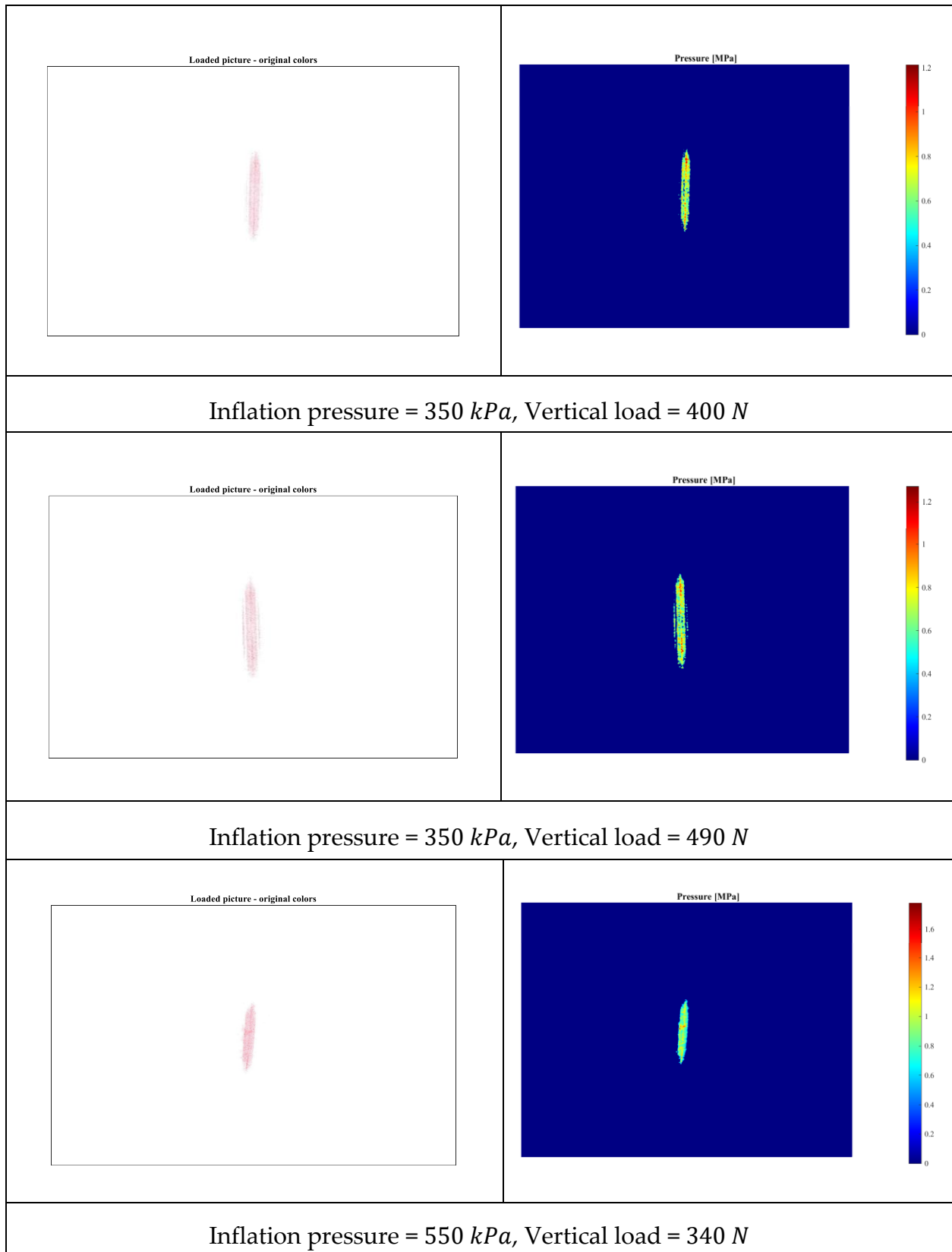
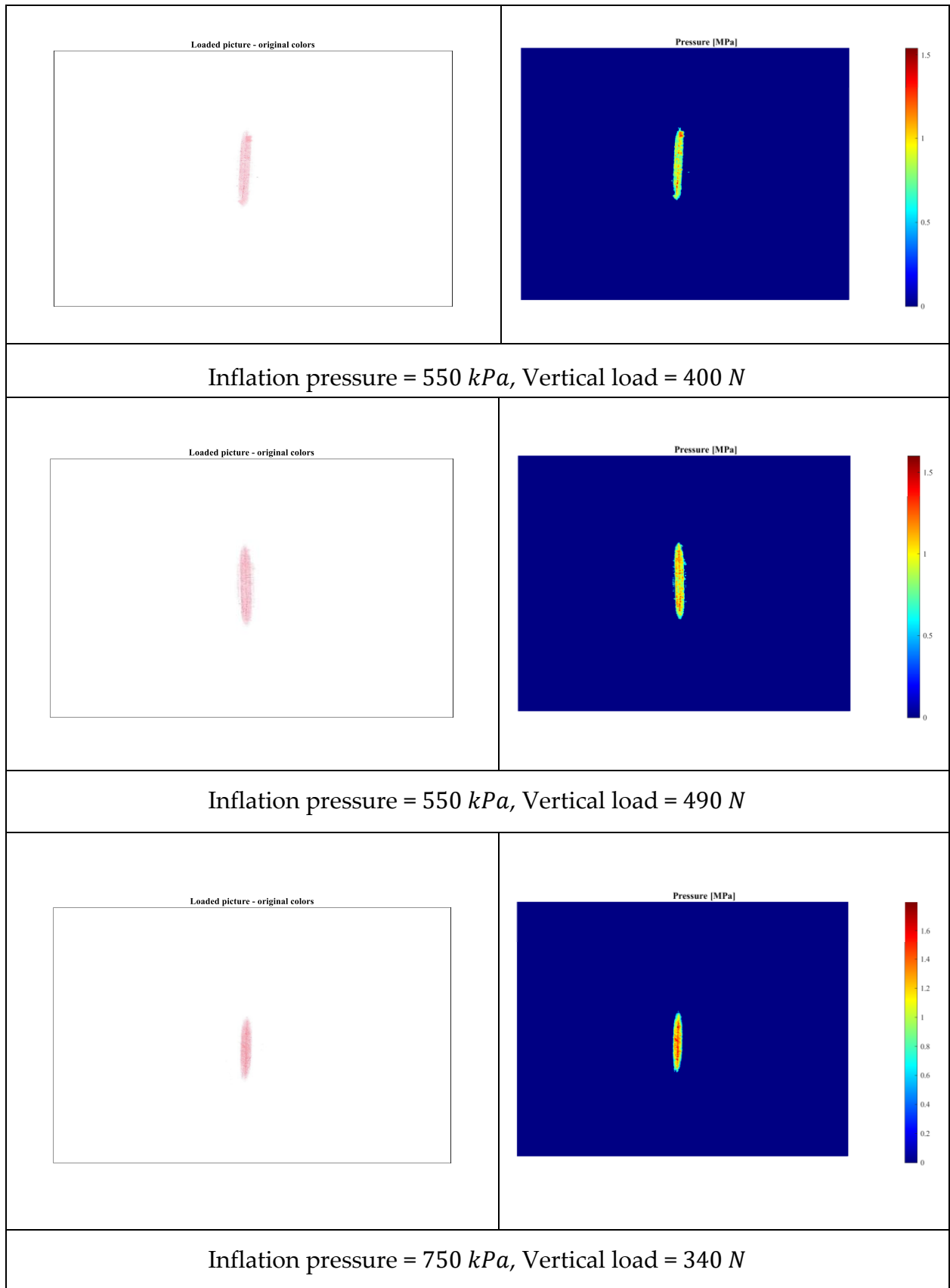


Table A. 1: Full contact patch analysis for VIT-T10.







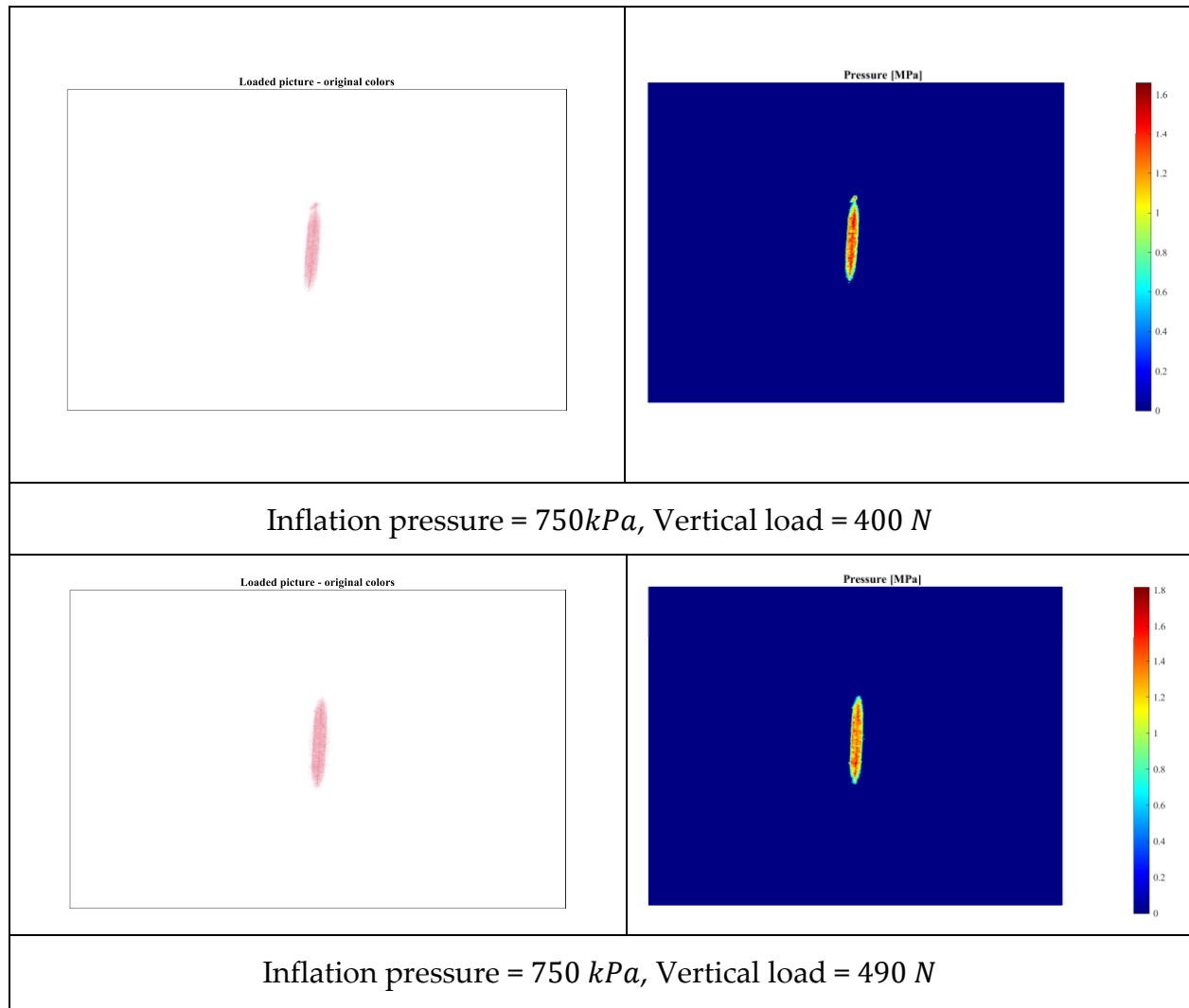


Table A. 2: Full contact patch analysis for VIT-T11.

B Appendix B

The Post Processing software described in Section 5.2 is made up of a main script called ‘postProcessing’ and several additional functions and scripts. Here is reported the code for the main scripts and the main functions.

B.1. Post Processing code

Post Processing: main script

```
% Environment Preparation
clc
clear
close all
fclose('all');
set(0,'DefaultFigurewindowStyle','normal')
set(groot,'defaultfigureposition',[300 150 900 550])
set(groot,'DefaultAxesFontSize',11)
% Adding folders to the path
addpath('input\')
addpath(genpath('Toolbox\'))
% Input data
measuringdata
kinematicData
tireBrand          = 'scalato';
tireCode           = 'T05';
rimCode            = 'R01';
slope              = 1;
% IMPORTANT: 0 must always be the first element in the cambervals vector
cambervals         = [0 -5 5];           % Camber angle [°]
loadvals           = [343 404 488];       % Static force [N]
dataTest.p          = 400;                 % Pressure [kPa]
dataTest.alphacut   = 1;                  % Cut-off slip angle [°]
dataVetyl.m_wheel  = 12.73;               % Mass shaft+fork+wheel [kg]
% Loading the zero file corresponding to the test session
zero               = load(['zero_22_11_2022.dat']);
% Generate struct containing all averaged and wanted data
initChoice = menu('Do you want to use previously saved data?','Yes','No');
if initChoice == 1
    load(uigetfile('*.*mat'));
else
    avgStorage = repmat(struct(),length(cambervals),length(loadvals));
    for iii = 1:length(loadvals)
        dataTest.Fz0 = loadvals(iii);
        for jjj = 1:length(cambervals)
            dataTest.camber = cambervals(jjj);
            disp([dataTest.Fz0 dataTest.camber])
            % Running processingData script to obtain the elaborated
            % test data
            processingData
            % Storing all the elaborated data into the 'avgStorage' struct
            fieldName = strcat('Fz_',num2str(dataTest.Fz0),'_camber_',...
                num2str(signString),num2str(camberAbs));
            avgStorage(jjj,iii).(fieldName) = dataElab;
        end
    end
    % Saving the struct
    choice = menu('Do you want to save the elaborated data?','Yes','No');
end
```

```

if choice == 1
    stdFilename = strcat(num2str(tireBrand), '_', num2str(tireCode), num2str(rimCode), '.mat');
    save(uiputfile('.*', 'File Selection', stdFilename), 'avgStorage');
end
end
% Interactive selector to choose the analysis type (load variation, camber
% variation, cornering stiffness, all)
selectorGUI
% Loading file containing the operator choice
load('selector.mat')
% Actuating the selection
% VARYING LOAD
if selector(1) == 1 || selector(4) == 1
    % Plot varying load
    for ww = 1:length(cambervals)
        camber = cambervals(ww);
        if camber < 0
            signString = 'meno';
            signs = ' - ';
        else
            signString = '';
            signs = '';
        end
        camberString = strcat(signString, num2str(abs(camber)));
    % Plot Mz
    figure('Name', strcat('Mz: camber=', num2str(camber), '^'), 'color', 'w')
    for xx = 1:length(loadvals)
        Fz = loadvals(xx);
        fieldname = strcat('Fz_', num2str(Fz), '_camber_', ...
                           camberString);
        toPlot = avgStorage(ww, xx).(fieldname);
        legendinfoA{xx} = ['Fz = ', num2str(Fz), 'N'];
        plot(toPlot.alphaMz, toPlot.Mz)
        hold on
        grid on
        title('Self-aligning moment vs slip angle')
        subtitle(['P = ', num2str(dataTest.p), 'kPa, ', '\gamma = ', signs, num2str(abs(camber)), '^'])
        xlim([-4 4])
        ylim([-6 6])
        xlabel('\alpha [deg]')
        ylabel('M_z [Nm]')
        legend(legendinfoA)
    end
    % Plot Fy
    figure('Name', strcat('Fy: camber=', num2str(camber), '^'), 'color', 'w')
    for xx = 1:length(loadvals)
        Fz = loadvals(xx);
        fieldname = strcat('Fz_', num2str(Fz), '_camber_', ...
                           camberString);
        toPlot = avgStorage(ww, xx).(fieldname);
        legendinfoB{xx} = ['Fz = ', num2str(Fz), 'N'];
        plot(toPlot.alphaFy, toPlot.Fy)
        hold on
        grid on
        title('Lateral force vs slip angle')
        subtitle(['P = ', num2str(dataTest.p), 'kPa, ', '\gamma = ', signs, num2str(abs(camber)), '^'])
        xlim([-7 7])
        ylim([-500 500])
        xlabel('\alpha [deg]')
        ylabel('F_y [N]')
        legend(legendinfoB, 'Location', 'southeast')
    end
    end
end
% VARYING CAMBER
if selector(2) == 1 || selector(4) == 1
    % plot varying camber
    for ww = 1:length(loadvals)
        Fz = loadvals(ww);
        % Plot Mz
        figure('Name', strcat('Mz: Fz=', num2str(Fz), 'N', 'Color', 'w')
        for xx = 1:length(cambervals)
            camber = cambervals(xx);

```

```

    if camber < 0
        signString = 'meno';
    else
        signString = '';
    end
    camberString = strcat(signString,num2str(abs(camber)));
    fieldname = strcat('Fz_',num2str(Fz),'_camber_',...
        camberString);
    toPlot = avgStorage(xx,ww).(fieldname);
    legendinfoC{xx} = ['\gamma = ',num2str(camber),'^'];
    plot(toPlot.alphaMz,toPlot.Mz)
    hold on
    grid on
    title('Self-aligning moment vs slip angle')
    subtitle(['P = ',num2str(dataTest.p),'kPa, ','F_z = ',num2str(Fz),'N'])
    xlim([-4 4])
    ylim([-6 6])
    xlabel('\alpha [deg]')
    ylabel('M_z [Nm]')
    legend(legendinfoC)
end
% Plot Fy
figure('Name',strcat('Fy: Fz=',num2str(Fz),'N'),'color','w')
for xx = 1:length(cambervals)
    camber = cambervals(xx);
    if camber < 0
        signString = 'meno';
    else
        signString = '';
    end
    camberString = strcat(signString,num2str(abs(camber)));
    fieldname = strcat('Fz_',num2str(Fz),'_camber_',...
        camberString);
    toPlot = avgStorage(xx,ww).(fieldname);
    legendinfoD{xx} = ['\gamma = ',num2str(camber),'^'];
    plot(toPlot.alphaFy,toPlot.Fy)
    hold on
    grid on
    title('Lateral force vs slip angle')
    subtitle(['P = ',num2str(dataTest.p),'kPa, ','F_z = ',num2str(Fz),'N'])
    xlim([-7 7])
    ylim([-500 500])
    xlabel('\alpha [deg]')
    ylabel('F_y [N]')
    legend(legendinfoD,'Location','southeast')
end
end
% Generate Cornering Stiffness table
if selector(3) == 1 || selector(4) == 1
    CS = zeros(length(cambervals),length(loadVals));
    varNames = {'camber'};
    for ww = 1:length(loadVals)
        Fz = loadVals(ww);
        varNames = [varNames strcat('Fz',num2str(Fz))];
        for xx = 1:length(cambervals)
            camber = cambervals(xx);
            if camber < 0
                signString = 'meno';
            else
                signString = '';
            end
            camberString = strcat(signString,num2str(abs(camber)));
            fieldname = strcat('Fz_',num2str(Fz),'_camber_',...
                camberString);
            CS(xx,ww) = avgStorage(xx,ww).(fieldname).cs;
        end
    end
    csTable = array2table([cambervals' CS],'VariableNames',varNames);
end
delete 'Toolbox\Temp\selector.mat'
% Automatic saving

```

```

if selector(1) == 1 || selector(2) == 1 || selector(3) == 1
    choice5 = menu('Do you want to save the plots?', 'Yes', 'No');
    if choice5 == 1
        % Generating Plots folder
        if ~exist('Plots', 'dir')
            mkdir('Plots');
        end
        % Generating fig folder
        if ~exist('Plots/fig', 'dir')
            mkdir('Plots/fig');
        end
        % Generating emf folder
        if ~exist('Plots/emf', 'dir')
            mkdir('Plots/emf');
        end

        folderName_fig = 'Plots/fig';
        folderName_jpg = 'Plots/JPG/';
        figList = findobj(allchild(0), 'flat', 'Type', 'figure');
        for iFig = 1:length(figList)
            % Generating plot name
            figHandle = figList(iFig);
            figName = strrep(strrep(get(figHandle, 'Name'), ': ','_'), '=','_');
            fileName = [num2str(tireBrand), '_', num2str(tireCode), num2str(rimCode), ...
                        '_', num2str(dataTest.p), '_kPa_', figName];
            % Saving fig
            savefig(figHandle, fullfile(folderName_fig, fileName));
            % Saving emf
            exportgraphics(figHandle, [folderName_jpg, fileName, '.emf'], 'ContentType', 'vector')
        end
    end
end

```

'processingData.m': elaboration of the DAT file inside the for-loop

```

% Get camber sign
if dataTest.camber < 0
    signString = 'meno';
    camberAbs = abs(dataTest.camber);
else
    signString = '';
    camberAbs = dataTest.camber;
end
% Automatic struct field name creation
filename = strcat(num2str(tireBrand), '_', num2str(tireCode), num2str(rimCode), ...
                  '_', num2str(dataTest.p), '_kPa_Fz_', num2str(dataTest.Fz0), '_camber_', ...
                  num2str(signString), num2str(camberAbs), '*.dat');
fpattern = fullfile('input', filename);
files = dir(fpattern);
for ii = 1 : length(files)
    testname = strcat('test', num2str(ii));
    tests.(testname) = load(files(ii).name);
end
% Comparison between tests with same parameters
% Plot for-loop
for jj = 1:length(files)
    d = load(files(jj).name);
    % Subtracting zero file
    d(:,1) = d(:,1) - mean(zero(:,2));
    d(:,2) = d(:,2) - mean(zero(:,3));
    % Filtering
    d = idfilt(d, 4, dataTest.fcut^2/1612, 'Noncausal');
    % Quick data elaboration
    time = (0:1/dataTest.fsamp:1/dataTest.fsamp*(size(d,1) - 1))';
    Fw1 = d(:,1)*100/1.953821*9.81*1000;           % Fwatt1 [N]
    Fw2 = d(:,2)*100/1.953821*9.81*1000;           % Fwatt2 [N]

```

```

alpha    = d(:,5);                                % slip angle [deg]
Fwatt   = Fw2 - Fw1;
% Plots
legendinfo{jj} = num2str(jj);
subplot(2,1,1)
plot(time,Fwatt)
hold on
grid on
ylabel('F_w_a_t_t [N]')
title('F watt')
legend(legendinfo)
subplot(2,1,2)
plot(time,alpha)
hold on
grid on
ylabel('\alpha [deg]')
title('Slip angle')
legend(legendinfo)
end
% Analysis type selector
choice1 = menu('Analysis type:','Single Test','Average');
if choice1 == 1                                     % Choice: 'Single Test'
    % Single test selector
    choice2      = menu('which test?',legendinfo);
    it           = 0;
    check        = 0;
    while check == 0
        it = it + 1;
        if choice2 == it
            % Loading the selected test
            fieldname1      = strcat('test',num2str(it));
            analysing.(fieldname1) = tests.(fieldname1);
            check           = 1;
        end
    end
else                                                 % Choice: 'Average'
    n           = numel(fieldnames(tests));
    figUI       = uifigure('Position',[650 250 300 300]);
    lbl         = uilabel(figUI);
    % Tests to average selector
    lbl.Text     = 'Choose which tests to average:';
    lbl.Position  = [30 215 200 100];
    lbl.FontSize  = 13;
    cbx          = zeros(n,1);
    for ii = 1:n
        h           = 210 - (ii - 1)*22;
        cbx(ii,1)   = uicheckbox(figUI,'Position',[55 h 102 15],...
            'Text',strcat('Test',num2str(ii)));
    end
    cbxAll  = uicheckbox(figUI,'Position',[55 (h - 22) 102 15],...
        'Text',strcat('All'));
    b       = uibutton(figUI,'push','ButtonPushedFcn',@(b,event) buttonPushed(b,cbx,cbxAll,tests,n,figUI));
    b.Text  = 'Confirm';
    uiwait(figUI)
    load('analysing.mat')
end
close all
% Filter data
[dataF]    = filterData(dataTest,analysing,zero);
% Select only the interesting part of the test
[dataCut]   = cuttingData(dataF,slope);
% Averaging
[averaged]  = averagingData(dataCut,dataTest);
% Calculation of the wanted physical quantities
if dataTest.camber == 0
    shift = [];
end
[dataElab,shift] = calcs(averaged,dataKin,dataVetyt,dataTest,slope,shift);
% Cornering stiffness calculation
[valueCS]   = corneringStiffness(dataElab,dataTest,slope);
dataElab.cs = valueCS;
% Delete temporary files
if exist('Toolbox\Temp\analysing.mat','file')

```

```

    delete 'Toolbox\Temp\analysing.mat'
end
clear tests legendinfo analysing
% Callback function for the push button
function buttonPushed(~,cbx,cbxAll,tests,n,figUI)
    allToggle = get(cbxAll,'Value');
    if allToggle == 0
        for ii = 1:n
            toggle = get(cbx(ii,1),'Value');
            if toggle == 1
                fieldname2           = strcat('test',num2str(ii));
                analysing.(fieldname2) = tests.(fieldname2);
            end
        end
    else
        for jj = 1:n
            fieldname2           = strcat('test',num2str(jj));
            analysing.(fieldname2) = tests.(fieldname2);
        end
    end
    save('Toolbox/Temp/analysing','analysing')
    uiresume(figUI)
    close(figUI)
end

```

'filterData.m' function: filtering all selected data

```

function [dataFilt] = filterData(dataTest,analysing,comp)
    % Filtering process for all of the selected tests
    fn = fieldnames(analysing);
    for ii = 1:numel(fn)
        test          = analysing.(fn{ii});
        time         = (0:1/dataTest.fsamp:1/dataTest.fsamp*(size(test,1)-1))'; % Time vector of the test [s]
        timecomp     = (0:1/dataTest.fsamp:1/dataTest.fsamp*(size(comp,1)-1))'; % Time vector of the compensation
        test [s]
        test          = [time,test];
        comp          = [timecomp,comp];
        % Subtracting the zero values to the signals
        test(:,1)      = test(:,1); % Time [s]
        test(:,2)      = test(:,2) - mean(comp(:,2)); % Measured Watt Linkage force (1) [mV]
        test(:,3)      = test(:,3) - mean(comp(:,3)); % Measured Watt Linkage force (2) [mV]
        test(:,4)      = test(:,4) - mean(test(1:1000,4)); % Measured steering force [mV]
        test(:,5)      = test(:,5) - mean(comp(:,5)); % Measured vertical force [mV]
        test(:,6)      = test(:,6); % Measured slip angle [°]
        % Filtering the signals
        dataFiltered   = idfilt(test,4,dataTest.fcut*2/1612,'Noncausal');
        % Create the dataFilt struct, which stores all the data as
        % subfields of the struct fields which represent the analysed
        % tests.
        dataFilt.(fn{ii}).time  = dataFiltered(:,1);
        dataFilt.(fn{ii}).Fw1   = dataFiltered(:,2);
        dataFilt.(fn{ii}).Fw2   = dataFiltered(:,3);
        dataFilt.(fn{ii}).Fsteer = dataFiltered(:,4);
        dataFilt.(fn{ii}).Fz    = dataFiltered(:,5);
        dataFilt.(fn{ii}).alpha = dataFiltered(:,6);
    end
end

```

'cuttingData.m' function: cutting the acquisition data to focus only on the interesting interval

```

function [dataCut] = cuttingData(dataF,slope)
fn = fieldnames(dataF);
for kk = 1:numel(fn)
    % Defining useful data
    dataFilt          = dataF.(fn{kk});
    alphaDot          = diff(dataFilt.alpha)./diff(dataFilt.time);
    alphaDot(end + 1) = alphaDot(end);
    n                = length(dataFilt.time);
    it               = 0;
    check1           = 0;
    check2           = 0;
    dataFilt.Fw      = dataFilt.Fw2 - dataFilt.Fw1;
    % Getting the peak slip angle values position in the vector
    if slope > 0
        % check on the slip angle signal slope
        while check1 < 2
            it = it + 1;
            if alphadot(it) > 0.3 && check1 == 0
                posLW   = it;
                check1 = 1;
            elseif alphadot(it) < 0 && check1 == 1
                posRW   = it;
                check1 = 2;
            end
        end
    elseif slope < 0
        while check1 < 2
            it = it + 1;
            if alphadot(it) < -0.3 && check1 == 0
                tLW    = dataFilt.time(it);
                posLW  = it;
                check1 = 1;
            elseif alphadot(it) > 0 && check1 == 1
                tRW    = dataFilt.time(it);
                posRW  = it;
                check1 = 2;
            end
        end
    end
    % Defining the cut vectors
    dataCut.(fn{kk}).time    = dataFilt.time(posLW:posRW);
    dataCut.(fn{kk}).Fw1     = dataFilt.Fw1(posLW:posRW);
    dataCut.(fn{kk}).Fw2     = dataFilt.Fw2(posLW:posRW);
    dataCut.(fn{kk}).Fsteer  = dataFilt.Fsteer(posLW:posRW);
    dataCut.(fn{kk}).Fz      = dataFilt.Fz(posLW:posRW);
    dataCut.(fn{kk}).alpha   = dataFilt.alpha(posLW:posRW);
    dataCut.(fn{kk}).alphaog = dataFilt.alpha;
end
end

```

'averagingData.m' function: averaging the selected tests (if 'Average' analysis type is chosen)

```

function [averaged] = averagingData(dataCut,dataTest)
% Built a new overall time vector
fn          = fieldnames(dataCut);
maxLength   = 0;
for mm = 1:numel(fn)
    newLength = length(dataCut.(fn{mm}).time);
    if newLength > maxLength
        maxLength = newLength;
    end
    averaged.time = (0:1/dataTest.fsamp:1/dataTest.fsamp*(maxLength - 1))';
end
% Defines vectors
toAverage.Fw1     = [];
toAverage.Fw2     = [];

```

```

toAverage.Fsteer = [];
toAverage.Fz = [];
toAverage.alpha = [];
% Making all the tests of the same length
for mm = 1:numel(fn)
    evalLength = length(dataCut.(fn{mm}).time);
    if evalLength < maxlen
        deltaLength = maxlen - evalLength;
        toAdd.Fw1 = dataCut.(fn{mm}).Fw1(end).*ones(1,deltaLength)';
        dataCut.(fn{mm}).Fw1 = [dataCut.(fn{mm}).Fw1; toAdd.Fw1];
        toAdd.Fw2 = dataCut.(fn{mm}).Fw2(end).*ones(1,deltaLength)';
        dataCut.(fn{mm}).Fw2 = [dataCut.(fn{mm}).Fw2; toAdd.Fw2];
        toAdd.Fsteer = dataCut.(fn{mm}).Fsteer(end).*ones(1,deltaLength)';
        dataCut.(fn{mm}).Fsteer = [dataCut.(fn{mm}).Fsteer; toAdd.Fsteer];
        toAdd.Fz = dataCut.(fn{mm}).Fz(end).*ones(1,deltaLength)';
        dataCut.(fn{mm}).Fz = [dataCut.(fn{mm}).Fz; toAdd.Fz];
        toAdd.alpha = dataCut.(fn{mm}).alpha(end).*ones(1,deltaLength)';
        dataCut.(fn{mm}).alpha = [dataCut.(fn{mm}).alpha; toAdd.alpha];
    end
    toAverage.Fw1 = [toAverage.Fw1; dataCut.(fn{mm}).Fw1];
    toAverage.Fw2 = [toAverage.Fw2; dataCut.(fn{mm}).Fw2];
    toAverage.Fsteer = [toAverage.Fsteer; dataCut.(fn{mm}).Fsteer];
    toAverage.Fz = [toAverage.Fz; dataCut.(fn{mm}).Fz];
    toAverage.alpha = [toAverage.alpha; dataCut.(fn{mm}).alpha];
end
% Performing the average
for oo = 1:maxlength
    averaged.Fw1(oo,1) = mean(toAverage.Fw1(oo,:));
    averaged.Fw2(oo,1) = mean(toAverage.Fw2(oo,:));
    averaged.Fsteer(oo,1) = mean(toAverage.Fsteer(oo,:));
    averaged.Fz(oo,1) = mean(toAverage.Fz(oo,:));
    averaged.alpha(oo,1) = mean(toAverage.alpha(oo,:));
end
end

```

'calcs.m' function: performing all needed calculations

```

function [dataElab,shift] = calcs(averaged,dataKin,dataVetyt,dataTest,slope,shift)
% Getting kinematic data and acquired signals in the correct units
braccio = dataKin(5,:);
ALPHA = dataKin(6,:);
Fw1 = averaged.Fw1*100/1.953821*9.81*1000; % Measured Watt Linkage force (1) [N]
Fw2 = averaged.Fw2*100/1.953821*9.81*1000; % Measured Watt Linkage force (2) [N]
Fsteer = averaged.Fsteer*50/2.0037*9.81*1000; % Measured steering force [N]
Fvert = averaged.Fz*250/1.9968*9.81*1000; % Measured vertical force [N]
alpha = averaged.alpha; % Measured slip angle [°]
Fw = Fw2 - Fw1;
% Getting the steering arm correspondent to each slip angle [mm]
arm = [];
for jj = 1:length(alpha)
    arm(jj) = braccio(1);
    error_alpha = abs(ALPHA(1) - alpha(jj));
    for kk = 2:length(ALPHA)
        if abs(ALPHA(kk) - alpha(jj)) < error_alpha
            arm(jj) = braccio(kk);
            error_alpha = abs(ALPHA(kk) - alpha(jj));
        end
    end
end
arm = arm';
% Lateral force developed in the tyre (correction pneumatic trail) [N]
Fy = (Fw.*dataVetyt.L + Fsteer.*arm)./(dataVetyt.L2.*cos(alpha.*pi/180));
trail = Fsteer.*arm./Fy; % Pneumatic trail length [mm]
Mz = Fsteer.*arm./1000; % Self-aligning moment [N.m]
% Fy corrections
if dataTest.camber == 0
    [v1,idxFy] = min(abs(Fy - 0));

```

```

        alphaA          = alpha(idxFy);
        shift.alphaA    = alphaA;
        dataElab.alphaFy = alpha - alphaA;
    else
        dataElab.alphaFy = alpha - shift.alphaA;
    end
% Cut alpha vector for Mz correction
alpha_Mz    = alpha - dataTest.Mz_x0;
Mz         = Mz - dataTest.Mz_y0;
check      = 0;
it         = 0;
if slope > 0
    while check < 2
        it = it + 1;
        if alpha_Mz(it) > -3 && check == 0
            posLW_Mz = it;
            check    = 1;
        elseif alpha_Mz(it) > 3 && check == 1
            posRW_Mz = it;
            check    = 2;
        end
    end
elseif slope < 0
    while check < 2
        it = it + 1;
        if alpha_Mz(it) < 4 && check == 0
            posLW_Mz = it;
            check    = 1;
        elseif alpha_Mz(it) < -4 && check == 1
            posRW_Mz = it;
            check    = 2;
        end
    end
end
alpha_Mz    = alpha(posLW_Mz:posRW_Mz);
Mzcut       = Mz(posLW_Mz:posRW_Mz);
% Mz correction
if dataTest.camber == 0
    meanMz          = 0.5*(max(Mzcut) + min(Mzcut));
    [v2,idxMz]       = min(abs(Mzcut - meanMz));
    shift.meanMz    = meanMz;
    alphaB          = alpha(posLW_Mz + idxMz - 1);
    shift.alphaB    = alphaB;
    dataElab.alphamZ = alpha - alphaB;
else
    dataElab.alphamZ = alpha - shift.alphaB;
end
% vertical force corrected due to camber
if dataTest.camber >= 0
    Fz = (Fvert + Fy*sin(abs(dataTest.camber*pi/180)) - ...
           datavetyt.m_wheel*datavetyt.g*cos(abs(dataTest.camber*pi/180))/...
           cos(abs(dataTest.camber*pi/180)));
else
    Fz = (Fvert - Fy*sin(abs(dataTest.camber*pi/180)) - ...
           datavetyt.m_wheel*datavetyt.g*cos(abs(dataTest.camber*pi/180))/...
           cos(abs(dataTest.camber*pi/180)));
end
% Building the 'dataElab' struct
dataElab.time      = averaged.time;
dataElab.Fw1        = Fw1;
dataElab.Fw2        = Fw2;
dataElab.Fw        = Fw;
dataElab.Fsteer     = Fsteer;
dataElab.Fz        = Fz;
dataElab.alpha      = alpha;
dataElab.Mz        = Mz;
dataElab.Fy        = Fy;
end

```

'corneringStiffness.m' function: calculating the cornering stiffness

```

function [valueCS] = corneringStiffness(dataElab,dataTest,slope)
    itCS      = 0;
    checkCS   = 0;
    % Cutting the slip angle signal to get the interval defined by the
    % operator for the calculation of the cornering stiffness
    if slope > 0
        while checkCS < 2
            itCS = itCS + 1;
            if dataElab.alphaFy(itCS) > -dataTest.alphacut && checkCS == 0
                tLWCS      = dataElab.time(itCS);
                posLWCS    = itCS;
                checkCS   = 1;
            elseif dataElab.alphaFy(itCS) > dataTest.alphacut && checkCS == 1
                tRWCS      = dataElab.time(itCS);
                posRWCS    = itCS;
                checkCS   = 2;
            end
        end
    elseif slope < 0
        while checkCS < 2
            itCS = itCS + 1;
            if dataElab.alphaFy(itCS) < dataTest.alphacut && checkCS == 0
                tLWCS      = dataElab.time(itCS);
                posLWCS    = itCS;
                checkCS   = 1;
            elseif dataElab.alphaFy(itCS) < -dataTest.alphacut && checkCS == 1
                tRWCS      = dataElab.time(itCS);
                posRWCS    = itCS;
                checkCS   = 2;
            end
        end
    end
    dataCS.time      = dataElab.time(posLWCS:posRWCS);
    dataCS.Fy        = dataElab.Fy(posLWCS:posRWCS);
    dataCS.alpha     = dataElab.alpha(posLWCS:posRWCS);
    % Calculating the Cornering Stiffness through interpolation
    p1              = polyfit(dataCS.alpha,dataCS.Fy,2);
    f1              = polyval(p1,dataCS.alpha);
    valueCS         = f1(2);
    % Print the cornering stiffness value to screen
    disp(['The cornering stiffness value found from the fitting of Fy is of:',num2str(valueCS)])
end

```

'corneringStiffness.m' function: calculating the cornering stiffness

```

clc
clear
close all

% Word setting
addpath(genpath('plots\''))
load('schwalbe_T03R01.mat');
word                      = actxserver('Word.Application');
word.Visible               = 1;
document                  = word.Documents.Open([pwd, '\template.docx']);
selection                 = word.Selection;
selection.Font.Name        = 'Times New Roman';
selection.Font.Size        = 12;
selection.GoToNext('wdGoToPage');

```

```

selection.MoveDown(5,43);
selection.ParagraphFormat.Alignment = 3;

% Parameters
vecP      = [300 400 500];
vecFz     = [343 404 488];
vecCamber = [0 5 -5];
tireBrand = 'schwalbe';
tireCode  = 'T03';
rimCode   = 'R01';

fzString = [];
for xx = 1:length(vecFz)
    if vecFz(xx) == vecFz(end)
        fzString = [fzString, num2str(vecFz(xx)), 'N'];
    else
        fzString = [fzString, num2str(vecFz(xx)), 'N', ''];
    end
end

camString = [];
for xx = 1:length(vecCamber)
    if vecCamber(xx) == vecCamber(end)
        camString = [camString, num2str(vecCamber(xx)), 'N'];
    else
        camString = [camString, num2str(vecCamber(xx)), 'N', ''];
    end
end

pString = [];
for xx = 1:length(vecP)
    if vecP(xx) == vecP(end)
        pString = [pString, num2str(vecP(xx)), 'N'];
    else
        pString = [pString, num2str(vecP(xx)), 'N', ''];
    end
end

% Load variation: Lateral force
selection.InsertBreak;
selection.Font.Bold = 1;
selection.TypeText('Results: Load variation');
selection.TypeParagraph;
selection.TypeText('Lateral force');
selection.Font.Bold = 0;
selection.TypeParagraph;

figN = 1;
tabN = 1;

for ii = 1:length(vecP)
    p = vecP(ii);
    for jj = 1:length(vecCamber)
        cam = vecCamber(jj);

```

```

if cam < 0
    signString = 'meno';
    signs      = ' - ';
else
    signString = '';
    signs      = '';
end
camberString = strcat(signString,num2str(abs(cam)));
selection.ParagraphFormat.Alignment = 'wdAlignParagraphJustify';
selection.TypeText(['Lateral force in function of the side slip angle, for pressure
equal to ',...
    num2str(p),' kPa, camber equal to ', num2str(cam),'^ and varying vertical load
Fz = (',...
    fzString,') ']);
selection.Font.Italic = 1;
selection.TypeText(['(Figure ',num2str(figN),')']);
selection.TypeParagraph;
selection.TypeParagraph;
emfName      =
[tireBrand,'_',tireCode,rimCode,'_',num2str(p),'_kPa_Fy_camber_',num2str(cam),'.emf'];
emfPath      = [pwd,'\\Plots\\emf\',emfName];
selection.InlineShapes.AddPicture(emfPath);
selection.TypeText(['Figure ',num2str(figN)])
selection.Font.Italic = 0;
selection.ParagraphFormat.Alignment = 'wdAlignParagraphCenter';
selection.TypeParagraph;
selection.TypeParagraph;
selection.ParagraphFormat.Alignment = 'wdAlignParagraphJustify';
selection.TypeText(['In order to have a better understanding of the Figure
',num2str(figN),...
    ', the values of the lateral force for side slip angles of 4° and -4° are
collected in Table '...
    num2str(tabN),'.']);
selection.TypeParagraph;
sz           = 2*length(vecFz) + 1;
selection.TypeParagraph;
selection.ParagraphFormat.Alignment = 'wdAlignParagraphCenter';
word.ActiveDocument.Tables.Add(word.Selection.Range,sz,5);
selection.TypeText("Inflation Pressure [kPa]");
selection.MoveRight(12,1,0);
selection.TypeText("Vertical Load [N]");
selection.MoveRight(12,1,0);
selection.TypeText("Camber [°]");
selection.MoveRight(12,1,0);
selection.TypeText("Side slip angle [°]");
selection.MoveRight(12,1,0);
selection.TypeText("Fz [N]");
selection.MoveRight(12,1,0);

for kk1 = 1:length(vecFz)
    Fz          = vecFz(kk1);
    fieldname   = strcat('Fz_',num2str(Fz),'_camber_',camberString);
    tab         = avgStorage(jj,kk1,ii).(fieldname).tab;
    selection.TypeText(num2str(p));

```

```

selection.MoveRight(12,1,0);
selection.TypeText(num2str(Fz));
selection.MoveRight(12,1,0);
selection.TypeText(num2str(camber));
selection.MoveRight(12,1,0);
selection.TypeText('4');
selection.MoveRight(12,1,0);
selection.TypeText(num2str(round(tab.FyP4,1)));
selection.MoveRight(12,1,0);
end

for kk2 = 1:length(vecFz)
    Fz          = vecFz(kk2);
    fieldname   = strcat('Fz_',num2str(Fz),'_camber_',camberString);
    tab         = avgStorage(jj,kk2,ii).(fieldname).tab;
    selection.TypeText(num2str(p));
    selection.MoveRight(12,1,0);
    selection.TypeText(num2str(Fz));
    selection.MoveRight(12,1,0);
    selection.TypeText(num2str(camber));
    selection.MoveRight(12,1,0);
    selection.TypeText('-4');
    selection.MoveRight(12,1,0);
    selection.TypeText(num2str(round(tab.FyN4,1)));
    if Fz == vecFz(end)
        tableObj = word.ActiveDocument.Tables.Item(6 + figN);
        tableObj.Borders.Enable = 1;
        selection.MoveDown(5,1);
    else
        selection.MoveRight(12,1,0);
    end
end
selection.Font.Italic = 1;
selection.TypeText(['Table ',num2str(tabN)])
selection.Font.Italic = 0;
selection.ParagraphFormat.Alignment = 'wdAlignParagraphCenter';
selection.TypeParagraph;
selection.ParagraphFormat.Alignment = 'wdAlignParagraphJustify';
figN = figN + 1;
tabN = tabN + 1;
selection.InsertBreak;
end
end

selection.TypeText('[Insert tables and considerations on cornering stiffness (only for
varying Fz and P) here.]');
selection.InsertBreak;

% Load variation: self-aligning moment
selection.Font.Bold = 1;
selection.TypeText('Self-aligning moment');
selection.Font.Bold = 0;
selection.TypeParagraph;

```

```

for ii = 1:length(vecP)
    p = vecP(ii);
    for jj = 1:length(vecCamber)
        cam = vecCamber(jj);
        if cam < 0
            signString = 'meno';
            signs      = ' - ';
        else
            signString = '';
            signs      = '';
        end
        camberString = strcat(signString,num2str(abs(cam)));
        selection.ParagraphFormat.Alignment = 'wdAlignParagraphJustify';
        selection.TypeText(['self-aligning moment in function of the side slip angle, for
pressure equal to ',...
                    num2str(p),' kPa, camber equal to ', num2str(cam), '° and varying vertical load
Fz = (',...,
                    fzString,') ']);
        selection.Font.Italic = 1;
        selection.TypeText(['(Figure ',num2str(figN),')']);
        selection.TypeParagraph;
        selection.TypeParagraph;
        emfName      =
[tireBrand,'_',tireCode,rimCode,'_',num2str(p),'kPa_Mz_camber_',num2str(cam),'.emf'];
        emfPath      = [pwd,'\\Plots\\emf\\',emfName];
        selection.InlineShapes.AddPicture(emfPath);
        selection.TypeParagraph;
        selection.TypeText(['Figure ',num2str(figN)])
        selection.Font.Italic = 0;
        selection.ParagraphFormat.Alignment = 'wdAlignParagraphCenter';
        selection.TypeParagraph;
        selection.TypeParagraph;
        selection.ParagraphFormat.Alignment = 'wdAlignParagraphJustify';
        selection.TypeText(['In order to have a better understanding of the Figure
',num2str(figN),...
                    ', the peak values of the self-aligning moment and the relative values of side
slip angles are collected in Table '...
                    num2str(tabN),'.']);
        selection.TypeParagraph;
        sz = 2*length(vecFz) + 1;
        selection.TypeParagraph;
        selection.ParagraphFormat.Alignment = 'wdAlignParagraphCenter';
        word.ActiveDocument.Tables.Add(word.Selection.Range,sz,5);
        selection.TypeText("Inflation Pressure [kPa]");
        selection.MoveRight(12,1,0);
        selection.TypeText("Vertical Load [N]");
        selection.MoveRight(12,1,0);
        selection.TypeText("Camber [°]");
        selection.MoveRight(12,1,0);
        selection.TypeText('alpha Mz_max [°]');
        selection.MoveRight(12,1,0);
        selection.TypeText("Mz_max [N]");
        selection.MoveRight(12,1,0);

```

```

for kk1 = 1:length(vecFz)
    Fz          = vecFz(kk1);
    fieldname   = strcat('Fz_',num2str(Fz),'_camber_',camberString);
    tab         = avgStorage(jj,kk1,ii).(fieldname).tab;
    selection.TypeText(num2str(p));
    selection.MoveRight(12,1,0);
    selection.TypeText(num2str(Fz));
    selection.MoveRight(12,1,0);
    selection.TypeText(num2str(cam));
    selection.MoveRight(12,1,0);
    selection.TypeText(num2str(round(tab.alphaMzMin,1)));
    selection.MoveRight(12,1,0);
    selection.TypeText(num2str(round(tab.MzMin,1)));
    selection.MoveRight(12,1,0);
end

for kk2 = 1:length(vecFz)
    Fz          = vecFz(kk2);
    fieldname   = strcat('Fz_',num2str(Fz),'_camber_',camberString);
    tab         = avgStorage(jj,kk2,ii).(fieldname).tab;
    selection.TypeText(num2str(p));
    selection.MoveRight(12,1,0);
    selection.TypeText(num2str(Fz));
    selection.MoveRight(12,1,0);
    selection.TypeText(num2str(cam));
    selection.MoveRight(12,1,0);
    selection.TypeText(num2str(round(tab.alphaMzMax,1)));
    selection.MoveRight(12,1,0);
    selection.TypeText(num2str(round(tab.MzMax,1)));
    if Fz == vecFz(end)
        tableObj = word.ActiveDocument.Tables.Item(6 + figN);
        tableObj.Borders.Enable = 1;
        selection.MoveDown(5,1);
    else
        selection.MoveRight(12,1,0);
    end
end
selection.Font.Italic = 1;
selection.TypeText(['Table ',num2str(tabN)]);
selection.Font.Italic = 0;
selection.ParagraphFormat.Alignment = 'wdAlignParagraphCenter';
selection.TypeParagraph;
selection.ParagraphFormat.Alignment = 'wdAlignParagraphJustify';
figN = figN + 1;
tabN = tabN + 1;
selection.InsertBreak;
end
end

% Camber variation: Lateral force
selection.Font.Bold = 1;
selection.TypeText('Results: Camber variation');
selection.TypeParagraph;

```

```

selection.TypeText('Lateral force');
selection.Font.Bold=0;
selection.TypeParagraph;

for ii = 1:length(vecP)
    p = vecP(ii);
    for jj = 1:length(vecFz)
        fz = vecFz(jj);
        selection.ParagraphFormat.Alignment = 'wdAlignParagraphJustify';
        selection.TypeText(['Lateral force in function of the side slip angle, for pressure
equal to ',...,
    num2str(p),' kPa, vertical load Fz = ', num2str(fz), 'N and varying camber
gamma = (',...,
    camString,') ']);
    selection.Font.Italic = 1;
    selection.TypeText(['(Figure ',num2str(figN),')']);
    selection.TypeParagraph;
    selection.TypeParagraph;
    emfName      =
[tireBrand,'_',tireCode,rimCode,'_',num2str(p),'kPa_Fy_Fz_',num2str(fz),'N.emf'];
    emfPath      = [pwd,'\\Plots\\emf\',emfName];
    selection.InlineShapes.AddPicture(emfPath);
    selection.TypeText(['Figure ',num2str(figN)])
    selection.Font.Italic = 0;
    selection.ParagraphFormat.Alignment = 'wdAlignParagraphCenter';
    selection.TypeParagraph;
    selection.TypeParagraph;
    selection.ParagraphFormat.Alignment = 'wdAlignParagraphJustify';
    selection.TypeText(['In order to have a better understanding of the Figure
',num2str(figN),...
    ', the values of the lateral force for side slip angles of 2° and -2° are
collected in Table '...
    num2str(tabN),'.']);
    selection.TypeParagraph;
    sz = 2*length(vecFz) + 1;
    selection.TypeParagraph;
    selection.ParagraphFormat.Alignment = 'wdAlignParagraphCenter';
    word.ActiveDocument.Tables.Add(word.Selection.Range,sz,5);
    selection.TypeText("Inflation Pressure [kPa]");
    selection.MoveRight(12,1,0);
    selection.TypeText("Vertical Load [N]");
    selection.MoveRight(12,1,0);
    selection.TypeText("Camber [°]");
    selection.MoveRight(12,1,0);
    selection.TypeText("Side slip angle [°]");
    selection.MoveRight(12,1,0);
    selection.TypeText("Fz [N]");
    selection.MoveRight(12,1,0);

    for kk1 = 1:length(vecCamber)
        cam      = vecCamber(kk1);
        if cam < 0
            signString = 'meno';
            signs     = ' - ';

```

```

    else
        signString = '';
        signs      = '';
    end
    camberString = strcat(signString,num2str(abs(cam)));
    fieldname   = strcat('Fz_',num2str(fz),'_camber_',camberString);
    tab         = avgStorage(kk1,jj,ii).(fieldname).tab;
    selection.TypeText(num2str(p));
    selection.MoveRight(12,1,0);
    selection.TypeText(num2str(Fz));
    selection.MoveRight(12,1,0);
    selection.TypeText(num2str(cam));
    selection.MoveRight(12,1,0);
    selection.TypeText('2');
    selection.MoveRight(12,1,0);
    selection.TypeText(num2str(round(tab.FyP4,1)));
    selection.MoveRight(12,1,0);
end

for kk2 = 1:length(vecCamber)
    cam          = vecCamber(kk2);
    if cam < 0
        signString = 'meno';
        signs      = ' - ';
    else
        signString = '';
        signs      = '';
    end
    camberString = strcat(signString,num2str(abs(cam)));
    fieldname   = strcat('Fz_',num2str(fz),'_camber_',camberString);
    tab         = avgstorage(kk2,jj,ii).(fieldname).tab;
    selection.TypeText(num2str(p));
    selection.MoveRight(12,1,0);
    selection.TypeText(num2str(Fz));
    selection.MoveRight(12,1,0);
    selection.TypeText(num2str(cam));
    selection.MoveRight(12,1,0);
    selection.TypeText('-2');
    selection.MoveRight(12,1,0);
    selection.TypeText(num2str(round(tab.FyN4,1)));
    if cam == vecCamber(end)
        tableObj = word.ActiveDocument.Tables.Item(6 + figN);
        tableObj.Borders.Enable = 1;
        selection.MoveDown(5,1);
    else
        selection.MoveRight(12,1,0);
    end
end
selection.Font.Italic = 1;
selection.TypeText(['Table ',num2str(tabN)])
selection.Font.Italic = 0;
selection.ParagraphFormat.Alignment = 'wdAlignParagraphCenter';
selection.TypeParagraph;
selection.ParagraphFormat.Alignment = 'wdAlignParagraphJustify';

```

```

        figN = figN + 1;
        tabN = tabN + 1;
        selection.InsertBreak;
    end
end

selection.TypeText(['Insert tables and considerations on cornering stiffness',...
    '(for varying Fz, P and camber) here.']);
selection.InsertBreak;

% Camber variation: Self-aligning moment
selection.Font.Bold = 1;
selection.TypeText('Self-aligning moment');
selection.Font.Bold = 0;
selection.TypeParagraph;

for ii = 1:length(vecP)
    p = vecP(ii);
    for jj = 1:length(vecFz)
        fz = vecFz(jj);
        selection.ParagraphFormat.Alignment = 'wdAlignParagraphJustify';
        selection.TypeText(['self-aligning moment in function of the side slip angle, for
pressure equal to ',...
            num2str(p), ' kPa, camber equal to ', num2str(cam), '° and varying vertical load
Fz = (' , ...
            fzstring, ') ']);
        selection.Font.Italic = 1;
        selection.TypeText(['(Figure ',num2str(figN),')']);
        selection.TypeParagraph;
        selection.TypeParagraph;
        emfName      =
[tireBrand,'_',tireCode,rimCode,'_',num2str(p),'kPa_MZ_Fz_',num2str(fz),'N.emf'];
        emfPath      = [pwd,'\\Plots\\emf\',emfName];
        selection.InlineShapes.AddPicture(emfPath);
        selection.TypeText(['Figure ',num2str(figN)])
        selection.Font.Italic = 0;
        selection.ParagraphFormat.Alignment = 'wdAlignParagraphCenter';
        selection.TypeParagraph;
        selection.TypeParagraph;
        selection.ParagraphFormat.Alignment = 'wdAlignParagraphJustify';
        selection.TypeText(['In order to have a better understanding of the Figure
',num2str(figN),...
            ', the peak values of the self-aligning moment and the relative values of side
slip angles are collected in Table '...
            num2str(tabN), '.']);
        selection.TypeParagraph;
        sz = 2*length(vecFz) + 1;
        selection.TypeParagraph;
        selection.ParagraphFormat.Alignment = 'wdAlignParagraphCenter';
        word.ActiveDocument.Tables.Add(word.Selection.Range,sz,5);
        selection.TypeText("Inflation Pressure [kPa]");
        selection.MoveRight(12,1,0);
        selection.TypeText("Vertical Load [N]");

```

```

selection.MoveRight(12,1,0);
selection.TypeText("Camber [°]");
selection.MoveRight(12,1,0);
selection.TypeText("alpha Mz_max [°]");
selection.MoveRight(12,1,0);
selection.TypeText("Mz_max [N]");
selection.MoveRight(12,1,0);

for kk1 = 1:length(vecCamber)
    cam      = vecCamber(kk1);
    if cam < 0
        signString = 'meno';
        signs     = ' - ';
    else
        signString = '';
        signs     = '';
    end
    camberString = strcat(signString,num2str(abs(cam)));
    fieldname   = strcat('Fz_',num2str(fz),'_camber_',camberString);
    tab         = avgStorage(kk1,jj,ii).(fieldname).tab;
    selection.TypeText(num2str(p));
    selection.MoveRight(12,1,0);
    selection.TypeText(num2str(Fz));
    selection.MoveRight(12,1,0);
    selection.TypeText(num2str(cam));
    selection.MoveRight(12,1,0);
    selection.TypeText(num2str(round(tab.alphaMzMin,1)));
    selection.MoveRight(12,1,0);
    selection.TypeText(num2str(round(tab.MzMin,1)));
    selection.MoveRight(12,1,0);
end

for kk2 = 1:length(vecCamber)
    cam      = vecCamber(kk2);
    if cam < 0
        signString = 'meno';
        signs     = ' - ';
    else
        signString = '';
        signs     = '';
    end
    camberString = strcat(signString,num2str(abs(cam)));
    fieldname   = strcat('Fz_',num2str(fz),'_camber_',camberString);
    tab         = avgStorage(kk2,jj,ii).(fieldname).tab;
    selection.TypeText(num2str(p));
    selection.MoveRight(12,1,0);
    selection.TypeText(num2str(Fz));
    selection.MoveRight(12,1,0);
    selection.TypeText(num2str(cam));
    selection.MoveRight(12,1,0);
    selection.TypeText(num2str(round(tab.alphaMzMax,1)));
    selection.MoveRight(12,1,0);
    selection.TypeText(num2str(round(tab.MzMax,1)));
    if cam == vecCamber(end)

```

```

        tableObj = word.ActiveDocument.Tables.Item(6 + figN);
        tableObj.Borders.Enable = 1;
        selection.MoveDown(5,1);
    else
        selection.MoveRight(12,1,0);
    end
end
selection.Font.Italic = 1;
selection.TypeText(['Table ',num2str(tabN)])
selection.Font.Italic = 0;
selection.ParagraphFormat.Alignment = 'wdAlignParagraphCenter';
selection.TypeParagraph;
selection.TypeParagraph;
selection.ParagraphFormat.Alignment = 'wdAlignParagraphJustify';
figN = figN + 1;
tabN = tabN + 1;
selection.InsertBreak;
end
end

selection.TypeText(['Insert tables and considerations on eventual other analysis if
present',...
    ' and finally add some conclusions here.']);

% Auto-save and close

cSave = menu('Do you want to save the report?','Yes','No');

if cSave == 1
    document.SaveAs2([pwd,'/',tireBrand,tireCode,rimCode,'.docx']);
else
end

cClose = menu('Do you want to close the report?','Yes','No');

if cClose == 1
    word.Quit();
else
end

```